



Burning Behavior of Oil in Ice Cavities

Final Report

Prepared by:

Dr. Ali S. Rangwala (PI)

Associate Professor,
Department of Fire Protection Engineering,
Worcester Polytechnic Institute
Worcester, MA 01609

Dr. Xiaochuan Shi

Research Scientist
Department of Fire Protection Engineering
Worcester Polytechnic Institute
Worcester, MA 01609

This report has been reviewed by the BSEE and approved for publication. Approval does not signify that the contents necessarily reflect the views and policies of the BSEE, nor does mention of the trade names or commercial products constitute endorsement or recommendation for use. This study was funded by the Bureau of Safety and Environmental Enforcement, US Department of the Interior, Washington, D. C., under Contract Number E14PC00010.

Date: 30 Sep 2016



Acknowledgements

This study is funded by the Bureau of Safety and Environmental Enforcement, US Department of the Interior, Washington, D.C., under Contract Number E14PC00010. The authors would like to thank Karen N. Stone (TPOC) and Paige Shin for support and coordination during this study. We would also like to thank Nathan Lamie and Leonard Zabilansky for support during large scale outdoor tests performed at the US Army Cold Regions Research and Engineering Lab in Hanover NH. Helpful discussions with Prof. V. Raghavan (Indian Institute of Technology, Chennai, India), Prof. Grunde Jomaas, (University of Edinburgh, UK) and Laurens van Gelderen (Technical University of Denmark) are also acknowledged.

Many thanks to WPI personnel, who made contributions during this study (listed in alphabetical order):

Shivaprasad Arava (graduate student)

Dr. Kemal Arsava (post doctoral fellow)

Borth Trevor (lab manager)

Andrew C. Egger (undergraduate student)

Dr. Tahar El-Korchi (FPE department head)

Hamed Farmahini (graduate student)

Nathan Ghion (undergraduate student)

Daniel A. Long (undergraduate student)

Francisco Kang (undergraduate student)

Aarat Kaushik (graduate student)

Dr. Shijin P. Kozhumal (post doctoral fellow)

Qi Li (graduate student)

Zhaozhao Meng (graduate student)

David Petrow (research engineer)

Raymond T. Ranellone Jr. (research engineer)

John P. Ramos (undergraduate student)

Kathleen Ross (undergraduate student)

Samim Safaei (graduate student)

Dr. Hayri Sezer (post doctoral fellow)

Karl Sundberg (undergraduate student)

Stephen Stephansky (undergraduate student)

Nicolas V. Tobar (undergraduate student)

Panyawat Tukaew (undergraduate student)

Preface

This study characterizes the flammability of ANS crude oil in an Arctic environment using a series of experiments uniquely designed and constructed for simulating cold boundary conditions comparable to the Arctic. The report is organized into 7 chapters that discuss the findings of Phase I (4 Tasks), Phase II (1 Task), and Phase III (1 Task). The major findings are summarized below:

Chapter 1: Ignitability of ANS crude oil at low temperatures (-20°C to 0°C)

A unique experimental apparatus was designed, constructed, and tested to investigate the influence of a cold boundary on ignition characteristics of a liquid fuel. The results can be applied towards optimization of igniter designs for ISB in low temperature conditions such as the Arctic environment. Experiments show that with the application of an external heat flux vertical temperature gradient from the fuel surface to colder fuel below, and the lateral temperature gradient between the center of the fuel surface to the vessel boundary increase so do internal convective flows. Due to the increased convection especially in the lateral direction in the liquid phase, the heat required for creating a vapor concentration equal to the lean-limit concentration for a gaseous fuel-air mixture is removed, causing a delay in ignition. This is especially important in cases where crude oil may be trapped between ice walls. This may warrant a careful design of igniters for ISB in arctic conditions with longer duration of heat input to sustain stable flame propagation.

Chapter 2: Characterization of radiant fraction of heat release rate using smoke point of ANS crude oil

Smoke point of a fuel is the maximum height of a smokeless laminar flame (mm) burning in air at which if the flow rate is increased, the fuel will start to produce soot. The laminar smoke point height forms a useful flammability ranking parameter for different blends of crude oil, weathering and emulsification levels. The current study developed an experimental platform to measure the smoke point of ANS crude oil given failure of current test methods (ASTM D1322) to measure smoke point of ANS crude oil. The experiments are unique as they are the first ever to systematically establish the time-varying smoke point of a highly multicomponent and viscous fuel like ANS crude oil. ANS crude oil has 13 distinct smoke point heights during its vaporization ranging from 13 mm (high volatiles) to 1 mm (low volatiles).

Chapter 3: Geometry changes due to ice melting during combustion

A series of experiments were conducted to develop an understanding on the geometry change of an ice cavity using a well characterized, single component, and transparent (easy to visualize) fuel (n-Octane). The experiments proved to be useful in elucidating the controlling parameters associated with the way ice melts during the burning of a layer of fuel floating on water and bounded by icy walls. Based on the observations made during the experiments, it became evident that the heat transfer from the fuel layer itself is capable of melting the ice at a faster pace than the heat transfer from the flame. Thus, a void is shaped in the circumference of the ice wall, and this void is referred to lateral cavity. Also, temperature measurements of the fuel layer obtained during the burning of the fuel showed a temperature gradient both in the vertical and the horizontal direction. These gradients contributed to creating convective motion in the liquid fuel. The driving forces inducing the convective motion were assumed to be surface tension and buoyancy, the Marangoni and the Rayleigh numbers were calculated as the

relevant dimensionless numbers for surface tension and buoyancy, respectively. The results of the analysis showed dominance of natural convection in the first half of the burning period when the fuel layer had a considerable thickness (1.8-0.5 cm). However, Marangoni convection took over as the most significant during the final half of the burning. A sophisticated flow measuring system such as Particle Image Velocimetry (PIV) will be useful to further quantify the flow field and provide fundamental insight into this unique burning behavior specially observed during combustion of a fuel bounded by icy walls.

Chapter 4: Influence of wicking agents on the ignitability and burning rate of ANS crude oil

Experiments were performed to analyze the influences of four types of wicking agents on the burning behavior of water-in-oil mixtures formed from ANS crude oil with water content 20% and 40%. The wicking agents were chosen based on recommendations by the TPOC. Among the agents, jute shows the best enhancement on both the burning rate and efficiency. Also, jute applicability as a wicking agent for ISB in the Arctic is promising from an environmental perspective as it is low-cost, lightweight, and naturally occurring fiber. The after burn clings onto the fibers, which can be easily removed. The controlling parameters related to the reasons for improved performance of jute compared to other fibers would be a useful future study.

Chapter 5: Analysis of rate of flame spread after ignition of ANS crude oil at low temperatures

Ignition at the surface of ANS crude oil bounded by cold walls (bottom and side) and consequent spread of flame was experimentally investigated in this chapter using a 100 cm long and 15 cm wide metal tray. It was observed that the flame spread occurred because of preheating of the liquid ahead of the flame by convective currents driven by surface tension and density differences because of temperature gradients imposed by the leading edge of the flame. The necessity to preheat the liquid in advance of the flame caused the flame propagation to occur in three stages: an induction period where the preheating distance was at a developing stage, a quasi-steady flame spread region where the flame propagation rate reached its maximum value and the preheating distance was relatively constant, and finally an end region where the preheating distance was blocked because the flame reaches the end of the tray. The three stages were also influenced by flame pulsations in some cases. The influence of boundary condition (water sub layer and adiabatic case), oil thickness (3 mm – 1.5 cm), and weathering were analyzed using image processing (visible and IR), and in-depth temperature measurements. The average rate of flame spread was in the range of 2 cm/s for fresh ANS crude oil and decreased to 0.7 cm/s after 5 days of weathering (21.3% loss by mass).

Chapter 6: Burning behavior in large scale indoor (~1m) and outdoor trials (~1.5 m)

A total of 2 indoor and 3 outdoor large-scale experiments comprising of burning ~1.5 cm thick ANS crude oil in a square cavity (~1 to 1.5 m) were performed during this study. The geometry changes (lateral cavity) observed and investigated at the small scale (chapter 3) were also observed in the large scale tests. The major finding from the tests was that the distance of the fuel layer from the surface defined as the ullage significantly influences the burning behavior. As the ullage decreases from 20 cm to 10 cm, the overall burning rate per unit area decreased by 10%, and lateral cavities increase by 63%. However, with only 2 large-scale tests performed at two different initial ullage conditions, the results though fascinating are still inconclusive and necessitate further experimentation.

Chapter 1: *Ignitability of ANS crude oil at low temperatures*

1.1 Summary

This chapter discusses a series of experiments conducted using a novel experimental platform and procedure to determine material property data for characterization of the ignition of crude oil in arctic conditions. The experimental data was used to clarify the ignition characteristics of different crude oil-and-water emulsions comparatively. Time to piloted ignition, critical heat flux for sustained ignition, and in depth temperature profiles for Alaska North Slope (ANS) crude oil and its saline emulsions (up to 60%) at temperatures ranging from 0°C to -20°C were determined using a set of 84 experimental trials. The results of these experiments revealed several important findings related to the unique problem of an oil spill in the arctic. It was observed that as the degree of emulsification increases the time required and the critical heat flux needed for sustained ignition both increase illustrating an additional difficulty of crude oil remediation in the remote areas of the arctic. It was also found that the initial temperature of the oil had no effect on the critical heat flux for crude oil or emulsions within the range of temperatures tested, rather a decrease in oil temperature only delayed the time of ignition. A unique finding of this research shows that as the applied external heat flux increases beyond the critical heat flux the thermal inertia of the fuel increased, delaying the expected time to ignition, caused by the large temperature gradient formed between the oil and boundary and the presence of water and salt in the oil-and-water emulsions. The role of these characteristics in an arctic spill scenario is discussed.

1.2 Introduction

When oil spills occur in the arctic they present a unique challenge for remediation due to the remoteness of the location, extreme cold temperatures, and the presence of ice below or amongst the spilt oil. Each of these challenges delay initial response and slow the time to successful intervention with heavy machinery for mechanical recovery [1]. In these circumstances, *In Situ Burning* (ISB) defined as igniting and burning the oil spill in place has been shown to be an effective means cleanup [2]. Several factors, however, greatly affect the degree of success of ISB such as weathering, level of emulsification, and the presence of a cold substrate in the form of sea water, and sea ice. Previous studies have examined the effects of weathering and emulsification, usually in combination, on the ignition characteristics of crude oil and have explored igniters to initiate ISB. However, these studies have been conducted at ambient temperatures above that of the arctic [3-5]. The objective of this study is to systematically analyze emulsification and influence of a cold boundary on the ignition behavior of an oil slick. A series of experiments are conducted using an experimental platform and procedure developed to determine material property data for characterization of the ignition of crude oil in arctic conditions. The experimental data is then used to clarify the ignition characteristics of different crude-oil-water emulsions comparatively.

1.3 Experimental apparatus and procedure

Experiments were performed using a specially engineered vessel whose walls were cooled and maintained at sub-zero temperatures to simulate arctic boundary conditions on a layer of fuel. Alaska North Slope (ANS) crude oil was used in all experiments. The properties are discussed in Farahani et al. [6]. In-depth temperature profiles, time to ignition, and applied external heat flux data were used to determine ignition probability and minimum ignition requirements for ANS crude oil at various temperatures and levels of emulsification.

1.3.1 Apparatus

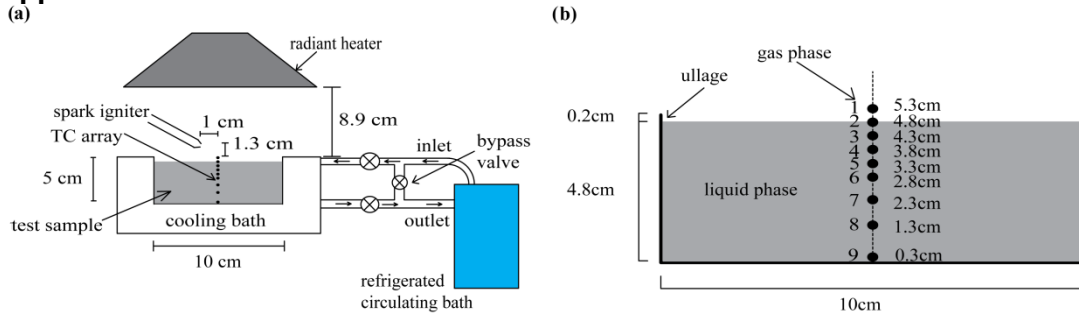


Fig. 1.1 a) Experimental setup. b) Cross section of ignition vessel indicating location of fuel layer and thermocouples. Fixed dimensions are shown.

Figure 1.1 shows a sketch of the experimental apparatus. An external refrigerated circulating bath (PolyScience Performance Digital 15L Recirculating Bath model EW-12210-26) was used to circulate coolant (Dynalene HC-50) to a copper coil cooling jacket around a 10cm diameter and 5cm deep thin-walled stainless steel vessel. Both the walls and the bottom of the vessel were cooled to a preset temperature to simulate an oil layer bounded by arctic sea ice. The temperature of the coolant fluid was set and monitored by the circulating bath ensuring a constant temperature boundary condition at the walls and bottom of the ignition vessel. External heat flux was applied to the fuel surface by a radiant heater [7] at a distance of 8.9 cm. The heat flux from the heater to the fuel layer was uniform and could be varied in steps of 0.1 kW/m^2 increments by adjusting the current to the heater. The current to heat flux calibration was achieved using a water cooled heat flux gauge (Medtherm). A spark igniter was placed 1.3 cm above the fuel surface offset from the centerline by 1 cm. During testing the spark igniter was cycled for 10 seconds of active spark followed by a 10 second off cycle. This procedure prevented observed ignition because of localized heating from a constant spark. A thermocouple array was placed along the centerline of the fuel layer at heights (from the bottom) of 0.3 cm, 1.3 cm, 2.3 cm, 2.8 cm, 3.3 cm, 3.8 cm, 4.3 cm, 4.8 cm, and 5.3 cm. An additional thermocouple was placed against the vessel wall. The height of the fuel layer was set at 4.8 cm for all experiments. The small ullage of 2 mm allowed for slight expansion that was observed in some experimental trials. The central thermocouple array thus provided temperature data at eight locations in the oil layer and one in the gas phase at 5.3 cm, 5 mm above the liquid surface.

A total of 84 experiments were conducted at oil temperatures of 0°C , -10°C , and -20°C for emulsion levels of 0% (pure ANS crude), 20%, 40%, and 60%. The emulsions were created using 3.5% salinity salt water by mass. The applied heat flux for each combination oil temperature and emulsion level was varied to determine critical heat flux, or the minimum heat flux needed to achieve sustained ignition. Sustained ignition is defined as flaming combustion across the fuel surface for four seconds or more after the spark igniter is removed [7]. Once the critical heat flux was determined, three additional experimental sets were conducted at heat flux increments above the critical heat flux. Each set of oil temperature, emulsion, and applied heat flux was tested in triplicate with a total of twelve experiments for each combination of emulsion level and temperature.

1.3.2 Test sample preparation

Oil samples were pre-conditioned in sealed 800ml vessels in a recirculating bath set at the required temperature for 24 hours to ensure uniform temperature throughout the sample. Oil-and-water emulsions were prepared using a closed-loop mixing system until a stable emulsion was achieved, as indicated by the sample remaining emulsified after 48 hours. The system was closed to ensure no weathering during emulsion preparation. Most crude oils and petroleum

products require weathering (evaporation) to form stable water-in-oil emulsions [8, 9]. Studies show that at warm temperatures (15°C) ANS crude must evaporate to lose more than 15% of volume to form stable emulsions, but at freezing temperatures even fresh ANS crude forms stable emulsions [10]. In the current study both temperatures of the sample and the testing environment were below the freezing temperature (0 to -20°C), and emulsions formed with fresh ANS crude were deemed stable.

1.3.3 Challenges in experimental procedure

Due to the nature of testing at arctic temperatures several factors contributed to the difficulty encountered during experimentation. Firstly, due to the cooling system used to cool the vessel containing the fuel, the vessel itself had little mobility which required the test sample be poured or scooped into the vessel located under the conical heater. Secondly, as the initial temperature of the test sample decreased and as the level of emulsification increased, the viscosity of the oil increased. At -10°C and -20°C the 20% and 60% emulsions resisted pouring from the conditioning containers and were scooped into the ignition vessel. Due to the high viscosity of the oil for these trials it was difficult to achieve a uniform surface leading to some uncertainty of initial ullage height.

1.4 Results and analysis

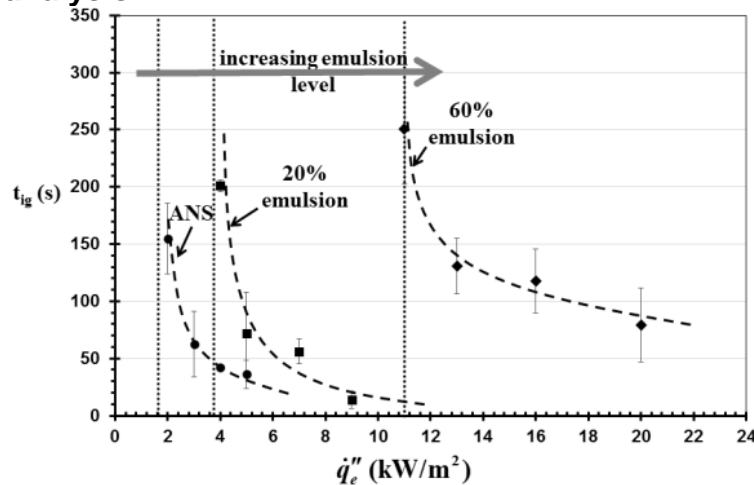


Fig. 1.2: Influence of level of emulsification on time to ignition at $T_{\infty} = -10^{\circ}\text{C}$. The critical heat flux is shown as a vertical dotted line

Figure 1.2 shows the time to ignition as a function of the external heat flux for pure ANS crude oil and emulsions of 20% and 60% maintained at -10°C. Each data point is an average of three experimental trials, with variation shown in the form of error bars. Figure 1.2 shows that as the heat flux decreases, the time to ignition increases, up to a point where no ignition is possible. This threshold heat flux between ignition and no ignition is defined as the critical heat flux [11] and indicated by the vertical dotted lines in Fig. 1.2. Due to the low temperature of ANS and the cold walls pure ANS crude oil shown to be otherwise ignitable at ambient temperatures [4, 5, 12] requires a critical heat flux of 1.87 kW/m² for sustained ignition. The main reason for this change is because of the cold side-walls which create significant thermocapillary convective effects. The boundary condition thus reduces the flammability of pure ANS. As the ANS is emulsified, the critical heat flux required for sustained ignition increases significantly up to 4.06 kW/m² for 20% emulsion and 10.55 kW/m² for 60% emulsion. The water content in the oil affects the ignition process by increasing the effective thermal capacity of the fuel sample (including latent heat requirement). Further, the released water vapor will dilute the fuel vapor effectively increasing the gas-phase induction time. Thus, critical heat fluxes are found to increase with

increasing moisture content [13-15]. Secondly, addition of water increases the thermal diffusivity of crude oil, mainly because of the higher conductivity of water compared to ANS [16]. This causes an increase in heat losses in-depth with an increase in water content also leading to an increase in the critical heat flux with increasing emulsion levels as shown in Fig. 1.2. These primary controlling parameters are further analyzed using in-depth temperature profiles.

1.4.1 In-depth temperature profile

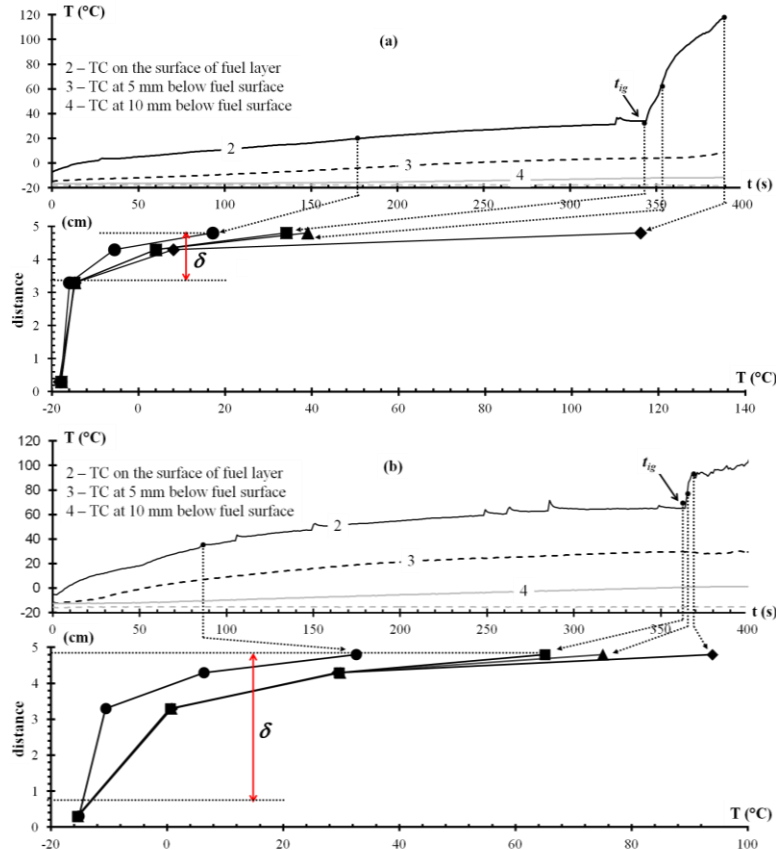


Fig. 1.3: (a) Time-temperature history and in-depth temperature profile at critical heat flux and -20°C for (a) pure ANS crude oil and (b) 20% emulsion

Figure 1.3a and Figure 1.3b shows in-depth temperature profiles obtained with critical heat flux application for pure ANS crude oil and 20% emulsion both at -20°C. The top line chart in each of the two figures shows the temperature recorded by four thermocouples as a function of time. The time to 50% temperature at ignition (T_{ig}), time to ignition (t_{ig}), maximum increase in temperature per unit time (dT/dy) following ignition, and local temperature maxima immediately following ignition are indicated in the figures. The lower line chart shows the in-depth temperature profile corresponding to these time instances. Figure 1.3 shows the in-depth heat transfer during the ignition process. Note that the wall temperature (not shown) is constant during the entire process because of the circulating coolant bath that maintains the temperature at a fixed pre-determined value of -20°C in this case. Firstly, Fig. 1.3a shows that for pure ANS the thermal wave does not penetrate to the bottom of the vessel showing that the fuel layer behaves as thermally thick during the ignition process. Further, the thermal penetration depth (δ) for ANS is only ~1.3 cm showing that ~1.5 to 2 cm oil layers trapped in ice in the arctic will behave as thermally thick. The penetration depth however increases to ~3.0 cm for the case with 20% emulsion maintained at -20°C. This difference is mainly because of an increase in the

thermal conductivity of the emulsion as discussed by Wu et al. [5]. Further, because saline water was used in the current study an additional increase in conductivity because of the presence of salt [17] is also possible. The thermal conductivity of saline water/ice increases with a decrease in temperature [17]. This may lead to significant in-depth conduction heat losses with increasing emulsion levels and decreasing temperatures. A qualitative comparison of the in-depth surface heat loss as a function of temperature of the fuel layer and level of emulsification is shown in Fig. 1.4.

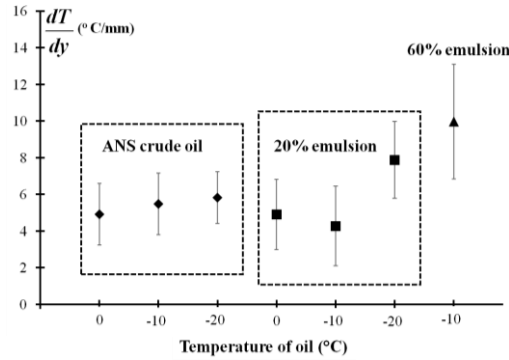


Fig. 1.4: Average in-depth heat loss at time of ignition for pure ANS crude oil, 20% emulsion and 60% emulsion at different initial temperatures.

Figure 1.4 shows the in-depth heat loss, from the surface of the oil layer immediately to the layer below for different experimental trials. The heat loss is calculated using the data obtained from the temperature profiles obtained at t_{ig} . Each data point is an average of twelve experimental trials at each reported temperature, with variation shown in the form of error bars. In the case of pure ANS crude oil, as the temperature is lowered, the in-depth conduction loss at the surface increases. This is mainly because of an increase in viscosity and a corresponding reduction in convective motion with a decrease in temperature. Marangoni and the Rayleigh numbers have been used as the relevant dimensionless groups for thermocapillary and natural convection, respectively [18]. These dimensionless numbers can be represented as:

$$Ma = \frac{\sigma_T R \Delta T_h}{\mu \alpha} \quad (1)$$

and,

$$Ra = \frac{\beta g L^3 \Delta T_v}{\nu \alpha}, \quad (2)$$

where $\sigma_T = \frac{\partial \sigma}{\partial T}$ is the change of surface tension per °C, R is the radius of the cavity, L is the thickness of the fuel, g is the acceleration due to gravity, and β , μ , ν , and α are thermal expansion, viscosity, kinematic viscosity and thermal diffusivity of the liquid, respectively. As shown in Figure 1.3, only a fine layer of liquid at the surface is really important in the ignition process. A recent study by Farahani et al. [19] shows dominance of Marangoni convection with such thin layers especially if bounded by cold walls as in the current study. Marangoni convection causes net force acting at the surface drawing the hot liquid away from the heated area causing colder liquid from below to take its place. The movement of the liquid sideways is further enhanced by the cold wall. However, with a reduction in the overall temperature of the ANS crude oil, the viscosity increases causing a reduction in the Marangoni convection. This results in greater in-depth heat penetration as shown in Figure 1.4. With the addition of saline water the viscosity increases even more. In fact with the 60% emulsion the oil becomes so thick that it has to be scooped with a spatula into the vessel. This significant increase in viscosity results in further increase in the in-depth heat transfer as shown in Fig. 1.4.

1.4.2 Thermal inertia

An important characteristic of a fuel, the thermal inertia (expressed as $k\rho c$), is a measure of a materials resistance to change in temperature and is a key factor in predicting the time to ignition. The property has been used as a parameter for crude oil flammability, especially because it can be determined easily from a bench scale test and can be applied to ignition and flame spread models to evaluate criteria for ISB in the field [5]. Eq. 1 shows that for constant heat exposures (ignoring heat losses), fuels with higher values of $k\rho c$ require longer exposure times to achieve ignition, where t_{ig} is the time to ignition, T_{ig} and T_o are the surface temperature at ignition and temperature of the surroundings respectively, \dot{q}_e'' and $\dot{q}_{o,ig}''$ are the applied heat flux and critical heat flux respectively, and $k\rho c$ is the thermal inertia of the crude oil [20]. Eq. 3 solved for the thermal inertia term results in Eq. 4 where t_{ig} , T_{ig} , T_o , \dot{q}_e'' and $\dot{q}_{o,ig}''$ are experimentally measured to calculate $k\rho c$.

$$t_{ig} = \frac{\pi k\rho c (T_{ig} - T_o)^2}{4(\dot{q}_e'' - \dot{q}_{o,ig}'')^2} \quad (3)$$

$$k\rho c = \frac{4t_{ig}(\dot{q}_e'' - \dot{q}_{o,ig}'')^2}{\pi(T_{ig} - T_o)^2} \quad (4)$$

A key assumption made during the development of Eq. 3 is the oil layer behaves as an inert upto the point of ignition. The time taken to reach a particular surface temperature (t_{ig}) under the action of a constant heat flux can then be calculated [21]. In the case of liquid ignition convective motion due to surface tension driven flows or Marangoni convection [5, 22-24] are important to consider. This effect has not been considered in Eq. 3. The implications of this omission especially with the presence of the cold surrounding walls which create a significant thermal gradient are discussed by comparing the trends of experimentally determined $k\rho c$ values for pure ANS and ANS-water emulsions shown in Fig. 1.5.

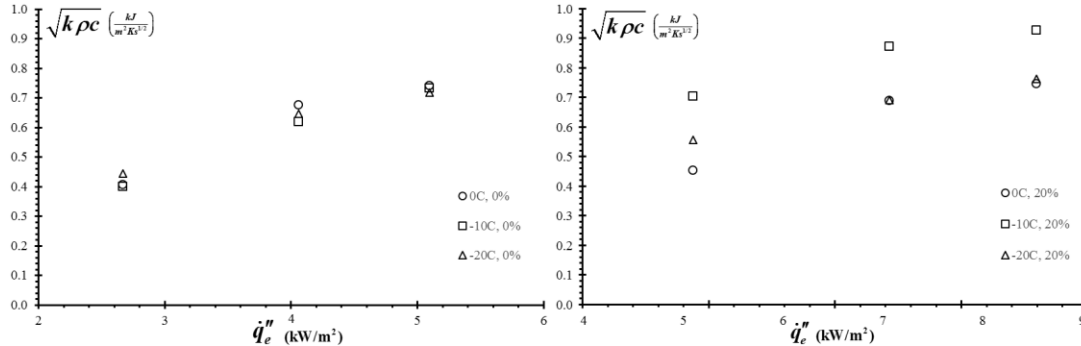


Fig. 1.5: Thermal inertia vs. external heat flux. (a) Pure ANS at different temperatures. (b) 20% emulsion

Figure 1.5a shows the average calculated value for $k\rho c$ for ANS crude at 0°C, -10°C and -20°C using Eq. 4. It is observed that as the external heat flux increases so does the thermal inertia. An explanation for this behavior is that as the applied external heat flux, and therefore the amount of energy transferred into the fuel, increases the temperature of the fuel increases creating a larger temperature gradient between the fuel and the boundary of the container. Although the exact nature of the internal fluid flow was not visualized in this study it is assumed that as the temperature gradient between the fuel and the boundary increases so do internal convective flows which promotes cooling of the fuel by mixing with the colder fluid located below the thermal penetration depth and the cooled wall of the vessel. This convection induced mixing delays the expected time to ignition resulting in an increase in the thermal inertia. This is a unique arctic situation where oil may be contained within ice.

1.4.3 Implications to an Arctic oil spill

Any oil spill in the arctic regions has great potential for creating a detrimental impact on the arctic ecosystem and would require significant effort, equipment, and funding to successfully remediate with little ecological damage. As oil is spilt it can interact with surrounding environment in a variety of ways, each presenting a unique challenge to oil remediation. Examples of these interaction can include, but are not limited to, spills in open water, on top of ice or snow cover, trapped within an ice channel, encapsulated in pockets within the ice cover, or completely entrapped below the ice cover [25]. Remediation or recovery methods for spilt oil in these cases typically include either mechanical recovery or In-Situ Burning (ISB). In mechanical recovery large vessels equipped with heavy equipment can herd and collect the oil using skimmers or suction, but given the remoteness of the location, presence of ice cover, seasonal darkness, and extreme temperatures, the use of mechanical recovery has serious disadvantages [26]. This makes ISB a feasible option for oil spill cleanup in the arctic. However, a successful ISB in the arctic necessitates a fundamental understanding of the ignition, flame spread and burning behavior of crude oil in the presence of ice. The current study is a *first* step in understanding the ignition of oil in this setting. When oil is contained by a cold boundary of ice or saline water it will impose similar implications on the ignition characteristics of the oil as the experimental apparatus used in this study.

The results of the study show that igniters developed for use in ISB on water will need significant modification to work in the arctic. The ignition experiments show that the ignition energy is *doubled* with the presence of a cold boundary. The reason for this increase is not limited to a decrease in temperature alone, but also because of thermocapillary convection and an increase in thermal conductivity because of salt migration in oil-water emulsions. These controlling parameters need further investigation for proper design and construction of igniters for ISB in arctic. The implications of these effects on flame spread and burning also require further investigation.

1.5 Conclusions

A series of experiments were conducted using an experimental platform and procedure developed for this study to determine material property data for characterization of the ignition of crude oil in arctic conditions. The experimental data was used to clarify the ignition characteristics of different crude-oil-water emulsions comparatively and will be used as future input data in mathematical models for flame spread.

Based on the experiments conducted it was observed that the minimum external heat flux, or the measure of the minimum energy required to sufficiently heat the oil and provide enough gaseous fuel for ignition and sustained burning, required for sustained ignition of ANS oil and emulsions was independent of the initial oil temperature or temperature of the surrounding but rather a function of degree of emulsification with higher levels of heat flux required for higher percent emulsions.

At arctic temperatures the thermal inertia of the crude oil increases as applied external heat flux increases. Although the exact nature of the internal flow below the surface was not specifically visualized in this research it is suspected that as the temperature gradient from the fuel surface to fuel below the penetration depth and the gradient between the center of the fuel surface to the vessel boundary increase so do internal convective flows, providing cooling and thus delaying time to ignition. This is especially important in cases where crude oil may be trapped in ice. It was also observed that the presence of water and salt in the emulsions contributed to a delay in time to ignition and an increase the thermal penetration depth of the fuel due to the presence of water and salt.

1.6 References

1. Buist, I., *Window-of-opportunity for in situ burning*. Spill Science & Technology Bulletin, 2003. **8**(4): p. 341-346.
2. Buist, I.A., Potter, S.G., Trudel, B.K., Shelnutt, S.R., Walker, A.H., Scholz, D.K., Brandvik, P.J., Fritt-Rasmussen, J., Allen, A.A., and Smith, P., *In situ burning in ice-affected waters: State of knowledge report*, 2013, Arctic Oil Spill Response Technology Joint Industry Programme (JIP).
3. Putorti, A.D., *Application of the critical radiative ignition flux methodology to high viscosity petroleum fractions*, in *Fire Protection Engineering 1994*, Worcester Polytechnic Institute. p. 75.
4. Walavalkar, A. and Kulkarni, A. *Combustion of mixtures of weathered alaskan crude oils and water under external heat flux*. in *Proceedings of the Twenty-Fourth Arctic Marine Oilspill Program Technical Seminar*. 2001.
5. Wu, N., Kolb, G., and Torero, J.L. *Piloted ignition of a slick of oil on a water sublayer: The effect of weathering*. in *Proc. Combust. Instit.* 1998. Elsevier.
6. Farmahini Farahani, H., Shi, X., Simeoni, A., and Rangwala, A.S., *A study on burning of crude oil in ice cavities*. Proceedings of the Combustion Institute, 2014.
7. Astm-E-1354, *E 1354 standard test method for heat and visible smoke release rates for materials and products using an oxygen consumption calorimeter*, 2009.
8. Astm, *Standard test method for evaluation of the type and viscoelastic stability of water-in-oil mixtures formed from crude oil and petroleum products mixed with water*, in *F30452015*.
9. Fingas, M. and Fieldhouse, B., *Studies on water-in-oil products from crude oils and petroleum products*. Marine pollution bulletin, 2012. **64**(2): p. 272-283.
10. Buist, I.A., Glover, N., Mckenzie, B., and Ranger, R. *In situ burning of alaska north slope emulsions*. in *International Oil Spill Conference*. 1995. American Petroleum Institute.
11. Quintiere, J.G., *Fundamentals of fire phenomena*. 2006: John Wiley & Sons, New York.
12. Putorti, A., Evans, D., and Tennyson, E. *Ignition of weathered and emulsified oils*. in *Arctic and Marine Oil Spill Program Technical Seminar*. 1994.
13. Mikkola, E. and Wichman, I.S., *On the thermal ignition of combustible materials*. Fire and Materials, 1989. **14**(3): p. 87-96.
14. Atreya, A. and Abu-Zaid, M., *Effect of environmental variables on piloted ignition*. Fire Safety Science, 1991. **3**: p. 177-186.
15. Khan, M.M., De Ris, J.L., and Ogden, S.D., *Effect of moisture on ignition time of cellulosic materials*. Fire Safety Science, 2008. **9**: p. 167-178.
16. Wu, N., Baker, M., Kolb, G., and Torero, J.L., *Ignition, flame spread and mass burning characteristics of liquid fuels on a water bed*. Spill Science & Technology Bulletin, 1996. **3**(4): p. 209-212.
17. Pringle, D., Eicken, H., Trodahl, H., and Backstrom, L., *Thermal conductivity of landfast antarctic and arctic sea ice*. Journal of Geophysical Research: Oceans (1978–2012), 2007. **112**(C4).
18. T. Yumoto, A. Takahashi, and T. Handa, *Combustion behavior of liquid fuel in a small vessel: Effect of convective motion in the liquid on burning rate of hexane in the early stage of combustion*. COMBUSTION AND FLAME, 1997. **30**: p. 33-43.
19. Farahani, H.F., Jomaas, G., and Rangwala, A.S., *Effects of convective motion in n-octane pool fires in an ice cavity*. Combustion and Flame, 2015.
20. Fernandez-Pello, A.C., *The solid phase*, in *Combustion fundamentals of fire*, G. Cox, Editor. 1995, Academic Press: New York. p. 32 -100.
21. Simms, D.L., *On the pilot ignition of wood by radiation*. Combust. Flame, 1963. **7**: p. 253-261.

22. Glassman, I. and Dryer, F.L., *Flame spreading across liquid fuels*. Fire Safety Journal, 1981. **3**(3): p. 123-138.
23. Higuera, F., *Steady thermocapillary-buoyant flow in an unbounded liquid layer heated nonuniformly from above*. Physics of Fluids, 2000. **12**(9): p. 2186-2197.
24. Ross, H.D., *Ignition of and flame spread over laboratory-scale pools of pure liquid fuels*. Progress in Energy and Combustion Science, 1994. **20**(1): p. 17-63.
25. Potter, S., Buist, I., Trudel, K., Dickins, D., and Owens, E., *Spill response in the arctic offshore*. Prepared for the American Petroleum Institute and the Joint Industry Programme on Oil Spill Recovery in Ice. American Petroleum Institute, Washington, DC, 2012.
26. Jensen, H.V. and Mullin, J.V., *Morice—new technology for mechanical oil recovery in ice infested waters*. Marine pollution bulletin, 2003. **47**(9): p. 453-469.

Chapter 2: *Characterization of radiative fraction of heat release rate using smoke point of ANS crude oil*

2.1 Summary

ANS crude oil shows 13 distinct smoke point heights during its vaporization ranging from 13 mm (high volatiles) to 1 mm (low volatiles). Smoke point heights are analyzed as a function of oil surface temperature and viscosity. The radiant fraction or the fraction of the total heat that is radiated is estimated for ANS crude oil using the smoke point data. Application of the results towards estimation of the radiant fraction, burning rate, and safe separation distance during ISB is discussed.

2.2 Introduction

The tendency of diffusion flames to soot is measured by the height of the fuel jet (ASTM D1322) at which the luminous diffusion flame breaks open at its apex and emits a stream of soot. The smaller the flame height at the soot emission condition or the smaller the mass flow rate the greater the tendency to soot. Smoke point (also called sooting height) of a fuel is the maximum height of a smokeless laminar flame (mm) burning in air at which if the flow rate is increased, the fuel will start to produce soot. Another definition (and more applicable to fire safety) is the heat release rate at which smoke just begins to be released from the flame tip.

Smoke point is a simplified ranking scheme for soot production and several experimental platforms using laminar diffusion flames [1-9], turbulent diffusion flames [10], stirred reactors [11], and laminar premixed flames [12] have been developed to experimentally determine its value. Smoke-point can be easily determined for gases and vapors by adjusting the flow rate of the fuel from a simple burner. For liquid fuels a wick-fed lamp (ASTM D1322) [3] is used. A fuel dependent parameter like laminar smoke point can be used to model the radiative losses due to soot formation during in-situ combustion. Further, it can also be used as a flammability ranking parameter for different blends (types) of crude oil, and quantify the influence of weathering and emulsification.

It has been shown that smoke point [5, 7, 13] can provide a convenient measure of the flame radiant fraction. For modeling purposes, radiant fraction of the total heat release rate can be found empirically by a function of the laminar smoke point [5]:

$$\chi_{rad} = 0.43 - 0.91L_s, \quad (2.1)$$

where L_s is the smoke point height (m) and χ_{rad} is the radiant fraction. Radiant fraction, χ_{rad} , defined as the ratio of radiant heat flux from the flame to the surroundings to the total heat flux released by the flame, which has been used as a primary input parameter to predict burning rate, efficiency, safe separation distance and time to boil-over in a large pool fire. While the constants may vary based on literature sources, in general, the linear relationship between the smoke point of a fuel and the radiative fraction proves to be a useful engineering formula to assess the safe separation distance from a pool fire [14].

A methodology to rank a fuel based on its capability to radiate more (or less) heat is of significant importance in ISB applications. Depending on the fuel type and flow conditions, the radiant fraction can range from a few percent to more than 50% [14-16]. The common approach to find the radiant fraction of a fuel is to measure the radiant heat flux emitted from the flame of a large pool fire using instrumentation such as heat flux gauges. This approach could be

complicated and expensive, as a large amount of heat flux gauges are required to be set around the flame.

Prior smoke point studies reported in literature (see [17]) mostly focused on the single component fuel, or up to two-component mixture. In this study, the first of its kind, the smoke point of a highly multicomponent and viscous fuel like ANS crude oil is measured and the results are used to show the validity of empirical correlation (Eq. 2.1). The corresponding radiant fraction χ_{rad} is compared with large scale experiments discussed in Chapter 6. The results can be used to estimate the safety distance, the radiant fraction and the likely burning rate when a spill response is required.

2.3 Experimental Setup and Procedure

Initial trials with the standard apparatus of an ASTM smoke point lamp [18] were attempted; however, proved unsuccessful because the fuel flow rate adjustment by varying the wick length was not precise because of the high viscosity of the crude oil. Therefore, a new test apparatus with a vaporization method [19] was built and improved upon after several iterations in design and construction.

A sketch of the new experimental test apparatus is shown in Fig. 2.1. The setup consists of a 250 ml Pyrex Erlenmeyer flask with a 14/35 ground glass joint (adapter) attached to a 12 cm long, 0.9 cm ID, Pyrex glass tube. The liquid fuel is heated and vaporized by a Bunsen burner placed at the bottom of the flask. The flame height of the Bunsen burner is adjusted by the gas flow rate controller. Along with varying the distance between the flask and the Bunsen burner flame tip, the vaporization rate of the liquid fuel inside flask is finely controlled by adjusting the fuel flow rate to the Bunsen burner. The flame from the glass tube is surrounded by a 61 cm long, 20 cm ID, polycarbonate outer-tube with a fine mesh screen attached to its bottom, which reduces the air draft effects. Similarly, the flame from the Bunsen burner is surrounded by a stainless steel perforated screen (63% open). To maintain a stable heating affect from the Bunsen burner, a heat containment disk is equipped around the flask. A metric scale is attached to the outer wall of the polycarbonate tube behind the flame of smoke point for its height measurement. A second metric scale is installed in front of the flame (outside polycarbonate tube, as shown in Fig. 2.1) to precisely align the camera with the flame.

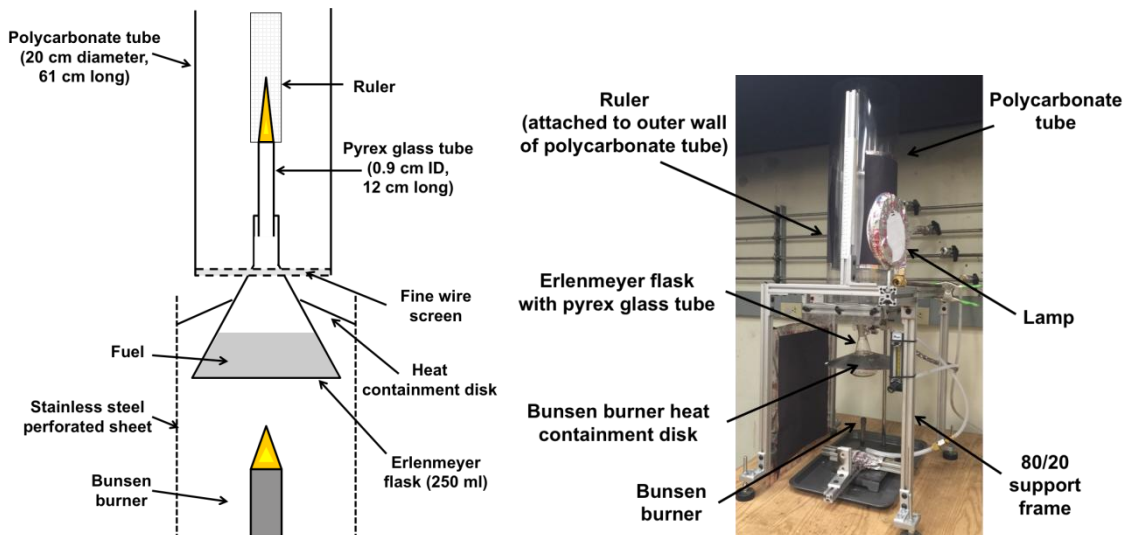


Fig. 2.1: Experimental setup for smoke point test
 (Note: SS perforated sheet for Bunsen burner is not shown on right for a clear view)

With the Bunsen burner ignited, the fuel in the flask begins to boil. Once the vapor coming out of the flask is stable, it is ignited by a lighter and the polycarbonate tube is placed. The fuel vapor flow rate, which determines its flame height, is controlled by the Bunsen burner. The camera is positioned to be level with both rulers for smoke point height measurement. The video is then reviewed through frame-by-frame analysis, looking for the flame height in which smoke begins to emerge. The flame shape to determine the smoke point [18] is shown in Fig. 2.2, along with a picture of a smoke point captured by the camera during the test.

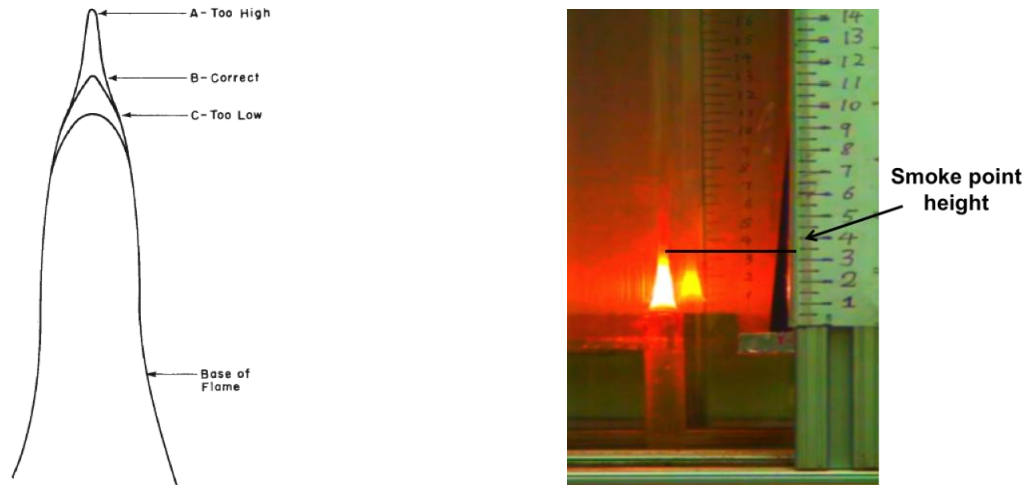


Fig. 2.2: Sketch for smoke point determination [18], left; measured smoke point (3.3 cm for a mixture of 10% Toluene 90% Iso-octane), right.

The apparatus is validated using measurements of smoke point heights of both single and double component fuel mixtures, and shows reasonable percentage deviation (1-16%) compared with reference values obtained from ASTM D1322 [18] standard. Three single component fuels (pentane, iso-octane and dodecane) with the boiling temperatures of 36, 99 and 216 °C are measured with the apparatus. Seven mixed solutions (double component) of toluene and iso-octane with very close boiling temperatures of 111 and 100 °C, respectively, are also measured. All measurement are repeated three times. The test matrix, fuel properties, experimental results of smoke points are shown in Table 2.1. Comparison with smoke point heights reported in literature [18] show good agreement.

Table 2.1: Test results of single and double components fuel

Fuel Type	Trial Number	Initial Volume (mL)	Trial Duration (s)	Boiling Point (°C)	Smoke Point (cm)		
					Reference	Observed	% Deviation
IsoOctane	1	50	600	99.5	5.43 +/- 1.3	5 +/- 1	8%
	2	75	900			5 +/- 1	8%
	3	75	900			5 +/- 1	8%
	4	100	660			5 +/- 1	8%
	5	100	660			5 +/- 1	8%
	6	125	1260			5 +/- 1	8%
	7	140	960			5 +/- 1	8%
	8	150	600			5.5 +/- 1	1%
	9	150	660			4.7	13%
	10	150	900			4.6	15%
	11	150	1200			4.8	12%
	12	150	1260			4.7	13%
	13	200	1200			5.5 +/- 1	1%
Pentane	1	100	540	36	16.3 +/- 2.5	15.5	5%
	2	150	900			15.5	5%
Dodecane	1	100	2700	214 - 218	10.7 +/- 2.4	9 +/- 1.5	16%
	2	110	2700			9 +/- 1.5	16%
40% Toluene 60% IsoOctane	1	100	1200	N/A	1.47	1.3	12%
25% Toluene 75% IsoOctane	1	100	720		2.02	1.8	11%
20% Toluene 80% IsoOctane	1	100	600		2.27	2	12%
15% Toluene 85% IsoOctane	1	100	780		2.58	2.2	15%
10% Toluene 90% IsoOctane	1	100	660		3.02	3.3	9%
5% Toluene 95% IsoOctane	1	100	660		3.54	3.8	7%

The smoke points of two-component mixtures at various mixing ratios are also shown in Fig. 2.3. It is clear that the apparatus is capable to measure the smoke point of a mixture with a reasonable experimental uncertainty range.

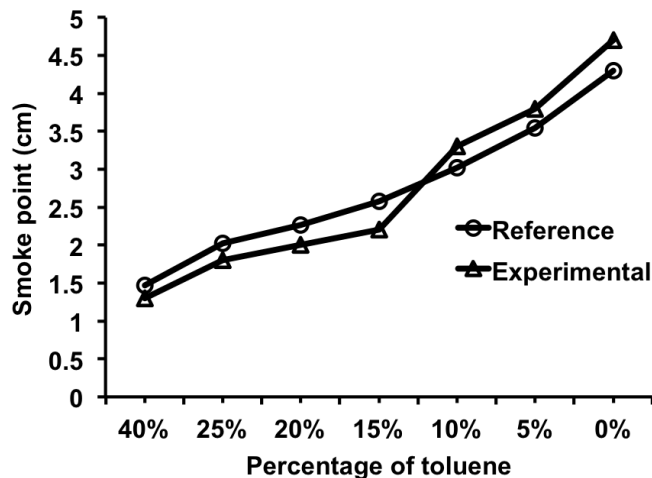


Fig. 2.3: Measured smoke points of double components fuel compared with literature [18].

To find the smoke point of crude oil precisely, it is important to separate a small group of lighter components from the heavier components gradually. A slow and precise control of the heat input from the flame of Bunsen burner to the crude oil is used, which allows the components with similar vaporization temperatures to vaporize. A typical sweep of one test usually lasts around 2 hours.

2.4 Experimental Results and Analysis

2.4.1 Smoke point of ANS crude oil – Relationship with oil surface temperature

Figure 2.4 shows a typical temperature sweep to determine the smoke point of ANS crude oil with the apparatus shown in Fig. 2.1. During the experiment, the Bunsen burner is maintained at a certain small flow rate and any observable smoke points are recorded. The Bunsen burner is kept constant at this methane flow rate until vaporization of the crude oil could no longer sustain a laminar flame. At this point, the flow rate of Bunsen burner is increased slightly. The Bunsen burner is then kept constant at a new flow rate and the observable smoke points are recorded. When the crude oil vapors could not sustain a flame again, the flow rate is increased again by the same rate. This process is repeated until the end of the experiment and all observable smoke points are recorded. If an increase in flow rate could not result in a stable flame, the flow rate is increased at the same rate again until a stable flame could be produced.

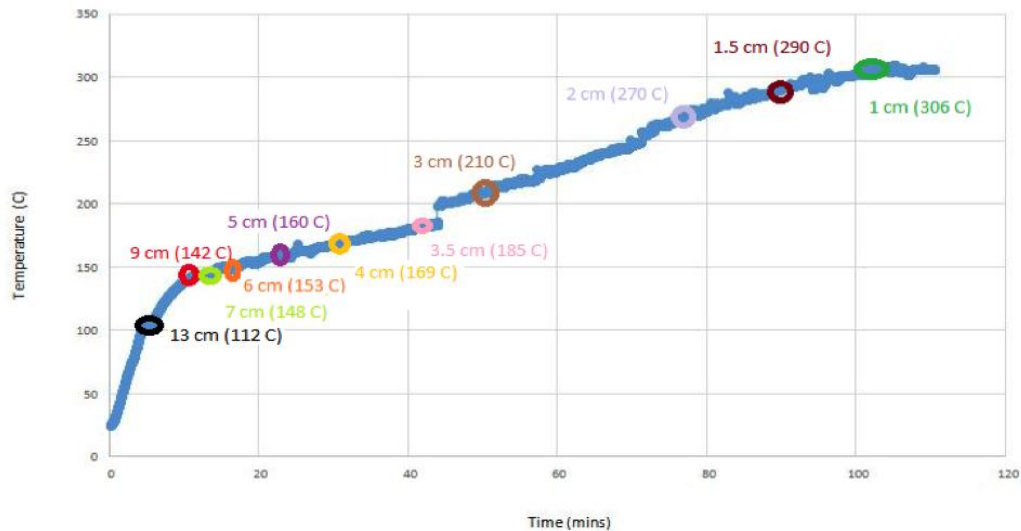


Fig. 2.4: Measured smoke points of double components fuel compared with literature [18].

The temperature plateaus shown in Fig. 2.4 represent the stable oil surface temperatures at different times for 2 hours. The circular data points indicate smoke points of ANS oil-vapor components with similar vaporization temperatures. Repeated experiments are performed and 13 smoke points were measured. Figure 2.5 shows the smoke point of ANS crude oil as a function of surface temperature of ANS crude oil. The flames prior, at, and post smoke point (per ASTM D1322 measurement criteria) are also shown.

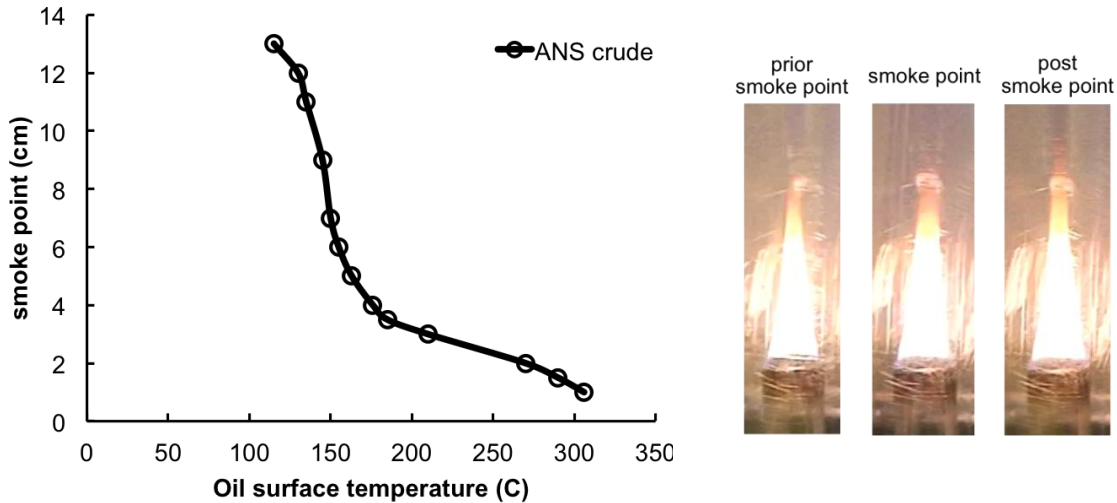


Fig. 2.5: Smoke point of ANS crude oil as a function of oil surface temperature, left; Photograph shows the observed smoke point height at 3 cm for ANS crude oil, right.

Figure 2.5 shows a total of 13 smoke points that were observed for ANS crude oil. Three repeat experiments were performed with the same batch of crude oil and the data points were within a $\pm 3\%$ showing good consistency. As shown in Fig. 2.5, the volatilization process of ANS crude oil results in stable smoke point heights varying from 13 cm (lighter components) to 0.4 cm (heavier components). The oil surface temperature correspondingly increases from 115°C to 306°C.

For an ISB operation, the results show that sootiness of the fuel will increase as the oil-layer burns. During ISB, the oil-layer is exposed to flame heat flux which causes volatilization. Because of the multicomponent nature of crude oil, the lighter volatiles are able to vaporize first followed by the heavier components. The heavier components have a lower smoke point representing increased soot and resulting in an increasing radiant fraction χ_{rad} , which is consistent with observations in ANS crude oil burns reported in an earlier study performed by WPI¹. Intermediate and large scale tests performed during the course of this research show that lighter (less viscous) and less sooty components burn first and as the oil becomes more heavy (more viscous), the oil produces more soot.

2.4.2 Smoke point height of ANS crude oil – Relationship with viscosity

Samples were collected at each smoke point for viscosity measurement. The samples were collected by stopping the experiment, opening the cap and extracting a 10 ml sample from the surface using a syringe. The samples were then taken to the rheology laboratory at WPI for viscosity measurement. Figure 2.6 shows the smoke point as a function of the ANS crude oil viscosity. The results show that the lighter components that evaporate first are also the least viscous (~15 cP) followed by the heavier components that have a higher viscosity up to 85 cP.

¹ Burning Behavior of Oil in Ice Channels, (2014) Project Number: OSSR-1007AA

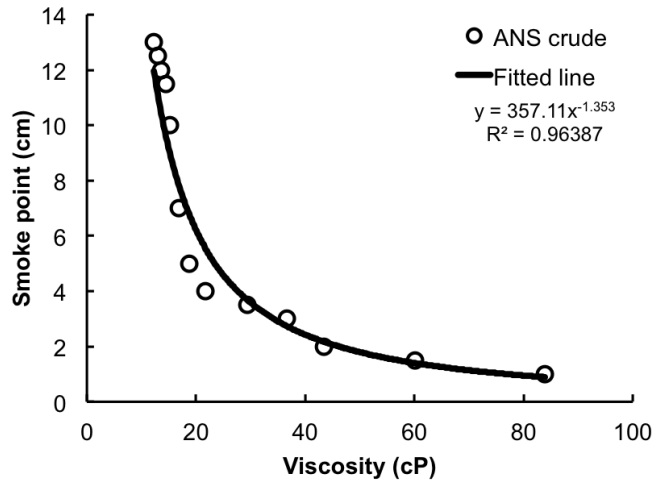


Fig. 2.6: Smoke point of ANS crude oil as a function of oil viscosity.

2.4.3 Radiant fraction

Figure 2.7 shows the radiant fraction (χ_{rad}) of ANS crude oil calculated using Eq. (2.1). Based on the smoke point height, χ_{rad} varies between 0.3 to 0.42. Comparison with large scale tests (discussed in Chapter 6) show that the radiative fraction is slightly overestimated.

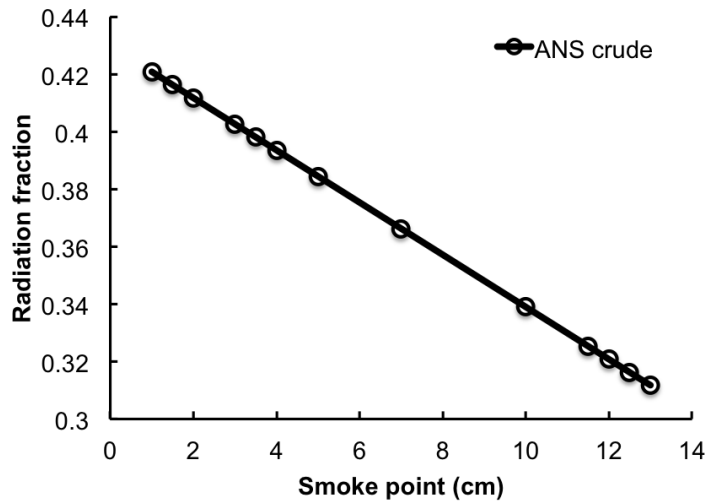


Fig. 2.7: Estimated flame radiant fraction (Eq. (1)) of ANS crude oil as a function of smoke point.

2.5 Conclusions

During ISB in the arctic, an oil slick will burn depending on the exposure to heat from the combustion process. The exposure to heat will depend on the fire environment to which the oil is exposed (oil bounded by an ice cavity, oil in snow, oil floating on sea-water etc). Its volatilization rate will be different depending on the environmental condition. The experimental platform described in this study, provides a simple engineering tool to predict the range of smoke point heights and corresponding radiative fraction of the total heat release rate using a simple bench scale test. The results show that:

1. Smoke points varied from 13 cm to 1 cm as the oil surface temperature increases from 115°C to 306°C.

2. ANS crude oil at different weathering degrees with the viscosities varying from 12 cP to 84 cP, its smoke point changes from 13 cm to 1 cm.

The results can be used as a guide to estimate the radiant fraction, burning rate, safety distance for the operators when the properties of a hydrocarbon spill (viscosity, vaporization temperature) are known.

2.6 References

1. Minchin, S., *Luminous stationary flames: The quantitative relationship between flame dimensions at the sooting point and chemical composition, with special reference to petroleum hydrocarbons*. Journal of the Institute of Petroleum Technologists, 1931. **17**(1): p. 102-120.
2. Clarke, A., Hunter, T., and Garner, F., *The tendency to smoke of organic substances on burning. Part i*. J. Inst. Pet, 1946. **32**: p. 627-642.
3. Schalla, R. and Hubbard, R., *Formation and combustion of smoke in flames*. NACA report, 1959. **1300**.
4. Kent, J., *A quantitative relationship between soot yield and smoke point measurements*. Combustion and Flame, 1986. **63**(3): p. 349-358.
5. Markstein, G.H., *Correlations for smoke points and radiant emission of laminar hydrocarbon diffusion flames*. Proc. Combust. Instit., 1989. **22**(1): p. 363-370.
6. de Ris, J. and Cheng, X. F., *The role of smoke-point in material flammability testing*. Fire Safety Science, 1994. **4**: p. 301-312.
7. Delichatsios, M., *A phenomenological model for smoke-point and soot formation in laminar flames*. Combustion Science and Technology, 1994. **100**(1-6): p. 283-298.
8. Tewarson, A., *Combustion efficiency and its radiative component*. Fire Safety Journal, 2004. **39**(2): p. 131-141.
9. Allan, K.M., Kaminski, J.R., Bertrand, J.C., Head, J., and Sunderland, P.B., *Laminar smoke points of wax candles*. Combustion Science and Technology, 2009. **181**(5): p. 800-811.
10. Magnussen, B.F. and Hjertager, B.H., *On mathematical modeling of turbulent combustion with special emphasis on soot formation and combustion*. Proc. Combust. Instit., 1977. **16**(1): p. 719-729.
11. Wright, F.J., *Carbon formation under well-stirred conditions, part ii*. Combustion and Flame, 1970. **15**(3): p. 217-222.
12. Schalla, R.L., Clark, T.P., and McDonald, G.E., *Formation and combustion of smoke in laminar flames*. 1954.
13. Lautenberger, C.W., De Ris, J.L., Dembsey, N.A., Barnett, J.R., and Baum, H.R., *A simplified model for soot formation and oxidation in cfd simulation of non-premixed hydrocarbon flames*. Fire Safety Journal, 2005. **40**(2): p. 141-176.
14. Delichatsios, M., De Ris, J., and Orloff, L., *An enhanced flame radiation burner*. Proc. Combust. Inst., 1992. **24**(1): p. 1075-1082.
15. De Ris, J. and Orloff, L., *The role of buoyancy direction and radiation in turbulent diffusion flames on surfaces*. Proc. Combust. Inst., 1974. **15**: p. 175-182.
16. Orloff, L., De Ris, J., and Markstein, G.H., *Upward turbulent fire spread and burning of fuel surface*. Proc. Combust. Inst., 1974. **15**: p. 183-192.
17. Lautenberger, C.W., *CFD simulation of soot formation and flame radiation*, 2002, Worcester Polytechnic Institute.
18. ASTM D1322, *Standard test method for smoke point of kerosine and aviation turbine fuel*, 2013.
19. Tewarson, A., *Prediction of fire properties of material part 1. Aliphatic and aromatic hydrocarbons and related polymers. Technical report NBS/GCR-86/521*, 1986.

Chapter 3: *Geometry changes due to ice melting during combustion*²

3.1 Summary

The effects of convective flows in n-Octane pool fires in an ice cavity were investigated and it was found that a new set of parameters to the classical problem of bounded pool fires arises under these unique conditions. To systematically understand these parameters, two sets of experiments were performed by burning n-Octane in cylindrically shaped ice cavities of 5.7 cm diameter. The first set of experiments was intended to provide a clear understanding of the geometry change of the cavity and displacement of the fuel layer. The results of these experiments showed that the rate of melting of the ice walls were higher in areas where the fuel layer was in contact with ice than in places where the flame was present. Due to the melting of the ice walls, a ring-shaped void was formed around the perimeter of the cavity. In the second set of experiments, the change in the temperature of the fuel layer was measured by use of multiple thermocouples at different locations inside the ice cavity. The results of the temperature analysis showed that the lateral temperature gradient of the fuel layer was an increasing function of time, whereas the vertical temperature gradient was a decreasing function of time. Using these experimental results, two dimensionless numbers (Marangoni and Rayleigh) were calculated. The Marangoni number represents the surface tension driven flows in the fuel layer and the Rayleigh number represents the buoyancy driven flows in the fuel layer. The results of this study showed two major convective phases; in the first half of the burning time, the buoyancy driven flows (Rayleigh) were dominant, while Marangoni convection was dominant in the second half of the burning time. The role of these mechanisms in affecting the flow and melting the ice is discussed.

3.2 Introduction

The study of flow within liquid fuels and pool fires has been of general interest for numerous decades both from a fire safety and from a scientific point of view. The phenomenology and understanding of the controlling mechanisms of liquid flow in pool fires have aided fire researchers in recommending methods to lessen the risks associated with use of liquid fuels. Liquid-phase convection in pool fires was one of the main subjects of investigation in the 1955-1980 research period and extensive studies of ignition and flame spread indicated a connection with the motion in liquid fuels [1, 2]. Specifically, it was shown that the rate of flame spread in liquid fuels with an initial temperature below the fuel's flash point temperature is governed by liquid-phase convection [3]. The liquid fuel flow pattern was first documented by Burgoyne et al. [4] during experiments of flame spread over alcohol pools. They attributed the motion in the liquid to buoyancy effects. Later, studies revealed that both surface tension and buoyancy were the driving forces in the flame spread of the liquids fuels and the surface tension was predicted to be the dominant parameter [5-7]. It was found that the liquid-phase convection in flame spread is driven by surface tension (Marangoni or thermo-capillary flow) initially, after which buoyancy forces and, to a much lesser degree, evaporation and thermal expansion are the driving forces [8]. However, further studies revealed the significant role of surface tension driven flows during the flame spread process [9-11]. Although extensive work on convective flow in the flame spread process has been undertaken, only a few studies have addressed the transport phenomena throughout the burning of pool fires [12-14].

² The contents of this chapter were published as a peer reviewed paper as Farahani, H.F., Jomaas, G. and Rangwala, A.S., 2015. Effects of convective motion in n-octane pool fires in an ice cavity. *Combustion and Flame*, 162(12), pp.4643-4648.

In a typical pool fire (contained with sidewalls), a portion of the heat produced by the flame transfers to the body of the liquid fuel in deeper areas through the rim of the pan, thereby creating local convective flows [15]. When the rigid walls of the pan are replaced with walls of ice, the transport mechanisms are significantly altered. Such a situation will arise for example during clean-up of oil spills in the Arctic using the in-situ burning method [16]. In two previous studies on burning of liquid fuels in ice cavities, a phenomenon that is referred as “*lateral cavity formation*” was observed. During burning of liquid fuels in ice cavities [17] and ice channels [18] (where the fuel was surrounded by walls of ice), the burning fuel was observed to penetrate radially into the ice. The size of the lateral cavity formed on the circumference of the original cavity by the fuel layer was found to vary with fuel type, and different geometric configurations of the ice.

There are some disadvantages to these ice deformations from a practical point of view. For example, the deformation will allow a portion of the oil to drift underneath the lateral cavity. This is presumed to be a potential factor in reducing the burning efficiencies by preventing the exposure of air to the trapped oil. A decrease in the burning efficiency leads to larger amount of oil residue. In addition, the confined residue in the cavity would be harder to collect and, as a result, increase the cost of the post-burn clean-up during in-situ burning operations. In particular, if the residue stays untreated, it could be encapsulated due to freezing of the water in colder seasons and potentially remain in the ecosystem for years.

The hypothesis to explain the formation of lateral cavities is that the penetration into the ice is caused by flows in the liquid fuel layer. The observations made during the previous experiments validated the existence of a flow close to the free surface of the fuel. The driving forces behind the flow in the liquid fuel are anticipated to be buoyancy and surface tension, relating to natural and Marangoni convection, respectively. However, the relative contribution of each of these mechanisms should be studied in order to figure out the influence that these convective flows within the fuel layer have on the formation of lateral cavities in the ice walls.

The objectives of this study are therefore to understand the convective motions in the fuel layer (role of thermocapillary and natural convection) and to relate these to the lateral cavity formations during in-situ burning of liquid fuels in ice cavities. It is envisioned that the results of this study could give a solution toward higher efficiency of in-situ burnings in Arctic condition.

3.3 Experimental Procedure

Figure 3.1 shows the experimental setup with n-Octane in a 5.7 cm diameter ice cavity. Each experiment used an ice block with a circular cavity excavated in its center. The depth (H) and initial fuel layer (L) were chosen based on the data obtained from preliminary tests to prevent overflow and spillage during the burning of the fuel. The ice block was placed on a drip pan on top of a load cell (precision of 0.01 g) to record the mass loss of the fuel. Then, 30 ± 0.1 g n-Octane was added to the cavity (with no water base-layer) and a propane torch igniter was used to ignite the fuel layer immediately after n-Octane had been poured into the cavity.

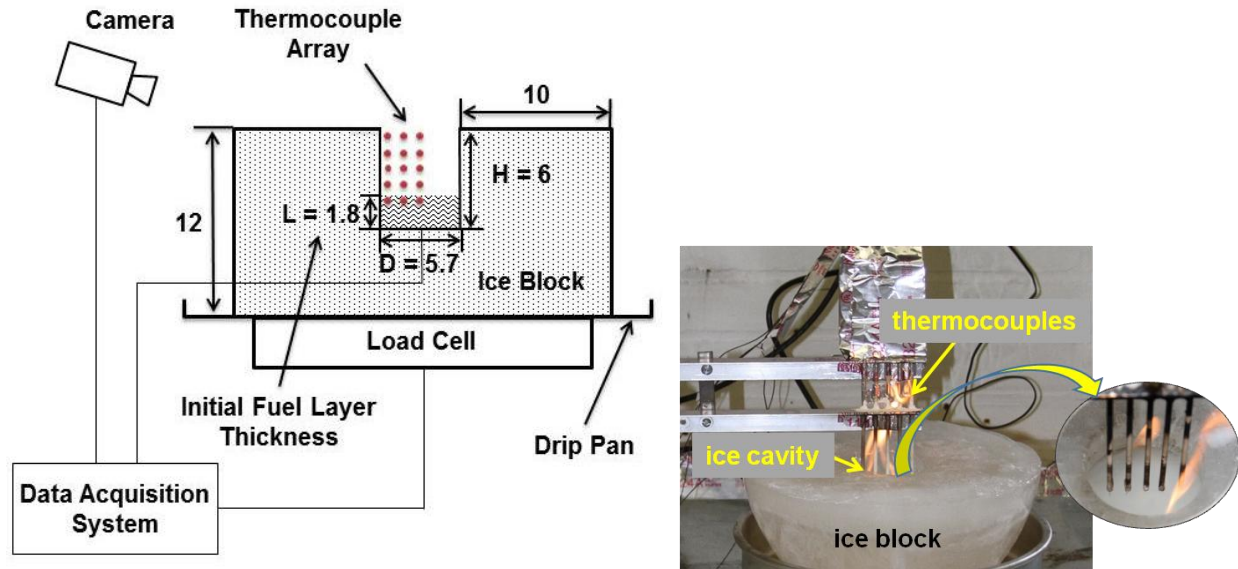


Fig. 3.1: Schematic of the experimental setup. The numbered dimensions are in cm with an uncertainty of ± 0.05 cm for D and ± 0.1 cm for H and L . Figure on the right shows a photograph of the experimental set up

Two sets of experiments were performed to collect data for analysis. In the first set, ten identical tests were conducted where the only varying parameter was the burning duration. In the first experiment, n-Octane was allowed to burn only for 1 minute and then it was extinguished by covering the ice cavity with a lead. The second experiment was extinguished after 2 minutes and so on. After each test the ice blocks were cut in half and a photograph was taken from the cross section. In addition, measurements of the ice cavity geometry were made by processing the images. These tests were intended to give an understanding of the process of geometrical changes of the ice and lateral cavity formation. In addition, the free surface of the fuel was tracked visually by the camera that was positioned on top of the ice block. Also, the interface of the fuel-water was calculated based on the fuel layer thickness at each time stamp. The fuel layer thickness was also calculated based on the diameter of cavity and the remaining mass of the fuel (Load cell data). In the second set of experiments 3 thermocouples (type K, gauge 36, and 0.13 mm diameter protected by ceramic tubes with a 1-2 mm exposed junction) were placed inside the cavity as shown with solid circles in Fig. 3.1. These tests were repeated 5 times with the thermocouple (TC) array placed at different elevations in the cavity to create a temperature map of the liquid fuel within the cavity. A more detailed description of the TC implementation is given in Section 3.2.

3.4 Results and Analysis

Measurements of the mass loss over time as well as the images taken from the cavity were used to measure and analyze the geometry change of the cavity and the thickness of the fuel layer. The results are reported in Section 3.1. along with a discussion on lateral cavity formation. The temperature profile of the fuel layer was obtained by using different arrangements of TCs inside the cavity and within the fuel layer. The results of the temperature analyses are reported in Section 3.2. A discussion on convective flow within the fuel layer and the effects of the fuel layer on melting of the ice follows in Section 3.3.

3.4.1 Cavity Change

The geometry change of the original cavity in ice during combustion of liquid fuels has been reported to be an important reason in affecting the burning rate and efficiency of a liquid fuel [17]. However, the exact changeover of the cavity into its final shape and formation of lateral

cavity was not addressed in earlier studies [17, 18]. In order to provide a detailed observation of the geometry change of the ice cavity, 10 experiments with similar initial condition were performed as explained in Section 3.2. Figure 3.2 shows the change in the cavity geometry and labels the relevant dimensions associated with the geometry changes.

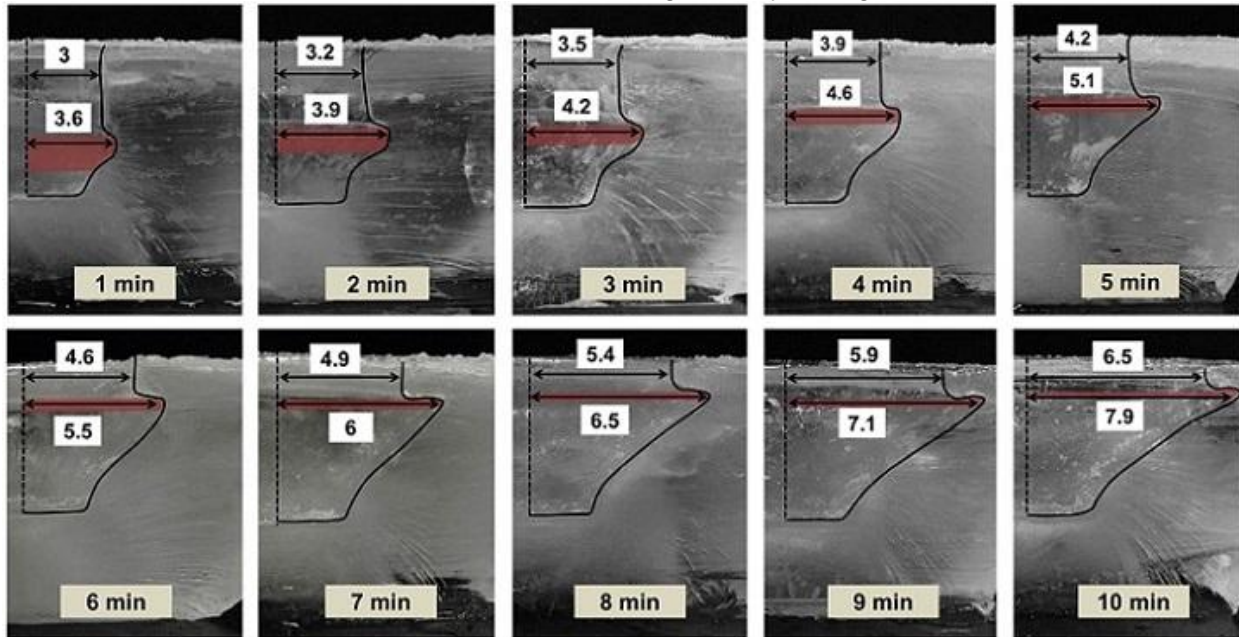


Fig. 3.2: Lateral cavity formation in sequential steps from top left in photos of ice blocks cut in half after the experiment. The vertical dashed line to the left of the pictures represents the centerline of the cavity. The dimensions are in cm with an uncertainty of ± 0.05 cm.

As shown in Fig. 3.2, at any instance during the burning of the n-Octane pool, the ice walls of the cavity were melting and the diameter of the cavity was constantly increasing. However, it was observed that the rate of melting of the ice walls were higher in areas the fuel layer was in contact with ice as compared with places where the flame was present. The melted ice created a semi-hemisphere void inside and around the circumference of the cavity. Thus, a lateral penetration of the fuel layer was observed around the perimeter of the original cavity. The final diameter of the cavity measured at the location of the fuel layer (D) was 15.8 cm whereas the diameter at the top surface of ice (D') was 13 cm. This translates into a partial penetration length (defined as $\frac{D-D'}{2}$) of roughly 1.4 cm for a 10 minute burning period. Note that the total penetration (calculated from original position of the ice wall) of the fuel layer was larger (about 5 cm) than the partial penetration length. With this estimation, the area of the fuel layer would be roughly 30 % larger than the cavity opening area. As a result, the burning rate of the fuel was reduced due to the reduction in the air entrainment to the parts of the fuel surface that were under the newly formed ice overhang.

As mentioned, during the burning of the n-Octane pool, the penetration length into the ice wall was observed to be larger wherever the liquid fuel was in contact with the ice. Contrary to the intuitive assumption that the flame's leading edge (temperature range of 1000-1300 °C) can melt the ice faster, it became evident that the liquid fuel (temperature range of 80-125 °C) is melting the ice at a much faster pace. Melting is an endothermic process and it requires a significant portion of the produced heat by combustion of the fuel to be consumed. This suggests existence of a great heat transfer coefficient in the liquid phase compared with that of the gas phase [19].

When burning the fuels in an ice cavity, a portion of the heat release is transferred to the walls, and thus converting the ice to water. Because water has a higher density than the fuel, a layer of water forms at the base of ice cavity that forces the fuel layer to elevate with respect to the bottom of the cavity [18]. For these experiments, the change in the thickness of the fuel layer (due to expansion of the cavity and evaporation of the fuel) and position of the fuel layer at each time stamps are shown in Fig. 3.3

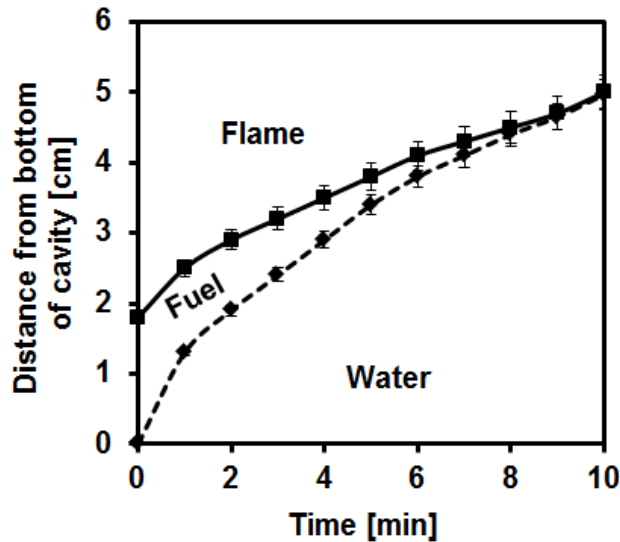


Fig. 3.3: Elevation of the fuel layer in cavity (free surface and water-fuel interface shown in solid and dashed line, respectively). The time in the figure is the time after ignition.

As illustrated in Fig. 3.3, the thickness of the fuel layer was initially at 1.8 cm (equal to ~30 g of n-Octane) and reduced to ~0 at the end of the burning. The evaporation of the liquid fuel during the burning and the increase in the diameter of the cavity were the two main reasons for the fast regression of the fuel layer thickness. It should be noted that in the final stage of the burning (the final 3 minutes), the fuel layer accumulated in a ring shape around the perimeter of the cavity. This ring shrunk and became slimmer as more fuel evaporated, but it maintained a 2 mm thickness that is required for continuous burning [20]. Due to accumulation of water at the base of the cavity, the fuel layer was elevated relative to the volume of the melt water. In the 5.7 cm diameter ice cavity, combustion of 30 g n-Octane resulted in melting of 350 g ice. This amount of meltwater made a significant increase in the fairly small cavity. However, for larger cavity diameters, the elevation of the fuel layer is expected to be insignificant.

3.4.2 Temperature history

As part of this study, the temperature distribution of the fuel layer was measured by thermocouples (TCs) at various locations as seen in Fig. 3.4. The initial fuel layer was 1.8 cm as shown in Fig. 3.4. However, through evaporation and geometry change of the ice cavity the fuel layer became as thin as about 2 mm during the final stage of the burning. As shown in Fig. 3.4, the 2 mm fuel layer remained only near the perimeter of the cavity and formed a ring shape slick. The 3 parallel TC arrays, placed 1 cm apart horizontally, consisted of ceramic tubes that ensured that the TC wires were shielded. Insulated thermocouple wires were passed through the ceramic tubes for protection against the contact with the flame and the liquid fuel. The opening of the tube (immersed in liquid) was also blocked by heat resistant cement to prevent fuel from entering the ceramic tube. Thus, the only exposed parts of the TCs were the 1-2 mm junctions. A holder was used to position the 3 TC beads at fixed elevations for each test. A total

number of 5 tests were performed with the TC arrays placed at different elevations (1 cm apart) with respect to the bottom of the cavity for tests 1 through 5. Thermocouple measurements were used to create a temperature map of the liquid fuel as it rose within the cavity. The corresponding location of TCs for each test is shown in Fig. 3.4. The uncertainty for the location of the TC arrays was ± 0.05 cm.

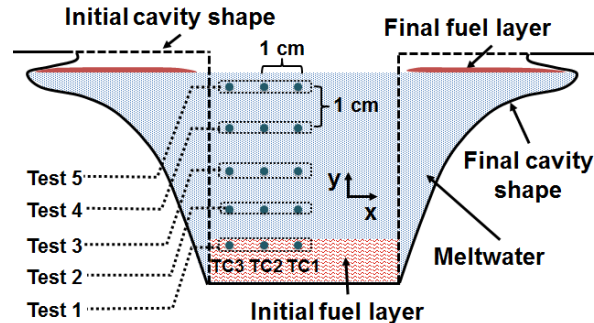
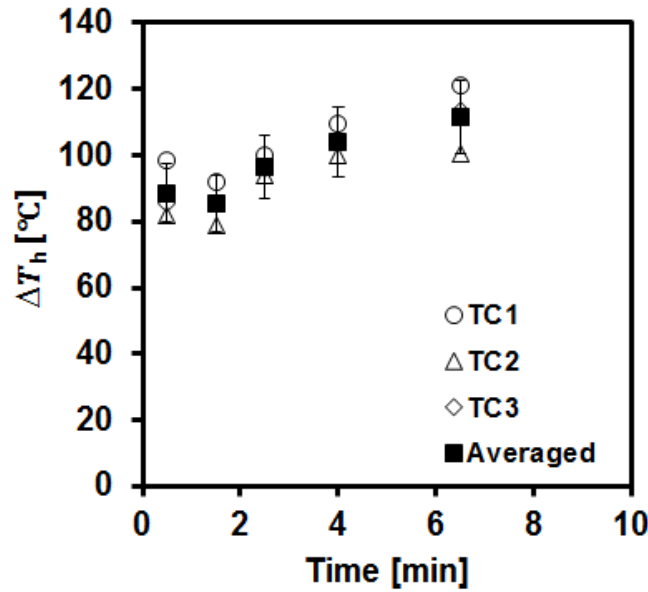


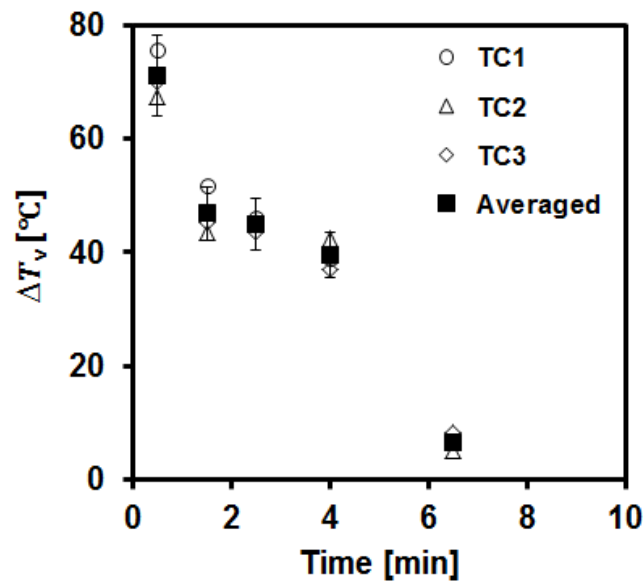
Fig. 3.4: The thermocouple array setup used to obtain the temperature history of the liquid fuel.

The three TCs positioned at different locations along the x-direction (TC1 being at the center of cavity and TC3 near the ice wall, as shown in Fig. 3.4) recorded the gas phase temperature and because the melting of the ice caused the fuel layer to rise, it eventually recorded the temperature of the n-Octane surface and that of the meltwater. The elevation of the liquid layer caused a sudden drop in the temperature recorded by these TCs. This moment was defined as the instant that the TCs immersed into the liquid fuel (a 500-700 °C drop in the temperature readings). As the boiling point of n-Octane is 125 °C, the temperature measurements in a 5 seconds period after this moment were averaged. This averaged value was assumed to be the instantaneous surface temperature of the fuel. As expected, the temperature of the fuel layer free surface measured at the center line of the cavity had the greatest value compared with the other locations measured. This is due the higher radiation input from the flame in the center [21]. Based on the findings of Hamins et al. [22], there should be a constant decrease of local heat feedback outward from the center, followed by a rise near the rims due to local heating of the fuel by the heat conducted through the rims to the body of the fuel. In a pool fire in ice, the component of the heat transfer from the flame through rims to the body of the fuel does not exist. Still, the temperature readings at the location of TC3 were higher than that of TC2. The explanation for this difference would be the existence of a high local burning rate near the perimeter of the ice cavity [23].

Using the temperature data, the temperature gradients of the fuel layer along vertical and lateral directions were obtained. In Fig. 3.5(a) the horizontal temperature gradient (ΔT_h) on the fuel surface is shown for the distances between the TCs and the ice wall. The assumption was that the temperature of the n-Octane adjacent to the ice wall was similar to that of the ice (0 °C). It is interesting to note that an isothermal condition was present at the rim and walls of the cavity. Except for the first data point (25 s after ignition), the trend for horizontal temperature gradient (ΔT_h) shows a monotonic increase. This initial non-linearity may be due to ignition effects associated with use of the propane torch. The vertical temperature gradients (ΔT_v) was defined as the temperature change from the free surface of the fuel to the fuel-water interface. Figure 3.5(b) shows the vertical temperature difference of n-Octane. As expected, the ΔT_v of the fuel layer was initially high and plummeted to small values towards the end of the burning. The decline in the fuel layer thickness increased the in-depth heat transfer, and resulted in higher temperature at the fuel-water interface.



(a)



(b)

Fig. 3.5: Temperature gradient of the fuel layer in the horizontal (a) and the vertical (b) direction.

3.4.3 Discussion on convective flows in the liquid fuel

The melting of the ice alongside the n-Octane pool was assumed to be associated with the dynamic heat and mass transfer in the fuel layer. Thus far, the convective flows in the liquid phase of pool fires in an ice cavity have not been studied. Therefore, it is important to analyze the convective flows in these situations opposed to the convective flows in the classical bounded pool fires problem. In typical pool fires, the convective motion in liquid fuels had been attributed mostly to buoyancy driven flows (occurring near the rims of the pan) and to surface tension driven flows. Normally, the flow in the liquid fuel is slowed down by the convective motion associated with the Rayleigh number and is enhanced by the convective motion

associated with the Marangoni number. However, when the liquid fuel is bounded by ice (instead of rigid walls) the mechanisms inducing the convective motions are significantly altered. In areas closer to the ice, a downward flow is expected to occur because of the lower temperature of the ice. In addition, due to the presence of the ice, a horizontal temperature gradient that produces a surface tension variation exists along the surface of the fuel. Because surface tension is a decreasing function of temperature for most of the liquids at most temperatures, a variation of the surface tension produces a flow on and near the surface of a liquid with non-uniform surface temperature. This phenomenon is known as Marangoni or thermo-capillary convection [24].

In this study, the temperature of the fuel surface at the centerline of the pool was about 125 °C and decreased to 0 °C at the side of the ice walls. Therefore, a surface tension driven flow should arise toward the ice wall outward from the center (Thermo-capillary convection) and downward in the liquid adjacent to the wall (Natural convection). The coupling between the buoyancy driven and surface tension driven flows creates a significant transport of mass and heat that provides the necessary heat to melt the ice. The relative contributions of these mechanisms are shown and discussed in the following.

Furthermore, the flow pattern was intriguing in its own right. The pattern of flow and vortices formed in the liquid fuel burning of contained pool fires are reported to include two groups of vortices [12, 13], namely a main counter-rotating vortex in the center of the pool (characterized by a larger radii and higher velocities) and a vortex close to the rims of the vessel that is formed by buoyancy. This flow pattern as described above is shown in Fig. 3.6. The exact flow pattern of the burning liquid fuel in this study remains unstudied. However, by the observations made during this study it is likely to see vortices with large radii near the free surface of the fuel. Figure 3.6 is showing the conceptual paths of the flow for the two cases. These vortices are expected to enhance in velocity during the second half of burning where the fuel layer has become thin.

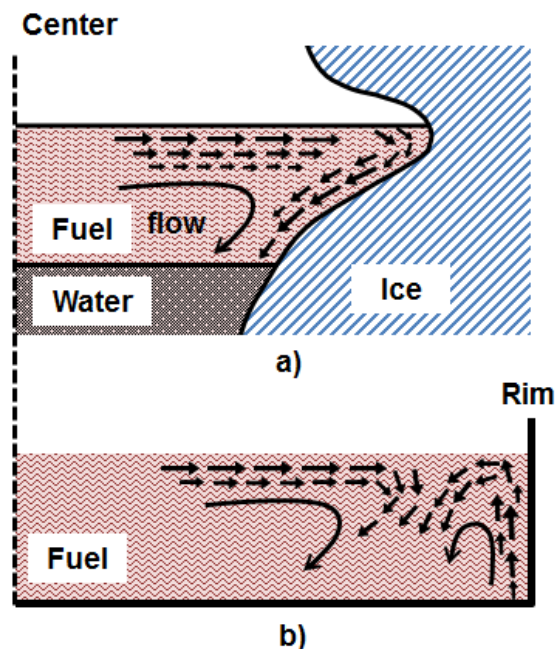


Fig. 3.6: Conceptual sketch showing the paths of the flow within the fuel layer in a) pool fires in ice cavity and b) contained pool fire.

Experimental observations were made of soot particles that were traveling on the fuel surface away from center toward the ice wall. Figure 3.7 displays the journey of one rather large particle captured on camera. This particle traveled a length of 1.5 cm in 1.28 seconds which is equal to

traversing the final diameter of the cavity (~16 cm) about 50 times in the entire burning period (10 minutes). This motion should not be mistaken with surface standing waves, which are associated with the gas phase pulsation exerting perturbation on liquid surface [22].



Fig. 3.7: Movement of a soot particle on the surface of the fuel. The particle traveled a length of 1.5 cm in 1.28 seconds towards the ice wall. Solid ice, ice cavity, and fuel surface from left to right.

To analyze the proportionality of the driving forces in the liquid fuel, the Marangoni and the Rayleigh numbers have been used as the relevant dimensionless groups for thermocapillary and natural convection, respectively [12]. The effect of evaporation on the fluid flow was assumed to be negligible so only surface tension and buoyancy have been considered as driving forces for fluid motion [10, 11, 25-27]. These dimensionless numbers can be represented as:

$$Ma = \frac{\sigma_T R \Delta T_h}{\mu \alpha} \quad (1)$$

$$Ra = \frac{\beta g L^3 \Delta T_v}{\nu \alpha} \quad (2)$$

where, $\sigma_T = \frac{\partial \sigma}{\partial T}$ is the change of surface tension per °C, R is the radius of the cavity, L is the thickness of the fuel, g is the acceleration due to gravity, and β , μ , ν , and α are thermal expansion, viscosity, kinematic viscosity and thermal diffusivity of the liquid, respectively. The physical properties of the n-Octane were acquired through use of a commercial software (Aspen HYSYS) and the surface tension variation was calculated for the temperature range of 80-125 °C. The dimensions (R and L) and also the temperature differences (ΔT_h and ΔT_v) were obtained experimentally, as explained in section 3.1 and 3.2.

After collecting all the relevant variables, Ma and Ra numbers could be calculated. Figure 3.8 shows the ratio of Ma to Ra calculated for the first 7 minutes of the burning. Because of the severe reduction of thickness of the fuel layer and ΔT_b during the course of combustion the Rayleigh number was reduced within orders of magnitude. On the contrary, radius of the cavity and ΔT_h are increasing functions of the time, hence the Marangoni number increased by a factor of 4. Consequently, the Ma/Ra ratio increased from very small values at the beginning of the experiments to unity and larger values after about 5-6 minutes. Two major convective phases could be considered for the fuel layer based on this ratio. The first phase would be the first 6 minutes of the burning, where buoyancy driven forces were dominant and the second phase occurred during the rest of the burning time where Marangoni convection became dominant.

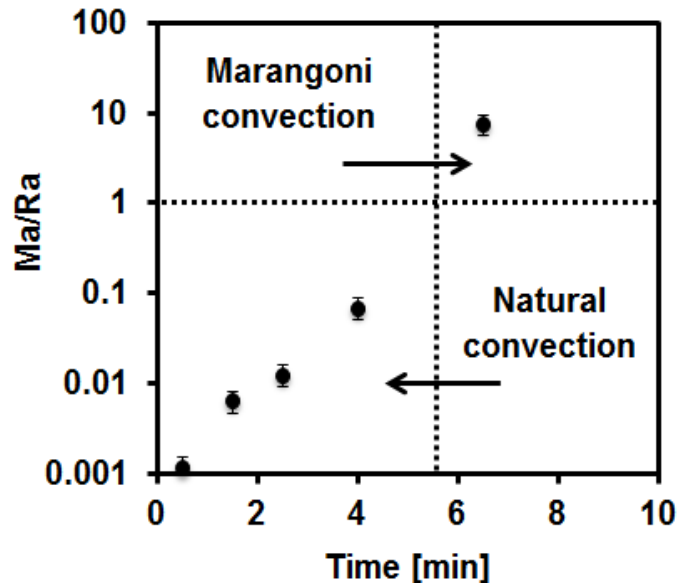


Fig. 3.8: The ratio of the Marangoni and the Rayleigh number. On the abscissa, 0 indicates the ignition time and 10 is the time for extinction of the flame.

The results of the analysis showed dominance of natural convection in the first half of the burning period when the fuel layer was of considerable thickness (1.8-0.5 cm). However, as the fuel layer thickness reduced (during the second half of the burning time), the Marangoni overcame the natural convection. The shallow pool of n-Octane at the final stage of the burning is the main reason for the diminishing natural convection. As the Marangoni number is associated with an interfacial force (acting on the surface/interface of fluids), its effect (melting of the ice and formation of the lateral cavity) is expected to be maximized with a decrease of the fuel layer thickness. The corresponding total penetration lengths of the fuel layer in ice for the first and second half of the burning were 2.1 and 2.8 cm. Also, the partial penetration lengths for the first and second half of the burning were 0.9 and 1.4 cm, respectively. It is evident that a large amount of the produced heat should be transferred to the ice through the fuel layer to melt the ice. In view of that, the heat transfer rate to the ice is obviously higher during the second phase, which means that the Marangoni convection could actually play a bigger role in melting the ice.

The two driving mechanisms (buoyancy and surface tension variation) inducing the convective flow in the liquid were analyzed to understand their contribution to the melting process. Usually, pressure, viscous, inertial and surface tension forces are of secondary importance and buoyancy alone is the dominating force for flow in liquid with a free top-surface. Hence, it is

uncommon for the Marangoni force, under normal gravitational condition and for a macroscopic scale, to overcome the buoyancy effect [28, 29]. Yet, because of the particular circumstances involved in burning of a liquid fuel adjacent to ice such occurrence was observed and reported herein.

3.5 Conclusions

A series of experiments were conducted to develop an understanding on the geometry change of an ice cavity during burning of liquid n-Octane. Based on the observations made during the experiments, it became evident that the heat transfer from the fuel layer itself is capable of melting the ice at a faster pace than the heat transfer from the flame. Thus, a void is shaped in the circumference of the ice wall, and this void is referred to lateral cavity. Also, temperature measurements of the fuel layer obtained during the burning of the n-Octane showed a temperature gradient both in the vertical and the horizontal direction. These gradients contributed to creating convective motion in the liquid fuel. The driving forces inducing the convective motion were assumed to be surface tension and buoyancy, the Marangoni and the Rayleigh numbers were calculated as the relevant dimensionless numbers for surface tension and buoyancy, respectively. The results of the analysis showed dominance of natural convection in the first half of the burning period when the fuel layer had a considerable thickness (1.8-0.5 cm). However, Marangoni convection took over as the most significant the final half of the burning. The corresponding total penetration lengths of the fuel layer in ice for the first and second half of the burning were 2.1 and 2.8 cm, respectively. A flow visualization study on this subject is required to comprehend the pattern of flow and shape of vortices in the liquid fuel.

3.6 References

- [1] H.D Ross, Ignition of and Flame Spread Over Laboratory-Scale Pools of Pure Liquid Fuels, *Prog. Energy Combust. Sci.* 20 (1994) 17-63
- [2] F. J. Miller, H. D. Ross, Further observations of flame spread over laboratory-scale alcohol pools, *Symposium (International) on Combustion*, (1992), 1703-1711.
- [3] R. Mackinven, J. Hansel, I. Glassman, Influence of laboratory parameters on flame spread across liquid fuels, *Combustion Science and Technology* 1 (1970) 293-306
- [4] J. Burgoyne, A. Roberts, P. Quinton, The spread of flame across a liquid surface. I. The induction period, *Proceedings of the Royal Society of London. Series A. Mathematical and Physical Sciences* 308 (1968) 39-53
- [5] I. Glassman, J.G Hansel, *Fire Research Abstracts and Reviews* 10 (1968) 217-234
- [6] K.E Torrance, *Comb. Sci. Tech.* 3 (1971) 133
- [7] I. Glassman, F. Dryer, Flame Spreading Across Liquid Fuels, *Fire Safety Journal* 3 (1980/81) 123 - 138
- [8] R. Murad, J. Lamendola, H. Isoda, M. Summerfield, A Study of Some Factors Influencing the Ignition of a Liquid Fuel Pool *Combustion and Flame* 1 (1970) 289-298
- [9] D.N Schiller, "Combustion above liquid fuel pools: Buoyant and surface tension-driven flow computations," Ph.D., Irvine, CA, 1991.
- [10] D.N Schiller, W.A Sirignano, Buoyant- Thermocapillary flow with nonuniform supra heating: II. Two phase behavior, *J. Thermophysics* 6 (1992) 113-120
- [11] D.N Schiller, W.A Sirignano, Buoyant-Thermocapillary Flow with Nommiform Supra-Heating: I. Liquid-Phase Behavior, *J. Thermophysics* 6 (1992) 105-112
- [12] T. Yumoto, A. Takahashi, T. Handa, Combustion Behavior of Liquid Fuel in a Small Vessel: Effect of Convective Motion in the Liquid on Burning Rate of Hexane in the Early Stage of Combustion, *Combustion and Flame* 30 (1997) 33-43
- [13] A. Vali, D. S. Nobes, L. W. Kostiuik, Transport phenomena within the liquid phase of a laboratory-scale circular methanol pool fire, *Combustion and Flame* 161 (2014) 1076-1084
- [14] F. J. Higuera, Steady thermocapillary-Buoyant flow in an unbounded liquid layer heated nonuniformly from above, *Physics of Fluids* 12 (2000) 2186-2197

- [15] A. Nakakuki, Heat Transfer Mechanisms in Liquid Pool Fires, *Fire Safety Journal* 13 (1994) 339-363
- [16] N. K. Smith and A. Diaz, In-place Burning of Crude Oil in Broken Ice- 1985 Testing at OHMSETT, in *Arctic and Marine Oilspill Program*, (1985).
- [17] H. F. Farahani, X. Shi, A. Simeoni, A. S. Rangwala, A study on burning of crude oil in ice cavities, *Proc. Combust. Inst.* 35 (2014) 2699-2706
- [18] P. W. Bellino, A.S. Rangwala, M.R. Flynn, A study of in situ burning of crude oil in an ice channel, *Proc. Combust. Inst.* 34 (2013) 2539-2546
- [19] R. Hosseini, M. Rahaeifard, Experimental investigation and theoretical modeling of ice-melting processes, *Experimental Heat Transfer* 22 (2009) 144-162
- [20] N. K. Smith, A. Diaz, In-place Burning of Prudhoe Bay Oil in Broken Ice, *Proceedings of the 1985 Oil Spill Conference*, (1985).
- [21] D. Drysdale, *An Introduction to Fire Dynamics*, 3rd ed.: John Wiley & Sons Ltd, 2011.
- [22] A. Hamins, S. Fischer, T. Kashiwagi, Heat Feedback to the Fuel Surface in Pool Fires, *Combustion Science and Technology* 97 (1994) 37-62
- [23] A. Nakakuki, Heat Transfer in Small Scale Pool Fires, *Combustion and Flame* 96 (1994) 311-324
- [24] K. Sefiane, C. A. Ward, Recent advances on thermocapillary flows and interfacial conditions during the evaporation of liquids, *Advances in colloid and interface science* 134 (2007) 201-223
- [25] N. Zhang, Surface tension-driven convection flow in evaporating liquid layers, *Surface Tension-driven Flows and Applications, Research Signpost* (2006)
- [26] B. M. Carpenter, G. Homsy, Combined buoyant-thermocapillary flow in a cavity, *Journal of Fluid Mechanics* 207 (1989) 121-132
- [27] T. Doi, J. N. Koster, Thermocapillary convection in two immiscible liquid layers with free surface, *Physics of Fluids A: Fluid Dynamics (1989-1993)* 5 (1993) 1914-1927
- [28] S. Ostrach, Low-gravity fluid flows, *Annual Review of Fluid Mechanics* 14 (1982) 313-345
- [29] J. Straub, The role of surface tension for two-phase heat and mass transfer in the absence of gravity, *Experimental Thermal and Fluid Science* 9 (1994) 253-273

Chapter 4: Influence of wicking agents on *in situ* burning of water-in-oil products from Alaska North Slope Crude oil³

4.1 Summary

The objective of this study is to examine the influence of wicking agents (peat moss, straw, jute, and commercial absorbent pads) on the burning rate and efficiency during in-situ burning (ISB) in icy condition. The experiments were performed using water-in-oil mixtures formed by Alaska North Slope (ANS) crude oil with saltwater (salinity of 35 ppt) of varying composition in the range of 20% to 40%. The agent to mixture ratios were varied at 1:5, 1:10, and 1:20 by mass, and the agent presoaking conditions were varied at 10 minutes presoaked and well-soaked. Results show that wicking agents influence the burning efficiencies in mixtures, with jute cloth showing the most promising results. The burning efficiency of 40% water-in-oil mixture was significantly improved from 50% to 79% with jute cloth as the agent, where the agent to mixture ratio was kept as 1:10 and the agent was well soaked. The second best agent is peat moss improving the burn efficiency by 29% under similar conditions.

4.2 Introduction

In situ burning of water-in-oil emulsions has been studied over the past 40 years, ever since the Exxon Valdez Oil Spill in 1989. Oil tends to emulsify with water within a few minutes of being spilled and a highly viscous and stable emulsion with water content of 80% could be formed after about one day on open water (Bech *et al.*, 1992). Oil spilled in icy water usually emulsifies much slower than in open water because of calm conditions, thick oil slick and low temperature. For example, during the “multi-year” ice break-up, water content increased to 28% over 6-days (Payne *et al.*, 1987). A much slower oil emulsification was found with low frequency wave actions, which increased to 28% water content after 34 days (Hirvi *et al.*, 1992). Oil emulsification to 40% water content was reported (Brandvik *et al.*, 2010) after 6 days in dense pack ice (70% - 90% ice cover).

Research has shown that emulsification of oil and water is difficult to ignite and burn when water content is in excess of 25% (Allen, 1991; Bech *et al.*, 1992; Buist *et al.*, 1995). This is because the maximum water content that can be removed by boiling is only about 20-30%. As the water content increases to 25% by volume, the burning rate decreases by 1/3-1/2 for stable emulsions (SL Ross, 1989). The burning rate could be further decreased to 0 (no burn) as the water content increases to 50%. The decrease in burning rate and overall efficiency has been observed in several studies (Energetex, 1980; Bech *et al.*, 1992; Garo *et al.*, 2004).

The idea of removing or separating the water from the oil to facilitate combustion has been applied to the oil emulsion burn in various ways. Emulsion-breaking chemicals (demulsifiers) have been added to emulsions before the ignition to improve the burning (Buist *et al.*, 1997). A more recent study has shown that its application to a thick emulsion slick requires additional mixing energy or heat from the igniter or combustion promoter to cause the emulsion breakdown (SL Ross, 2012). Adding combustion promoters has shown to increase the removal efficiency of oil slick by burning. It acts as a wicking agent and an insulator between the slick and the water sublayer. Several wicking agents have been tested and used since 1970

³ The contents of this chapter are published as: X. Shi, N. S. Ghion, K. T. Sundberg, J.P. Ramos, S. Stephansky, K. Ross, F. Kang, Y.Fu, V. Raghavan, and Rangwala, A. S., “Influence of Wicking Agent on In-situ Burning of Water –in-oil Products from Alaska North Slope Crude,” *Arctic Marine Oilspill Program (AMOP) technical seminar on environment contamination and response*, vol. 39, Jun 2 – 4, 2015, Halifax, Nova Scotia, Canada

(Anonymous, 1970). Among these agents, test with Fibreperl showed almost complete removal of crude oil slick by burning (Tam & Purves, 1980); test with Vermiculite also produced effective burns (Tam & Purves, 1980); some natural products such as straw and peat moss also resulted in effective burn, while the test with peat moss showed up to 95% burn efficiency; some manufactured sorbent products have been used successfully as wicking agents which include Saneringsull (Jerbo, 1973) and polypropylene sorbent sheets and pads (Buist *et al.*, 1983). However, none of these agents have been tested with water-in-oil mixtures.

In this study, an inexpensive agent (jute cloth), which has never been applied as a wicking agent, was tested with three other wicking agents that were chosen based on a literature review and consultation with the TPOC: peat moss, straw, and commercial oil only absorbent pads. Agents were tested in water-in-oil mixtures with 20% and 40% water content according to the field experiment results in pack ice (Payne *et al.*, 1987; Brandvik *et al.*, 2010). The agent to oil ratio was varied at 1:5, 1:10, 1:20 by mass with various agent presoak times (10 min and well-soaked).

4.3 Experimental Setup

Four agents used in this study are shown in Fig. 4.1. Water-in-oil mixtures were prepared using 35 ppt artificial saltwater and fresh ANS crude. An emulsification system that consisted of a gear pump to recirculate the emulsion in a 5-gallon pail placed in an ice water bath, and a drill-mounted paint mixer immersed in the oil inside the pail to mix the emulsion (Buist *et al.*, 1995). The mixtures were mixed for at least 3-6 hours and remained stable for 5-6 days with 20% water content and 2 days with 40% water content.

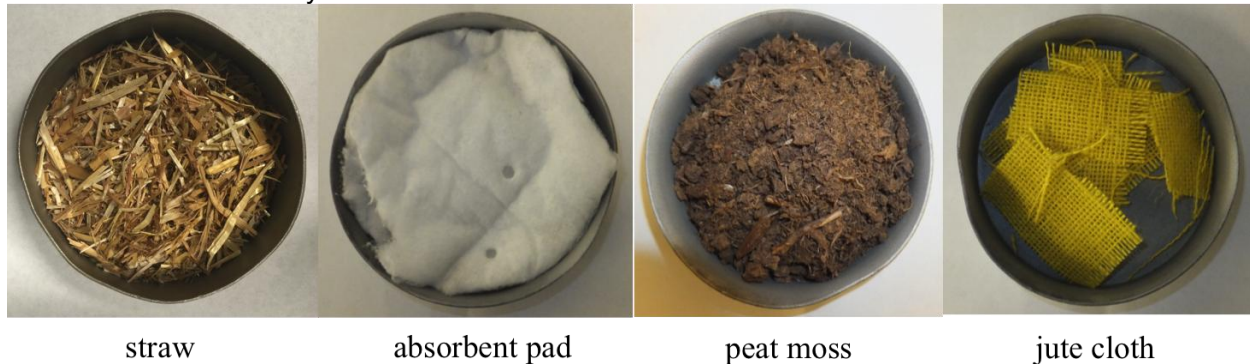


Fig. 4.1: Wicking agents used in the current study.

The influence of a wicking agent on the burning behavior was tested using the experimental setup shown in Fig. 4.2.

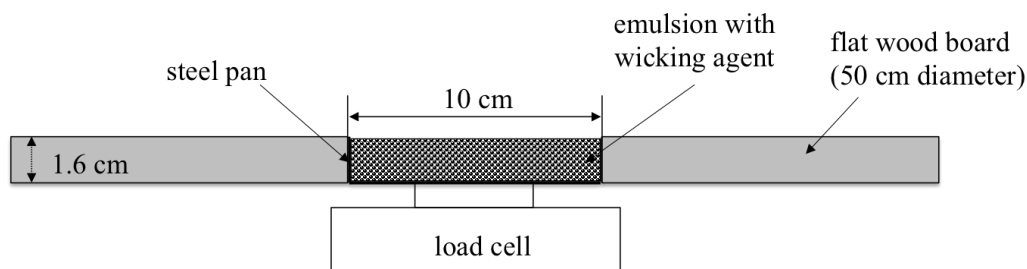


Fig. 4.2: Experimental setup of wicking agents burning test

A 10 cm circular stainless steel pan with depth of 1.6 cm and wall thickness of 1.5 mm was used as the sample holder. The pan was surrounded by a 50 cm diameter wood board that was to provide an adiabatic boundary condition and to reduce air entrainment effects caused by the rim

of the pan. Water-in-oil mixture was poured into the pan and the agent was then added evenly over the surface of the pool without pressing. The test sample was covered and allowed to settle for around 10 minutes to presoak the agent in the water-in-oil mixture. For the “well soaked” case, the agent was mixed carefully with the mixture and allowed to settle for 5 minutes so as to attain a homogeneous soaked condition. All samples were covered during this phase to prevent further weathering. The test sample was ignited using a progression of ignition sources: first ignited by a lighter, then a propane torch for 5 s (if the lighter fails), and finally by the torch for 20-30 s (if the 5 s torch ignition fails). The torch ignition (20 – 30 s) was then repeated five times. If the sample cannot be ignited successfully after 5 ignition attempts with the torch, it was considered “non ignitable.” Tests of water-in-oil mixtures without a wicking agent were performed as a “baseline” and the results were used as a reference for performance comparison.

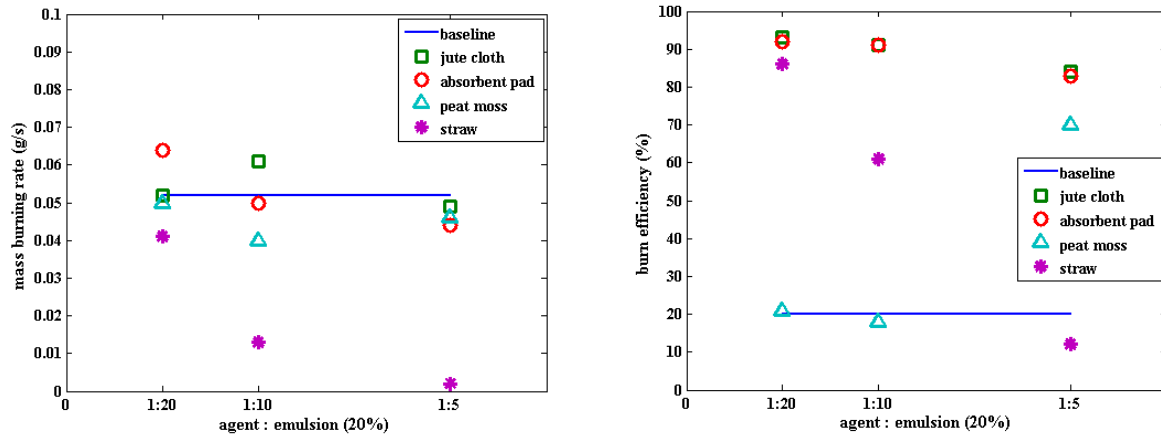
The mass burning rate was measured from the mass-loss recorded every 0.2 s by a Sartorius ED6202S-CW load cell (Capacity of 6.2 kg with sensitivity of 0.01 g and a factory uncertainty of ± 0.03 g). The burning efficiency was measured by weighing the mass of the test sample before and after the burn.

4.4 Experimental Results and Analysis

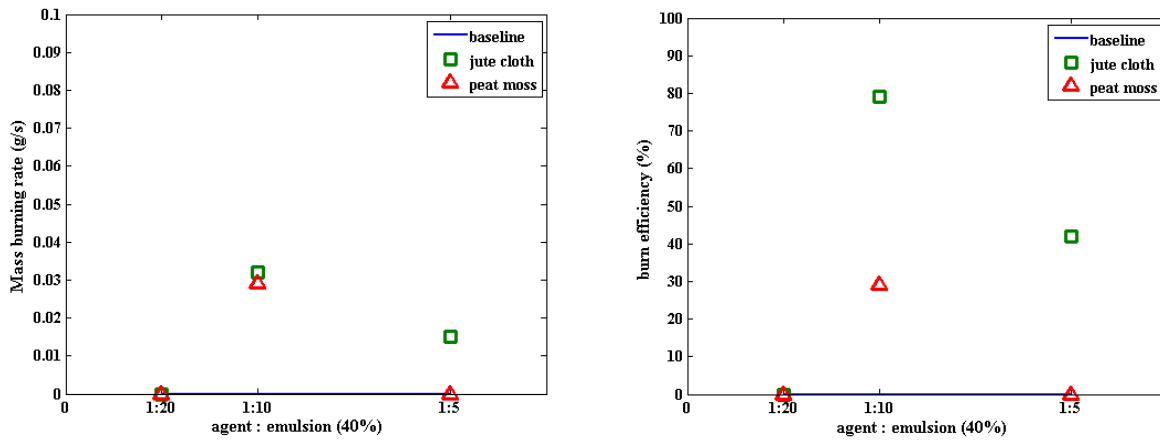
Forty-five tests using 20% and 40% water-in-oil mixtures were performed with four agents (peat moss, straw, jute and commercial absorbent pads). Two mixing conditions of wicking agent and water-in-oil mixture, comprising of a shorter 10 min presoak time and a prolonged exposure (well-soaked condition) were conducted. As mentioned earlier, the well-soaked condition was simulated by mixing the wicking agent with the water-in-oil mixture carefully without any compression.

The burning rates and efficiencies are summarized in Fig. 4.3 and Fig. 4.4. The burning efficiency is calculated as:
$$\text{Burning efficiency} = \frac{\text{mass of burned agent / water-in-oil mixture}}{\text{total mass of agent/water-in-oil mixture added}}$$
 Figure 4.3 shows the burning rate (on left) and efficiency (on right) of 20% (Fig.4.3a) and 40% (Fig. 4.3b) water-in-oil mixtures with well soaked agents. For the case with 20% water (Fig. 4.3a), jute cloth and absorbent pad showed the ability to increase the burning rate by 17% and 23% at a agent to emulsion ratio of 1:10 and 1:20, respectively. All four agents were able to increase the efficiency from 20% to a range of 70-93%. The optimum wicking agent to water-in-oil mixture ratio varied based on agent type. Results show that less agent (1:20) enhances the burn rate and efficiency most significantly for 20% water-in-oil mixture compared with the case without agent (baseline).

The influence of adding agents on 40% water-in-oil mixture is even more significant (Fig. 4.3b). The baseline burn tests of water-in-oil mixture with 40% water cannot be ignited. However, both the jute cloth and peat moss at 1:10 ratio were able to assist in a successful ignition and a sustained combustion afterwards. A higher burning efficiency was observed for jute cloth compared with peat moss. Jute cloth improved the burn rate from 0 to 0.032 g/s with a 79% efficiency, which is promising.



(a) Burning rate and efficiency of water-in-oil mixture with 20% water



(b) Burning rate and efficiency water-in-oil mixture with 40% water

Fig. 4.3: Test results of well-soaked agents

The influences of agent soak time (time for mixing agents with water-in-oil mixture) on burning rate are shown in Fig. 4.4. Soak time had limited influence on jute cloth and straw, while it did play a role on the performance of peat moss and absorbent pad. This is because of the differences in the material properties of the agents. Jute cloth could get immersed and saturated with the water-in-oil products quickly, even with the 40% emulsion, which was thick and mousse-like. On soaking, dry straw was coated/covered by the water-in-oil product. Peat moss and absorbent pad required more time to be well soaked. The longer soak time assisted in combustion of absorbent pad as shown in Fig. 4.4d, where a significant increase in mass burning rate was observed for a well-soaked condition.

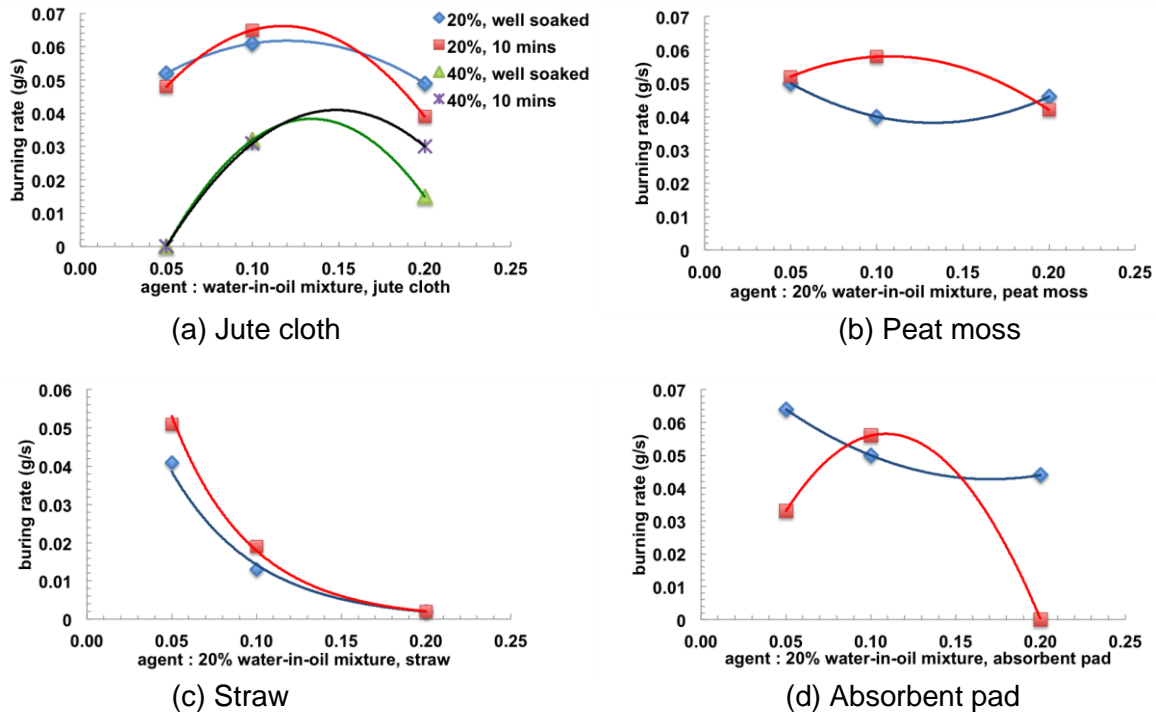


Fig. 4.4: Burn rate of agent with water-in-oil mixtures at 10 mins soaked and well-soaked

Detailed results of average steady state burning rate and burning efficiency are listed in Table 4.1. Experimental results show that jute cloth also assisted in flame propagation over the surface of the water-in-oil mixture/agent. This ability is the reason for better performance compared with other agents. The improved flame propagation was best observed at higher water content (40%).

Figure 4.5 shows flame growth during the burning of a 40% water-in-oil mixture with jute cloth at 1:10. The picture at 20 seconds after ignition shows a small weak flame in a small area. The burning rate at this stage was around 0.005 g/s. At 250 seconds after ignition, flame propagated over 2/3 of the surface. Around 500 seconds, the burning became vigorous with a burning rate increase of 0.05-0.06 g/s. This vigorous burning stage lasted for more than 400 seconds and then the burning returned back to a relatively calm stage with a burning rate of 0.035 g/s. The flame extinguished shortly. The after burn residue was found as one piece, which can be easily removed, with about 5 g clear water left on the bottom of the pan. There was no wet oil residue observed, which shows the jute cloth was capable of bringing additional heat to break the water-in-oil mixture during the burning. The experiments showed promise for application of jute cloth in the in-situ burning of water-in-oil mixtures in icy condition.

Table 4.1 Burning rate and efficiency of agent with water-in-oil mixtures

	20% water				40% water			
	10 mins pre-soaked		well-soaked		10 mins pre-soaked		well-soaked	
	Burn rate (g/s)	Efficiency	Burn rate (g/s)	Efficiency	Burn rate (g/s)	Efficiency	Burn rate (g/s)	Efficiency
Baseline	0.052	20%	0.052	20%	no ignition		no ignition	
Peat moss:mixture								
1:05	NA		0.046	70%	no ignition		NA	
1:10	0.058	88%	0.04	18%	no ignition		0.029	29%
1:20	0.052	22%	0.05	21%	no ignition		NA	
Jute cloth:mixture								
1:05	0.039	87%	0.049	84%	0.03	48.00%	0.015	42%
1:10	0.065	91%	0.061	91%	0.031	67.00%	0.032	79%
1:20	0.048	92%	0.052	93%	no ignition		no ignition	
Absorbent pad:mixture								
1:05	NA		0.044	83%	NA		NA	
1:10	0.056	40%	0.05	91%	NA		NA	
1:20	0.033	8%	0.064	92%	NA		NA	
Straw:mixture								
1:05	0.002	9.00%	0.002	12%	no ignition		NA	
1:10	0.019	49%	0.013	61%	no ignition		NA	
1:20	0.051	86%	0.041	86%	no ignition		NA	

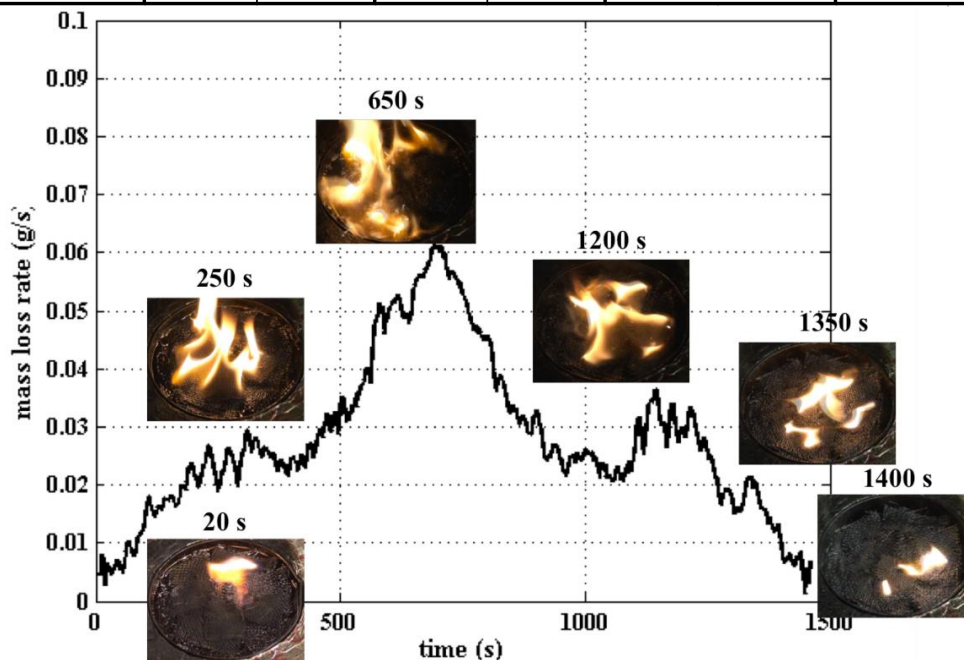


Fig. 4.5: Flame spread over water-in-oil mixture (40% water) with jute cloth (1:10)

4.4 Ignitability results and discussion

The experimental platform designed during the ignition related work (Chapter 1) was modified to test the ignitability of wicking agents at different emulsion levels at 20° C. A total of 122 tests were performed. Table 4.2 shows the ignitability of 20% and 40% emulsions under external heat flux. Two exposure time intervals of the wicking agent and oil water emulsion were investigated. A soak time of 10 mins representing a short interval between wicking agent deployment and ignition, and a well-mixed condition representing a condition where the wicking agent was exposed to the oil water emulsion for a sufficiently long interval such that it was fully soaked before ignition. Results show the critical heat flux for 20% and 40% emulsions vary between 5 and 13 kW/m². This information is critical in the design of igniters for in-situ burning.

Table 4.2. Results of ignitability under external heat flux

Heat Flux (kW/m ²)		2	5	9		5	9	13
Time of ignition (s)	20% emulsion	313	33	10	40% emulsion	NA	95	27
	10 mins soak				Well-soaked			
	Peat moss							
	1:5	>600	55	21		230	65	20
	1:10	340	34	21		443	232	22
	1:20	267	35	6		350	40	20
	Jute cloth							
	1:5	NA	NA	NA		431	25	22
	1:10	>600	56	10		222	44	24
	1:20	437	74	28		225	48	21
	Absorbent pad							
	1:5	NA	NA	NA		NA	NA	NA
	1:10	NA	NA	NA		NA	NA	NA
	1:20	>600	68	30		>600	45	21
	Straw							
	1:5	NA	NA	NA		NA	NA	NA
1:10	NA	NA	NA		NA	NA	NA	
1:20	385	30	22		187	43	20	

4.5 Conclusions

Small-scale experiments were conducted to study the influences of four types of wicking agents on the burning behavior of water-in-oil mixtures formed from ANS crude oil with water content of 20% and 40%. Among the agents, jute cloth showed the best enhancement on both the burning rate and efficiency even with the 40% emulsion. The burning rate and efficiency of 40% water content were significantly improved from 0 (unable to burn) to 0.032 g/s, and from 0 to 79% with jute cloth (1:10) while the agent was well soaked.

The study used fresh ANS crude to make 20% and 40% water-in-oil mixtures. Although both mixtures were stable during the experimental trials, future work should be aimed at “weathered” ANS crude for more stable emulsions. Further, the mechanism of ignition and burning by a

wicking agent especially with hard to ignite water-in-oil mixtures (> 20-30% water content) can be investigated by a predictive ignition, flame spread and burning rate model.

4.6 References

Allen, A.A., "Controlled Burning of Crude Oil On Water Following the Grounding of the *Exxon Valdez*," in *Proceedings of the 1991 Oil Spill Conference*, March 4-7, San Diego, CA. American Petroleum Institute, Washington, DC, U.S., pp. 213-216, 1991.

Anonymous, "Materials Applications," *Industrial Research*, 12(3): 67-68, 1970.

Bech, C., P. Sveum, and I.A. Buist, "In Situ Burning of Emulsions: the Effects of Varying Water Content and Degree of Evaporation," in *Proceedings of the Fifteenth Arctic and Marine Oilspill Program (AMOP) Technical Seminar*, Environment Canada, Ottawa, ON, Canada, pp. 547-559, 1992.

Brandvik, P.J., J.L.M. Resby, P.S. Daling, F. Leirvik, and J. Fritt-Rasmussen, *Meso-scale weathering of oil as a function of ice conditions. Oil properties, dispersability and in situ burnability of weathered oil as a function of time*. SINTEF Materials and Chemistry, Marine Environmental Technology Report no. 15563, 2010.

Buist, I.A., S.G. Potter, and D.F. Dickins, "Fate and Behaviour of Water-In-Oil Emulsions in Ice," in *Proceedings of the Sixth Arctic and Marine Oilspill Program (AMOP) Technical Seminar*, Environment Canada, Ottawa, ON, Canada, pp. 263-279, 1983.

Buist, I. A., N. Glover, B. McKenzie, and R. Ranger, "In-situ Burning of Alaska North Slope Emulsions," in *Proceedings of the 1995 International Oil Spill Conference*, American Petroleum Institute, Washington, DC, p. 139, 1995.

Buist, I., J. McCourt, and J. Morrison, "Enhancing the in situ burning of five Alaskan oils and emulsions," 1997 International Oil Spill Conference Proceedings. April 7-10. Fort Lauderdale, FL, U.S., pp. 121-129, 1997.

Energetex Engineering (Energetex), *A Study to Evaluate the Combustibility and other Physical and Chemical Properties of Aged Oils and Emulsions*, Report for Environment Canada. Environment Canada, Ottawa, ON, Canada, 1980.

Garo, J.P., J.P. Vantelon, J.M. Souil, and C. Breillat, "Burning of Weathering and Emulsified Oil Spills," *Experimental Thermal and Fluid Science*, 28 (2004): 753-761, 2004.

Hirvi, J-P., J. Koponen, and H. Vepsa, "A Case Study of the M/T Antonio Gramsci Accident in Ice-infested Waters," in *Combating Marine Oil Spills in Ice and Cold Climates, HELLCOM Seminar*, Helsinki, Finland, 1992.

Jerbo, A, "Two Types of Oil Spills in Swedish Inland Waters - Tests of new Materials, Ideas and Methods," in *Proceedings of the 1973 Conference on Prevention and Control of Oil Spills*, March 13-15, Washington, DC. American Petroleum Institute, Washington, DC, U.S., 559 p., 1973.

Payne, J.R., G. McNabb, L. Hachmeister, B. Kirsten, J. Clayton, C. Phillips, R. Redding, C. Clary, G. Smith, and G. Farmer, *Development of a Predictive Model for the Weathering of Oil in the Presence of Sea Ice*. Outer Continental Shelf Environmental Assessment Program, Final Reports of Principal Investigators. Vol 59, NOAA/OCSEAP, Washington, DC, U.S., pp. 147-461, 1987.

S.L. Ross Environmental Research Ltd. (SL Ross). *Disposal of Spilled Hibernia Crude Oils and Emulsions: In Situ Burning and the "Swirlfire" Burner*, Report to Canadian Coast Guard, Ottawa, ON, Canada, 1989.

SL Ross Environmental Research, Ltd. (SL Ross), *Emulsion Breakers to Extend the Window-Of-Opportunity for Ignition and Burning in Fire Booms: Wave Tank Tests*. Report to BP, Houston, TX, U.S., 2012.

Tam, W.K. and W.F. Purves, "Experimental Evaluation of Oil Spill Combustion Promoters," in *Proceedings of the Oceans '80 International Forum on Ocean Engineering in the 80's*. IEEE, Piscataway, NJ, U.S., pp. 415-421, 1980.

Chapter 5: Analysis of rate of flame spread after ignition of ANS crude oil at low temperatures

5.1 Summary

Ignition at the surface of ANS crude oil bounded by cold walls (bottom and side) and consequent spread of flame is experimentally investigated in this chapter using a 100 cm long and 15 cm wide metal tray. It was observed that the flame spread occurred because of preheating of the liquid ahead of the flame by convective currents driven by surface tension and density differences due to temperature gradients imposed by the leading edge of the flame. The necessity to preheat the liquid in advance of the flame caused the flame propagation to occur in three stages: an induction period where the preheating distance was at a developing stage, a quasi-steady flame spread region where the flame propagation rate reached its maximum value and the preheating distance was relatively constant and finally an end region where the preheating distance was blocked because the flame reaches the end of the tray. The three stages were also influenced by flame pulsations in some cases. The influence of boundary condition (water sub layer and adiabatic case), oil thickness (3 mm – 1.5 cm), and weathering were analyzed using image processing (visible and IR) and in-depth temperature measurements.

5.2 Introduction

Flame spread can be considered as an advancing ignition front in which the leading edge of the flame acts both as the source of heat (to raise the fuel ahead of the flame front to the fire point) and as the source of pilot ignition [1]. The problem is therefore closely linked to the piloted ignition of ANS Crude oil discussed in chapter 1. The vapour close to the surface of the liquid can be ignited by a pilot if its temperature exceeds its flash point. However, a variety of conditions can render the liquid susceptible to ignition when its bulk temperature is below its flash point including [2]: (1) partial immersion of fibrous materials which could act as wick (Chapter 4), (2) local heating by any hot surface (Flame RefluxerTM concept proposed in [3]), and (3) dispersion of the liquid which increases its specific surface such as foaming.

The rate at which flame will spread over a pool of liquid depends strongly on the temperature. If the liquid's temperature is lower than the flash point temperature, the surface ahead of the flame front must be heated to allow the flame to advance. This regime of flame spread on a liquid fuel has been defined as sub-flash flame spread [4-9]. The sub-flash flame spread has been experimentally observed to comprise of three regimes depending on the temperature difference between the initial liquid temperature and flash point. When the liquid temperature is slightly below the flashpoint, the flame is observed to spread steadily over the liquid surface and the phenomena is known as uniform flame spread. Mechanisms of uniform flame spread have been studied by Ito et al. [6]. Further decrease in the initial liquid temperature, the flame front starts to pulsate and this phenomenon is called pulsating flame spread. With a further decrease in temperature the flame front slows down significantly (~ 2 cm/s) and this regime is described as a pseudo uniform flame spread [6]. In addition to these three regimes of flame spread on a liquid fuel in the sub-flash condition, a fourth regime between uniform and pulsating where the flame propagation is caused by finger like projections has also been observed. The flame propagation is asymmetric and has not been extensively studied in literature. Only a few studies [10, 11] have reported this behaviour.

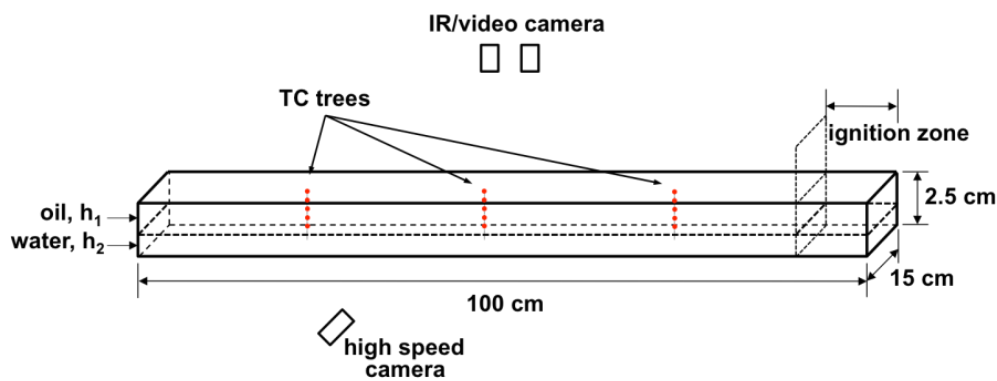
The flash point of fresh ANS Crude oil varies between 25 – 35 °C and therefore in the cold temperatures found in the arctic, it will mostly behave as a sub-flash liquid fuel. Hence it is possible to obtain either uniform or pulsating flame spread as observed by Hirano et al. [12]. In

this study, the influence of slick thickness and weathering on flame propagation was experimentally investigated. Controlling mechanisms of flame spread were established using video camera, IR cameras and in-depth temperature measurements. It was observed that the flame spread is a strong function of weathering of ANS crude oil and geometry effects.

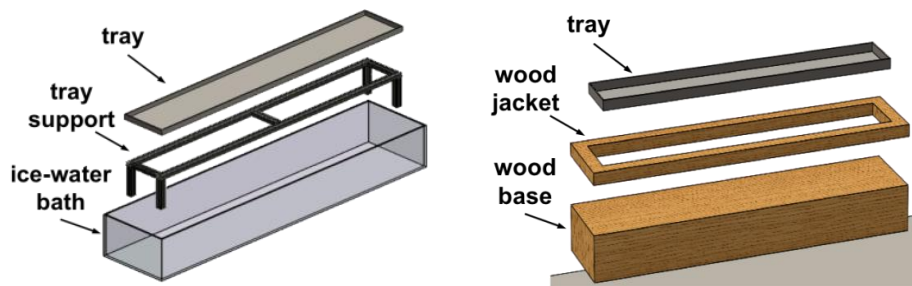
5.3 Experimental setup

Flame spread on ignition of a crude oil slick on water in an ice channel was investigated using the experimental setup shown in Fig. 5.1a. The channel was simulated by using a 100 cm long, 15 cm wide and 2.5 cm deep aluminum tray (0.8 mm wall thickness). As shown in Fig. 5.1b (left) the tray was placed in an ice-water bath to maintain the oil slick and water sub-layer at a low temperature environmental condition at around 0-5°C simulating a temperature of a melt pool or ice crack in the arctic. To simulate an adiabatic (no heat loss) boundary condition, a second experimental design comprising of a tray surrounded by a 2.5 cm thick and 5 cm wide wood jacket and then placed on a 20 cm thick wood base was used, as shown in Fig. 5.1b (right). For the adiabatic boundary condition, ANS crude oil with thicknesses of 3 mm and 5 mm were tested on a water sublayer. The oil and the water before the ignition were at around 0-5°C, but with no heat exchange with the surroundings, except the top surface.

An ignition zone segmented by a plate was used to minimize the disturbance from the torch during the ignition. The plate was removed after the flame was fully developed in the ignition zone, to allow the flame to spread. One IR camera and one visual video camera were mounted above the tray to record the leading edge of the flame. The recording was used to experimentally determine the flame spread rate defined as the spread of the flame leading edge with respect to a coordinate axis fixed to the stationary liquid container. An additional camera was used to observe the flame front from the side. Oil slick thickness was varied to study the influence on flame spread.



(a) Layout of experimental setup in the tray



(b) Simulated boundary conditions: ice-water (left) and adiabatic (right).

Fig. 5.1: Experimental setup of flame spread of an oil slick at low temperature

Three thermocouple (TC) trees made by K-type thermocouples with 75 micron (0.075 mm) diameter and with spacing of 1.4-2.8 mm were placed in the tray at 30, 50 and 70 cm from the end of the tray (shown in Fig. 5.2). Thermocouples in each tree were placed above and in the oil slick and also in the water sublayer in order to obtain the in-depth temperature distributions during the flame spread, and to track fluid movement at the leading edge of the flame.

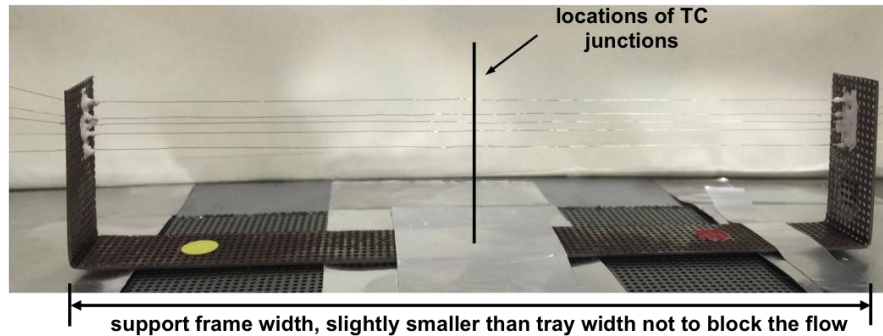


Fig. 5.2: Thermocouples (TC) for indepth temperature measurement

Several series of experiments were performed to study the effect of fuel layer thickness over water and the effect of icy and adiabatic boundary conditions on the flame spread rate of ANS crude oil. For the adiabatic boundary conditions, two experimental trials of 3 mm and 5 mm fuel layer thickness were performed. However for icy boundary condition, 5 different case of fuel thickness varied from 3 mm to 15 mm were performed. For the adiabatic boundary condition the experiments were repeated 3 times for each fuel layer thickness case. For the icy boundary conditions the experiments were repeated 5 times for each fuel layer thickness. Prior to experiments with ANS crude oil, several runs with dodecane with different fuel layer thickness were performed to get an approximate range of interest.

In order to analyze the influence of weathering on the flame spread, two additional experimental trials with ANS crude at different weathering degree were conducted. The ANS crude oil was evaporated by leaving it stagnant and open in the experimental tray for 2 days (48 hrs) and 5 days (120 hrs), separately. The oil in trays were then carefully weighed for their evaporation loss by mass, which were 18 % and 21.3 % for the 2-day and 5-day period respectively. The corresponding thicknesses of the weathered oil in the trays were ~9 mm and ~ 7 mm.

5.4 Experimental results and discussion

5.4.1 Image processing algorithm

Flame spread velocity was calculated with an image analysis scheme programmed in MATLAB as shown in Fig. 5.3. The original image, shown in Fig. 5.3a, was converted into a gray (Fig. 5.3b). The gray scale image was binarized (Fig. 5.3c) and a sobel edge detection algorithm was used to obtain the edges of the flame shown in Fig. 5.3(d). Finally, the flame tip position at each frame was calculated by averaging the pixel positions in a fixed range from the leading edge of the flame shown in Fig. 5.3(e). This range was optimised based on visual observation of a sample flame front. For consistency, the same range was used for all test cases. The numerical image analysis algorithm was then used to investigate the flame spread rate for all experimental trials.



Fig. 5.3: (a) real flame (b) binary flame (c) binary filled flame (d) flame edge (e) flame length measurement range.

In order to verify the accuracy of the algorithm, the flame tip positions determined by edge detection was superimposed on the real flame image shown in Fig. 5.4. From the RGB matrix of the flame, only the green color was depicted. The edge (calculated using the algorithm) was highlighted by the pink contour. It was observed that the image algorithm successfully captured the flame edge automatically thereby providing an accurate estimate of the flame edge as a function of time.

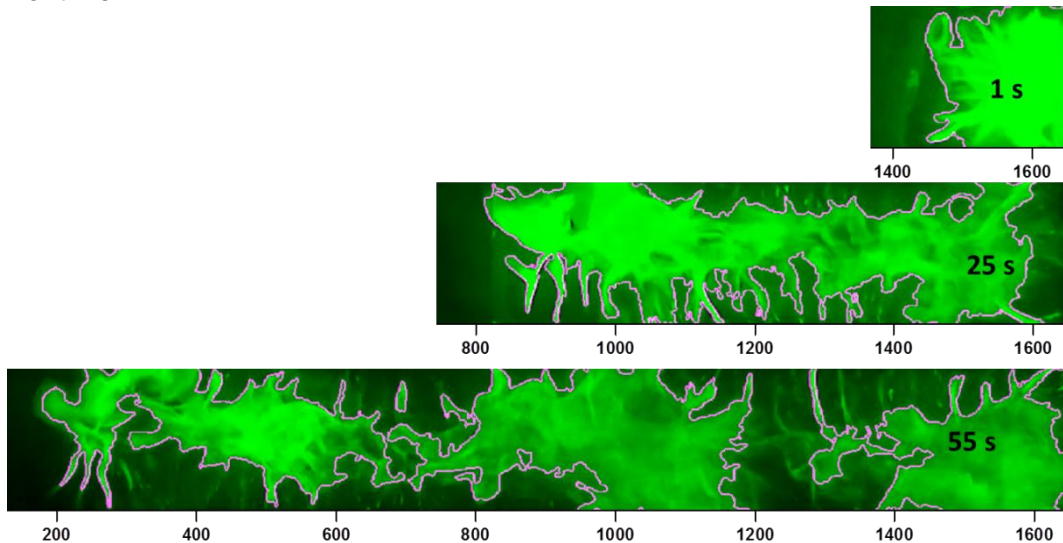


Fig. 5.4: Combined edge detection and the real flame images; shows the accuracy of the implemented image processing algorithm. Flames are in green color as only the green spectrum from RGB is used.

Figure 5.4 shows that the flame propagation was highly asymmetric and finger like projections were observed both in the forward and lateral direction. Similar projections were observed in all tests with ANS crude oil at cold temperature boundary conditions. A test performed with an ANS crude oil layer maintained at ambient conditions (20°C) with adiabatic boundary conditions, was the only test where the projections were not observed.

5.4.2 Flame tip position and spread analysis

Flame tip position was calculated using the image processing algorithm explained in section 5.4.1. Images were obtained from a Sony video camera that captures the real image of the flame as shown in Fig. 5.3(a). The Sony camera was mounted above the experimental setup to capture flame leading edge after ignition at one end of the experimental tray. Figure 5.5 shows the leading edge of the flame front as a function of time for the two boundary conditions: icy water and adiabatic. Individual flame images at different time intervals for the two boundary conditions are shown in Fig. 5.6 and 5.7. The fuel (ANS crude oil) thickness was 3 mm for both cases. In general, the adiabatic (no loss) case shows faster flame spread rate compared to the icy-water layer. As shown in Fig. 5.5 three spread regimes were observed shown by linear trend lines on the experimental data for the two cases. The slope of each linear trend was calculated to determine the flame spread rate in each regime. For the adiabatic (no loss) case, the flame

spread rate was ~ 1.9 cm/s in region I, 1.9 cm/s in region II and then decreased to ~ 0.9 cm/s in region III. In the case of 3 mm crude oil layer on icy-water, the flame spread rate was ~ 1.2 cm/s in region I, increased to 1.5 cm/s in region II and then decreased again to ~ 1.2 cm/s.

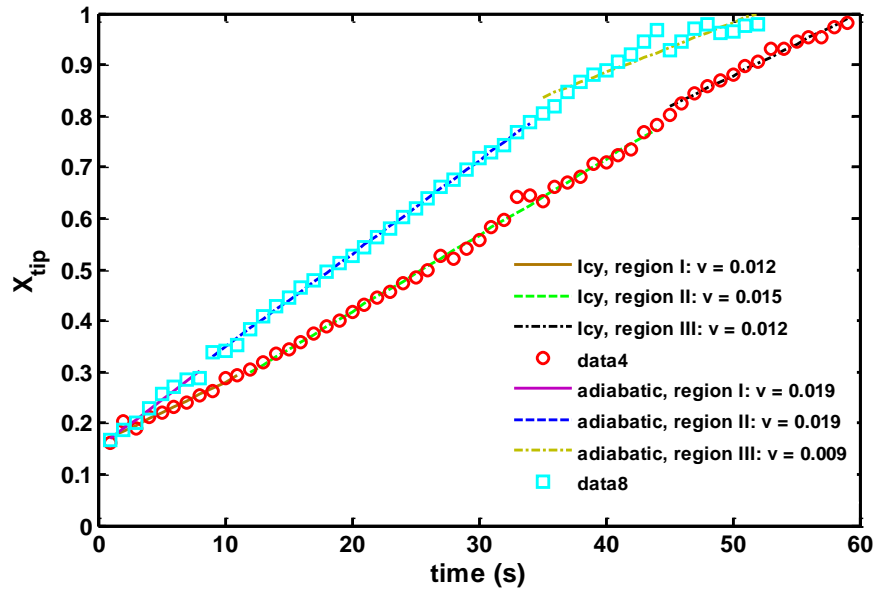


Fig. 5.5: Flame tip position versus time shown for two extreme cases of icy boundary condition with 3 mm fuel thickness and adiabatic boundary condition with 3 mm fuel thickness

In the subsequent sections, the same methodology was used to analyze the flame tip position and flame spread rate for experimental trials.

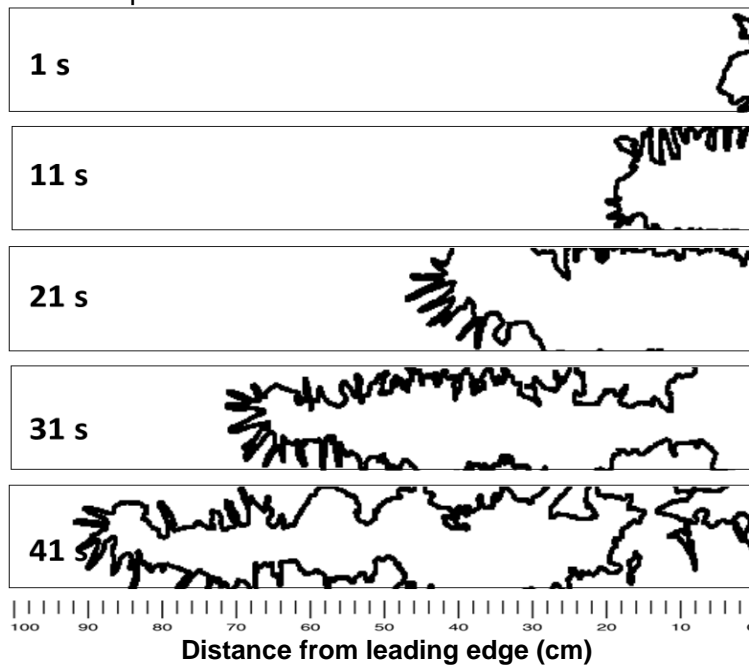


Fig. 5.6: Flame spread position versus time shown adiabatic boundary condition with 3 mm fuel thickness.

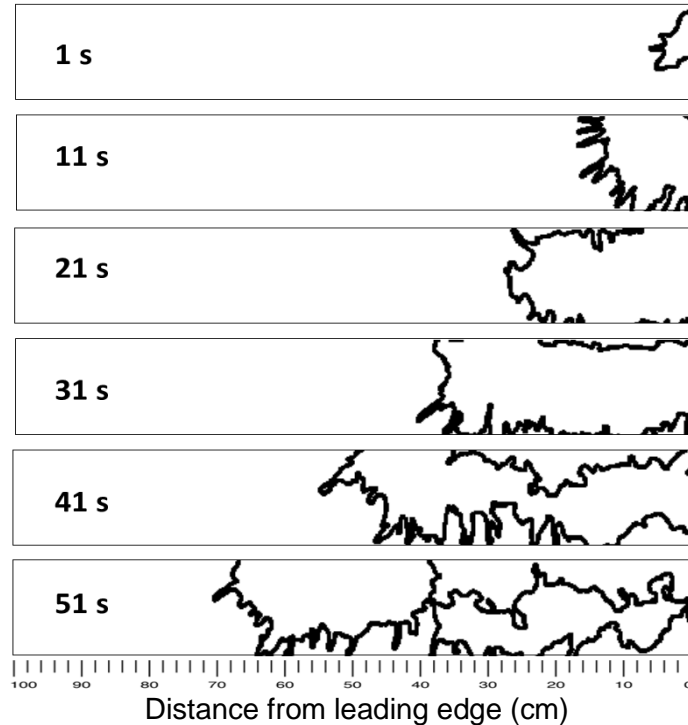


Fig. 5.7: Flame spread position versus time shown icy boundary condition with 3 mm fuel thickness.

A schematic representation of the thermocouple locations with reference to approximate locations of the 3 regions identified earlier is shown in Fig. 5.8. The flame regions were identified based on the flame spread behavior shown in Fig. 5.5. In all experiments with ANS crude oil, once the plate segmenting the ignition zone was lifted, the flame propagated slowly for the first ~24 cm (region I), then faster by about 1.5 times in region II ~50 cm, and finally slowed down in region III ~ 20 cm. Figures 5.9, 5.10 and Table 5.1 – 5.7 show the corresponding flame spread velocity for each region. Error bars are shown in Fig. 5.9 and 5.10 to show the standard deviation observed between repeated trials. As mentioned earlier, 5 repeated experimental trials were performed for the icy boundary condition and 3 repeat trials were performed for the adiabatic boundary condition.

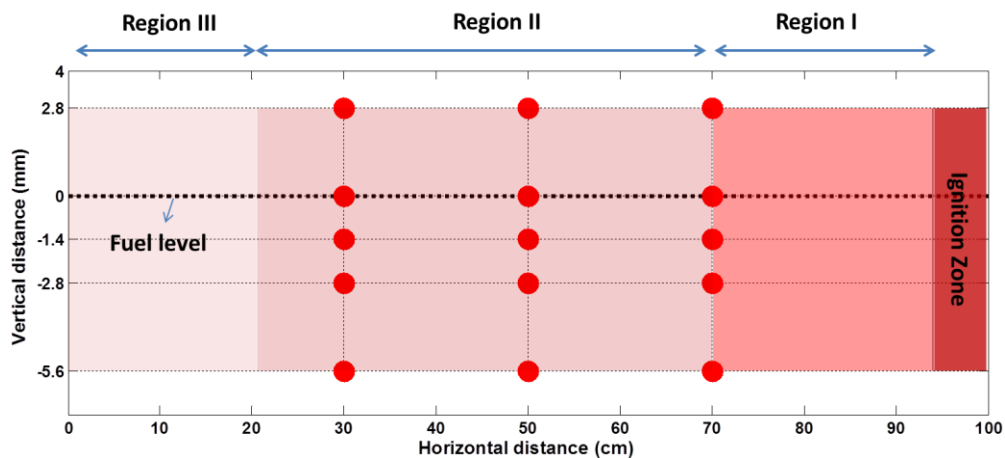


Fig. 5.8: Schematic representation of experimental set-up (side view) with thermocouples location and characteristic flame spread regions.

The results show that the fuel layer thickness does not affect the flame spread rate in region II for icy boundary conditions. However for the region I and III, the fuel layer thickness has a significant effect on flame spread rate. The thicker fuel layers yield higher flame spread rate. In general, the following factors affect the flame spread:

- 1) Difference between the initial fuel temperature and the flash point
- 2) Heat loss mechanism (i.e boundary conditions),
- 3) Surface tension of the liquid fuel,
- 4) Density, specific heat and thermal conductivity of fuel

In region I, right after ignition, the flame just started heating the liquid fuel ahead. Similar to observations by Glassman and Hansel [13], and Ross [9], the surface tension of the liquid decreases as the temperature was raised because of flame heating. This causes a net force resulted hot fuel to be expelled from beneath the flame, thereby displacing the cooler surface layer [2, 9, 12, 14, 15]. The thickness of the liquid fuel plays a significant role during early flame propagation (region I) because, with shallow pools the internal convection currents which accompany the surface tension driven flow are restricted. In addition, heat losses to the water sub-layer increase with decreasing thickness of the oil layer.

In region II, the surface tension driven convective flow was fully developed and the flame therefore propagates at the maximum possible velocity, given the composition of the fuel. The thickness seems to have little effect in the propagation velocity for region II. This region also occupied ~50% of the spread regime. In region III, heat loss once again increased because the surface tension driven convective flow was restricted by the end of the tray. This is the main reason why the flame slows down here. In-depth temperature data also shows that the difference between the fuel temperature and the flash point of the fuel was higher in region I and II compared with region III. The higher temperature difference between flash point and the fuel surface temperature can lead to flame pulsation in the direction of the flame spread [7, 9, 16]. This pulsation is a discrete flame spread mechanism and it decrease the flame spread. This may be one more reason for flame spread rate to be lower in these regions (I and III) compared to region II.

The difference between the adiabatic and icy boundary condition is significant in 3 mm ANS crude oil thickness. Especially, the difference arises in region II. The likely reason for this is mainly because of the heat loss to the water sub layer which is avoided in the adiabatic boundary condition. Therefore the flame spread rate is significantly higher in the adiabatic boundary condition than that of icy boundary condition. As the thickness of the ANS crude oil increased to 5 mm, the flame spread rate with the two cases is comparable. This is again because of the in depth heat transfer to the water sublayer. In the case of 3 mm fuel thickness, the heat loss in-depth from the fuel surface into the water layer was higher than that of 5 mm. The thermal conductivity of ANS crude oil was ~ 0.124 W/m K, on the other hand thermal conductivity of the water was ~0.6 W/m K. Therefore the heat loss in the water must be higher in the case of thinner fuel. Another important mechanism can be due to the velocity boundary layer of the liquid. If the boundary layer thickness was close to the fuel layer thickness, then the possibility of the convection heat transfer by the water layer can be significant. Therefore, the thinner fuel layer yields higher heat loss due to the convection of the water under the liquid fuel layer.

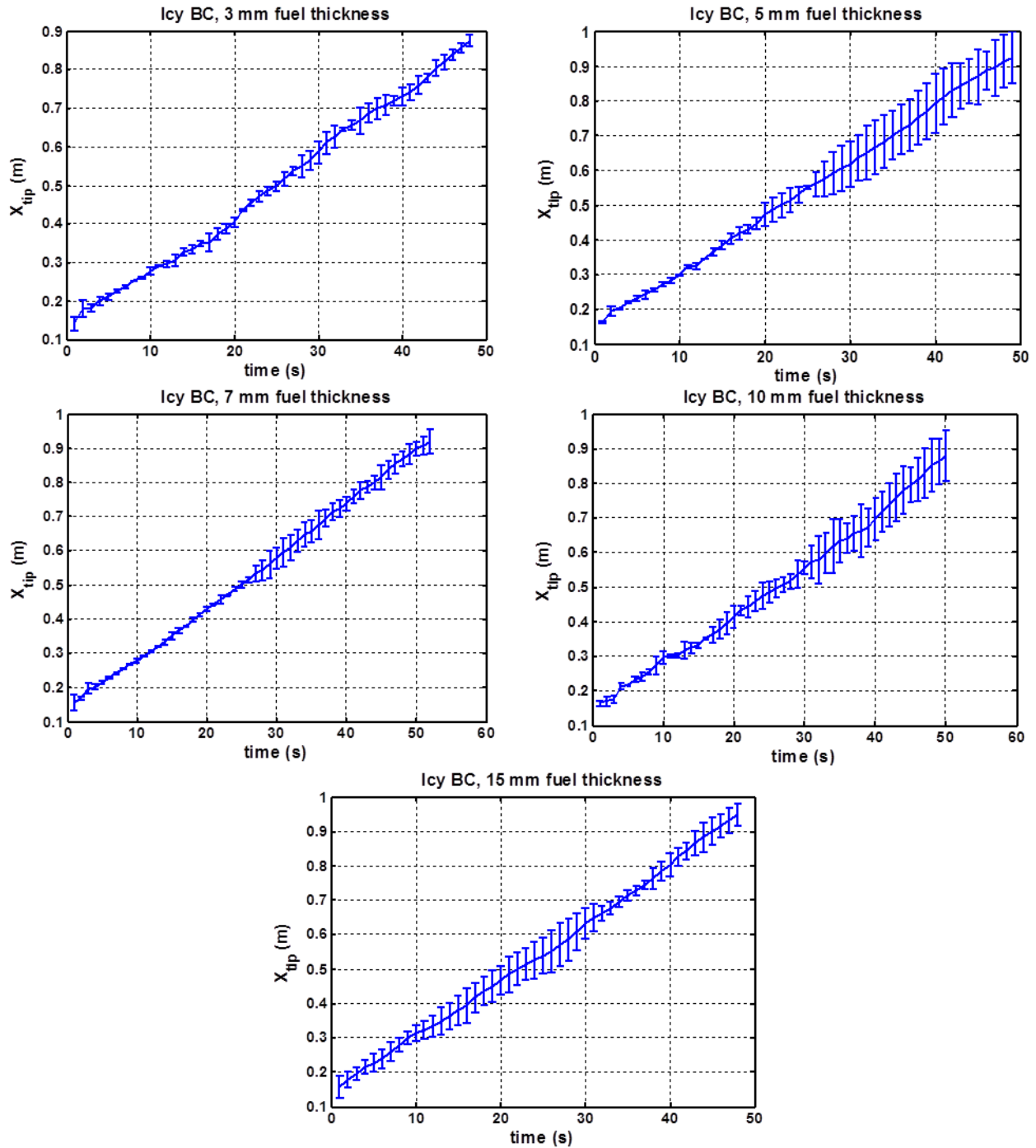


Fig. 5.9: Icy condition testing flame tip position of ANS Crude Oil with a 3 mm, 5 mm, 7mm, 10 mm and 15 mm oil thickness. (Each test is repeated 5 times).

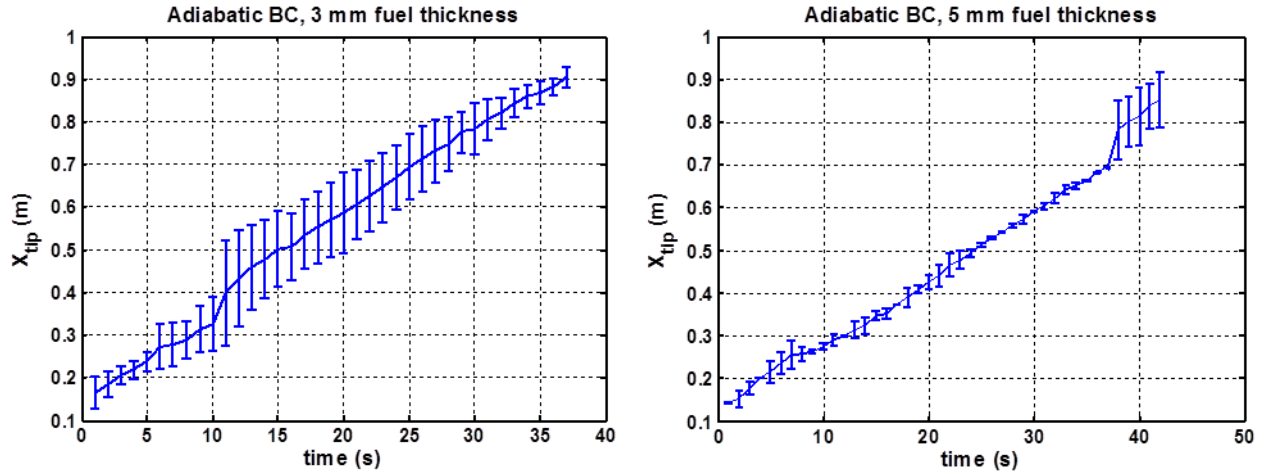


Fig. 5.10: Adiabatic condition testing flame spread of ANS Crude Oil with a 3 mm and 5 mm oil thickness. (Each test is repeated 3 times).

Table 5.1: Flame spread rate calculation for 3 mm fuel ANS crude oil thickness with icy boundary condition

3 mm icy condition

# of test	Region I	Region II	Region III
	100 90 80 70 60 50 40 30 20 10 0	100 90 80 70 60 50 40 30 20 10 0	100 90 80 70 60 50 40 30 20 10 0
1	0.012	0.015	0.012
2	0.010	0.015	0.012
3	0.014	0.024	0.012
4	0.012	0.017	0.012
5	0.013	0.014	0.011
average velocity (m/s)	0.012	0.017	0.012

Table 5.2: Flame spread rate calculation for 5 mm fuel ANS crude oil thickness with icy boundary condition

5 mm icy condition

# of test	Region I	Region II	Region III
	100 90 80 70 60 50 40 30 20 10 0	100 90 80 70 60 50 40 30 20 10 0	100 90 80 70 60 50 40 30 20 10 0
1	0.015	0.014	0.013
2	0.013	0.018	0.013
3	0.012	0.017	0.014
4	0.012	0.015	0.014
5	0.014	0.017	0.012
average velocity (m/s)	0.013	0.016	0.013

Table 5.3: Flame spread rate calculation for 7 mm fuel ANS crude oil thickness with icy boundary condition
7 mm icy condition

# of test	7 mm icy condition		
	Region I	Region II	Region III
1	0.015	0.014	0.013
2	0.014	0.016	0.014
3	0.014	0.016	0.013
4	0.012	0.017	0.015
5	0.013	0.015	0.016
average velocity (m/s)	0.014	0.016	0.014

Table 5.4: Flame spread rate calculation for 10 mm fuel ANS crude oil thickness with icy boundary condition
10 mm icy condition

# of test	10 mm icy condition		
	Region I	Region II	Region III
1	0.014	0.013	0.013
2	0.012	0.014	0.022
3	0.011	0.013	0.016
4	0.016	0.017	0.021
5	0.012	0.017	0.016
average velocity (m/s)	0.013	0.015	0.017

Table 5.5: Flame spread rate calculation for 15 mm fuel ANS crude oil thickness with icy boundary condition
15 mm icy condition

# of test	15 mm icy condition		
	Region I	Region II	Region III
1	0.016	0.016	0.019
2	0.020	0.017	0.018
3	0.016	0.017	0.018
4	0.014	0.015	0.014
5	0.017	0.017	0.015
average velocity (m/s)	0.017	0.016	0.017

Table 5.6: Flame spread rate calculation for 3 mm fuel ANS crude oil thickness with adiabatic boundary condition

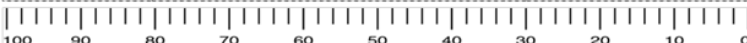

3 mm adiabatic condition			
# of test	Region I	Region II	Region III
			
1	0.014	0.022	0.015
2	0.010	0.030	0.012
3	0.019	0.018	0.010
average velocity (m/s)	0.014	0.023	0.012

Table 5.7: Flame spread rate calculation for 5 mm fuel ANS crude oil thickness with adiabatic boundary condition

5 mm adiabatic condition			
# of test	Region I	Region II	Region III
			
1	0.014	0.017	0.011
2	0.018	0.015	0.015
3	0.011	0.018	0.010
average velocity (m/s)	0.015	0.017	0.012

5.4.3 Influence of weathering on flame spread rate of ANS crude oil

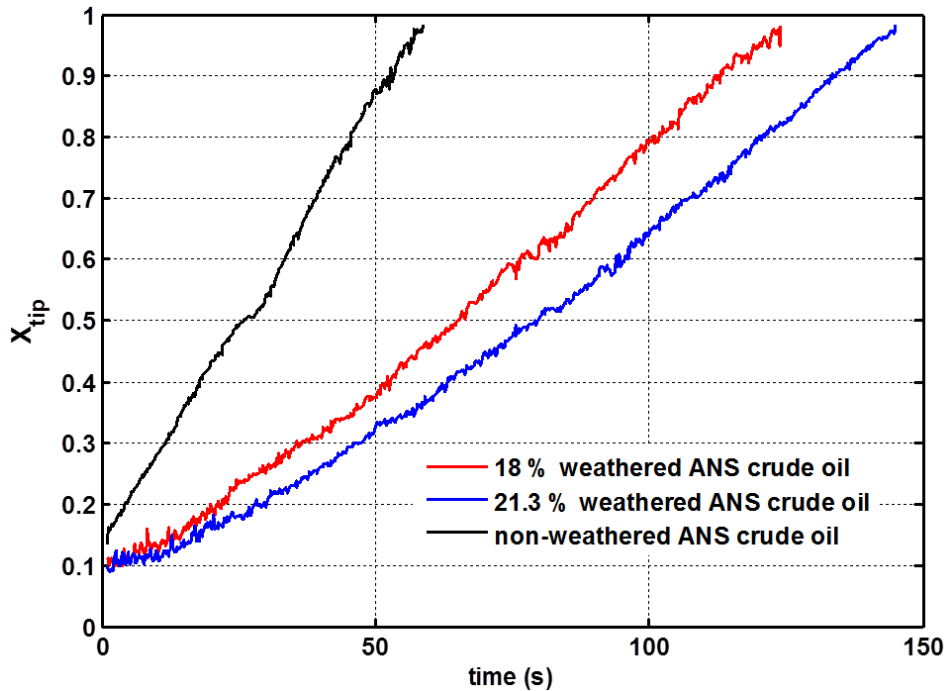


Fig. 5.11: Icy condition testing flame tip position of non-weathered, 18% weathered and 21.3 weathered ANS crude oil

Table 5.8: Flame spread rate calculation for weathered ANS crude oil thickness with icy boundary condition

Weathered ANS crude oil, icy condition			
# of test	Region I	Region II	Region III
	100 90 80 70 60 50 40 30	20 10 0	
18 % weathered	0.006	0.008	0.008
21.3 % weathered	0.004	0.007	0.008
average velocity (m/s)	0.005	0.007	0.008

The flame tip position of the weathered cases and the 7 mm icy boundary condition case are shown in Fig. 5.11. In the case of non-weathered case, the flame spread rate was higher than the weathered case. The 5 days weathered case (21.3%) shows the slowest spread rate (~0.7 cm/s). This can be explained by the flash point of the fuel. The flash point has a significant effect on the flame spread rate. The heavier components have higher flash points, and hence the flame spread regime has a pulsating character. The pulsating flame does not have a continuous connection with the fuel surface, and slows down the flame propagation in the pulsating direction. Here, again it is possible to observe three different regions of the flame tip position similar to the earlier cases. The flame spread was slow initially after the ignition and the pulsating frequency was higher as shown in Fig. 5.11. However, in region II, the flame spread rate increased even though the pulsations remained. In region III, the flame spread slowed down and the magnitude of the oscillations increased. This is clearly shown in the case of 18 % of weathered case.

5.4.4 Measurement of heated region ahead of the flame front using IR imaging

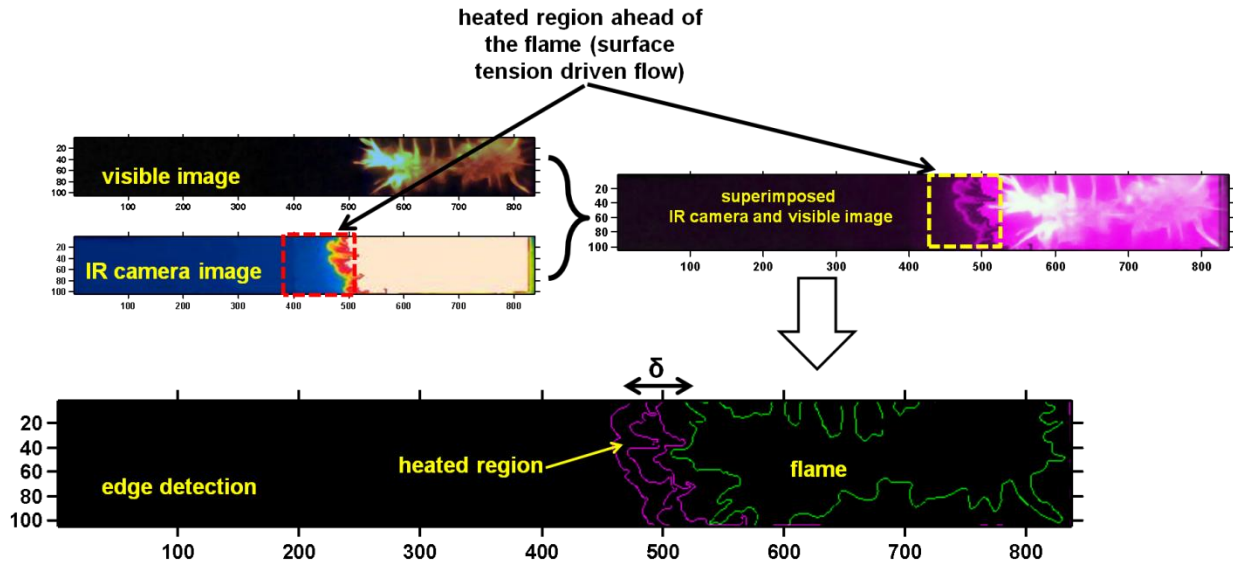


Fig. 5.12: Visible and IR image superimposed to determine δ defined as the heated region ahead of the flame.

As discussed previously, an important mechanism of the flame spread rate on a liquid fuel layer is the surface tension driven convective flow that heats the fuel ahead of the flame. This hot fuel layer racing ahead of the flame was clearly observed from the IR camera which was used in conjunction with the Sony video camera and mounted on top of the experimental tray looking down. Note that the IR camera used in the study was only capable of showing a maximum temperature of 150 °C. The temperature beyond 150 °C in IR camera was shown in white color. The color map is from white – red to dark blue. The lower temperature was detected by blue color. The IR image and the Sony camera images were merged together and the edge detection algorithm (discussed in 5.4.1) was used to determine the flame position.

Figure 5.12 shows an example visible and IR image and the corresponding image processing applied to obtain δ , defined as the distance ahead of the flame that was heated by surface tension driven flow. Figure 5.13 shows the flame tip position obtained from IR and Sony camera for 18% and 21.3 % weathered tests with 7mm ANS crude oil fuel layer. The length of the heated region (δ) decreased with increased weathering as shown in Fig. 5.13. This is mainly because the viscosity of the ANS crude oil was higher for the 21.3% weathered sample compared to the 18% weathered sample. The increase in viscosity causes a reduction in the surface tension driven convective flow preheating the fuel ahead of the flame. This ultimately leads to a lower flame propagation rate also observed in Fig. 5.13.

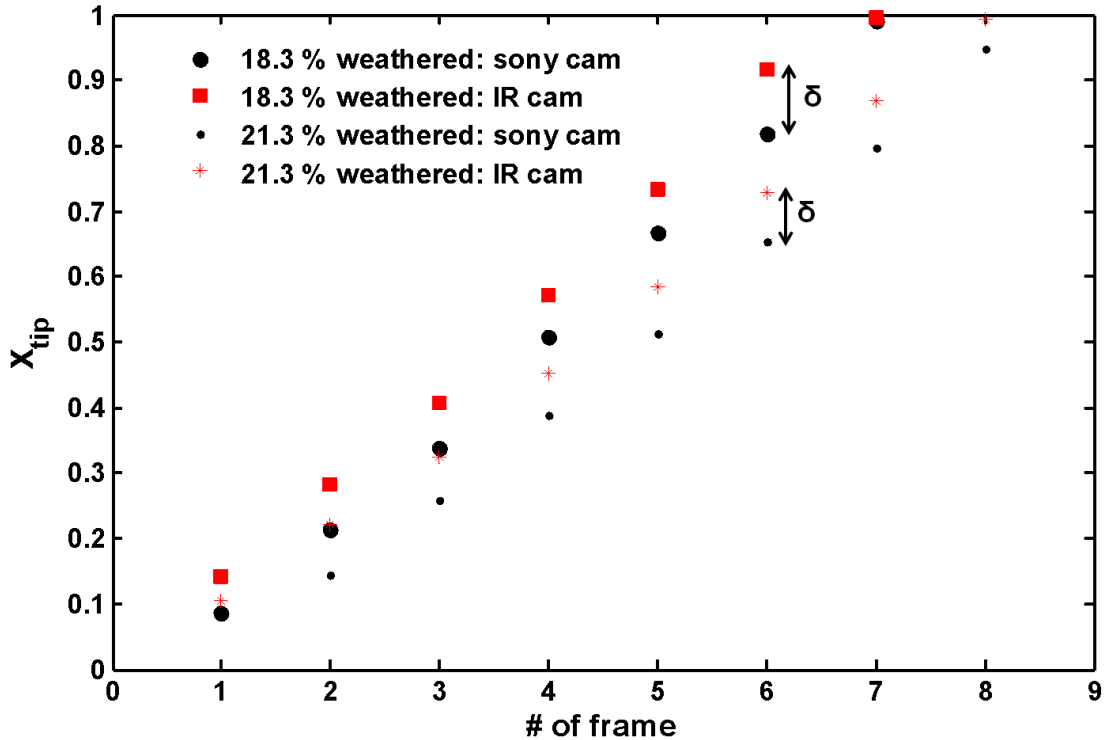


Fig. 5.13: Flame position by the visible camera and the fuel hot zone front by the IR camera for 7mm icy boundary condition of ANS crude oil.

It should be noted that the difference between flame tip positions calculated by IR camera and visible (Sony) camera was low initially and then increases in region II and then again decreases in region III towards to end of the tray. This proves the early hypothesis of surface tension driven flows playing a significant role in flame behavior observed in regions I, II and III.

5.5.5 In-depth temperature profiles

Figures 5.14 and 5.15 show the flame tip position versus time for the 3 mm and 15 mm ANS crude oil with icy boundary conditions. The corresponding temperature profiles at times when the flame leading edge arrives at the TC tree location is also shown. The thermocouple data was mapped into a 2D mesh grid based on the locations shown in Fig. 5.8. Then the contours of the temperature were plotted once the flame reaches a specific thermocouple array.

When the leading edge of the flame reached the first thermocouple location in both tests, temperature contours obtained from thermocouples measurements show that the liquid fuel layer temperature of the 3 mm test case was higher than that of the 15 mm test. On the other hand, the gas phase temperature of 15 mm test was higher than the gas temperature of 3 mm test. This trend was followed by the other thermocouple locations as well. Another important difference observed from thermocouple measurement was the fuel hot zone that was the hot region ahead of flame tip position. It is clearly shown that the fuel hot zone for the 3 mm at second thermocouple location was about 5 cm on the fuel surface. However, for the 15 mm case, fuel hot zone length was about 1 cm.

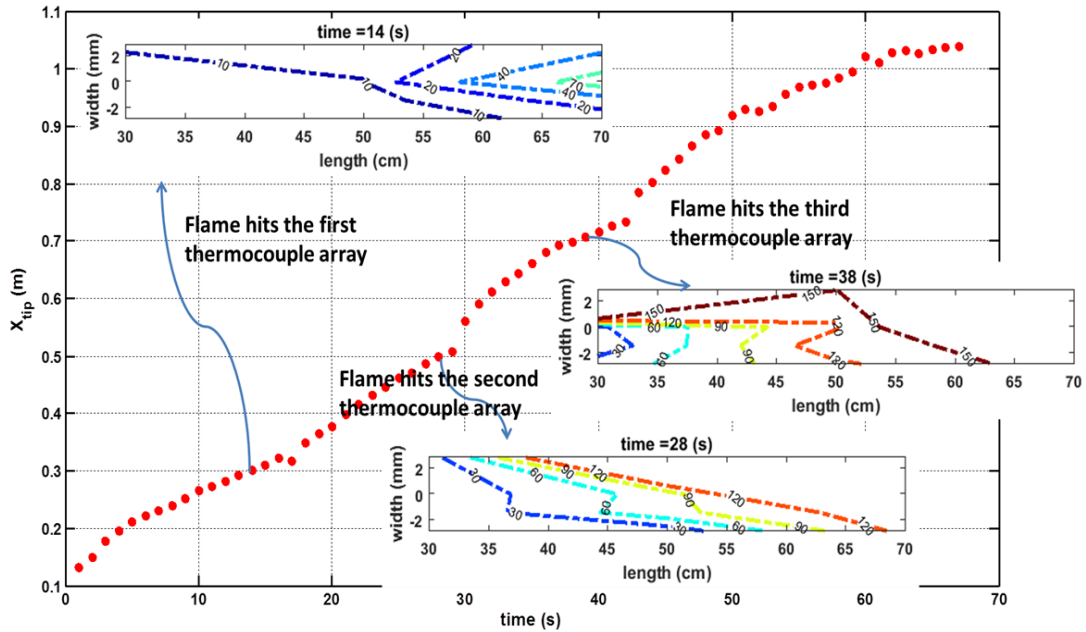


Fig. 5.14: 3 mm ANS crude oil icy boundary condition: temperature contours obtained from thermocouple data.

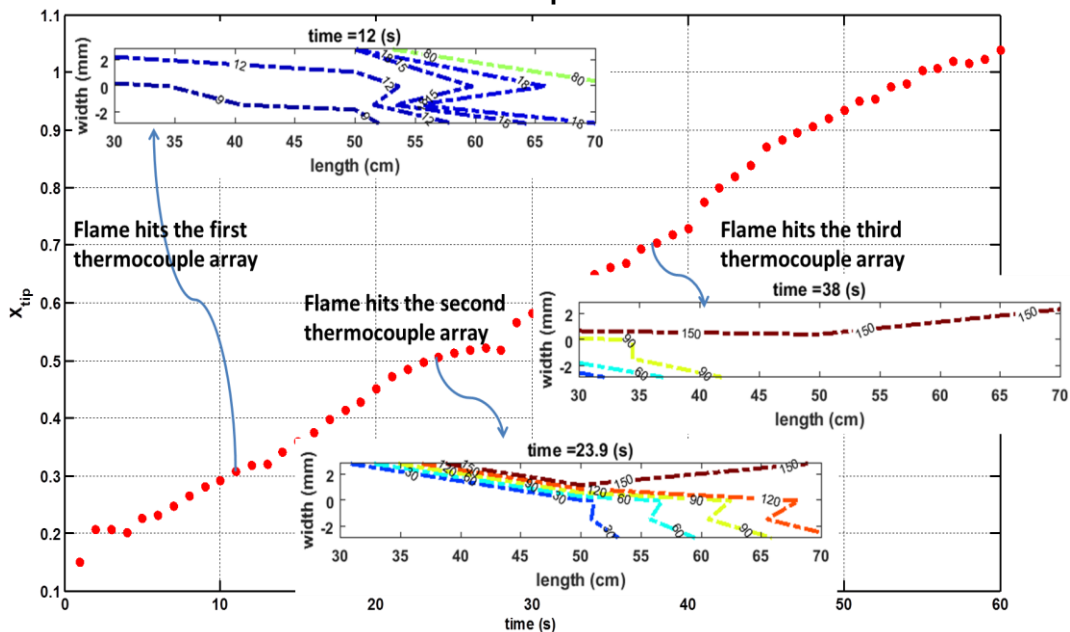


Fig. 5.15: 15 mm ANS crude oil icy boundary condition: temperature contours obtained from thermocouple data.

As discussed earlier, the heated fuel zone which is formed due to surface tension driven flow ahead of the flame leading edge is the primary controlling parameter for the flame propagation speed. The *rate* of formation of this zone is determined by the velocity of the hot liquid layer that races ahead of the flame leading edge and preheats the liquid ahead of the flame. The thickness of this layer, which is mostly a function of the liquid fuel properties such as viscosity, thermal conductivity, specific heat, and density can also be used to determine the minimum fuel thickness to sustain a continuous flame spread.

5.6 References

1. Drysdale, D., *An introduction to fire dynamics*. 1998: John Wiley & Sons, New York.
2. Burgoyne, J. and Roberts, A. *The spread of flame across a liquid surface. li. Steady-state conditions*. in *Proceedings of the Royal Society of London A: Mathematical, Physical and Engineering Sciences*. 1968. The Royal Society.
3. Rangwala, A.S., Shi, X., Arsava, K.S., and Mahnken, G., *Methods and systems for clean-up of hazardous spills*, 2016, US Patent 20,160,123,582.
4. Glassman, I. and Dryer, F.L., *Flame spreading across liquid fuels*. *Fire Safety Journal*, 1981. **3**(3): p. 123-138.
5. Hirano, T., Suzuki, T., Sato, J.I., and Ohtani, H. *Flame spread over crude oil sludge*. *Proc. Combust. Insti*, vol. 20, 1985. Elsevier.
6. Ito, A., Masuda, D., and Saito, K., *A study of flame spread over alcohols using holographic interferometry*. *Combustion and Flame*, 1991. **83**(3): p. 375-389.
7. Ito, A., Saito, K., and Cremers, C., *Pulsating flame spread over liquids*. *Fire Safety Science*, 1994. **4**: p. 445-456.
8. Schiller, D., Ross, H., and Sirignano, W., *Computational analysis of flame spread across alcohol pools*. *Combustion Science and Technology*, 1996. **118**(4-6): p. 203-255.
9. Ross, H.D., *Ignition of and flame spread over laboratory-scale pools of pure liquid fuels*. *Progress in energy and combustion science*, 1994. **20**(1): p. 17-63.
10. Helmstetter, A.J., *An experimental study of subsurface connective flows preceding a flame front spreading over a liquid fuel (msc thesis)*. 1974: Princeton University.
11. Ross, H.D. and Sotos, R.G. *An investigation of flame spread over shallow liquid pools in microgravity and nonair environments*. in *Proc. Combust. Instit*. 1991. Elsevier.
12. Hirano, T., Suzuki, T., Sato, J., and Ohtani, H. *Flame spread over crude oil sludge*. 1985. Elsevier.
13. Glassman, I. and Hansel, J.G., *Some thoughts and experiments on liquid fuel flame spreading, steady burning and ignitability in quiescent atmospheres*, 1968, DTIC Document.
14. Mackinven, R., Hansel, J., and Glassman, I., *Influence of laboratory parameters on flame spread across liquid fuels*. *Combustion Science and Technology*, 1970. **1**(4): p. 293-306.
15. Akita, K. *Some problems of flame spread along a liquid surface*. in *Symposium (International) on Combustion*. 1973. Elsevier.
16. Ross, H.D. and Miller, F.J. *Flame spread across liquid pools with very low-speed opposed or concurrent airflow*. in *Symposium (International) on Combustion*. 1998. Elsevier.

Chapter 6⁴: Large scale burning behavior of ANS crude oil in ice cavities

6.1 Summary

Five large scale tests were conducted during the course of the study comprising of two indoor tests performed with fresh water ice with a thin (~5 cm) water sublayer at the WPI Fire Laboratory (Test 2-3); and three outdoor tests within an artificial ice pond (Test 4-6) with a thick (~70-80 cm) water sublayer at the US Army Cold Regions Research and Engineering Laboratory (CRREL) located in Hanover, NH. Table 6.1 shows the large scale experimental test matrix. The large scale test performed in 2013 [1] [2] is also included for comparison. The geometry change (lateral cavity) observed and investigated at the small scale (chapter 3) is also observed in the large scale tests. In fact, salt water ice melts at a faster rate compared with fresh water ice.

The major finding from the tests was that the distance of the fuel layer from the surface defined as the ullage significantly influences the burning behavior. As the oil slick thickness kept at 1.5 ± 0.2 cm, the average burning rate per area ($\text{g}/\text{cm}^2\text{-s}$) and the removal efficiency are the same as the pool size increases from 100 cm to 150 cm. However, as the ullage decreases from 20 cm to 10 cm, the overall burning rate per unit area decreased by 10%, and efficiency decreases by 3%. Further, the low ullage burns had longer burn durations (20%) which lead to average fuel penetration into the ice (lateral cavities) increase by 40%. However, with only 2 large-scale tests at two different initial ullage conditions, the results though fascinating are still inconclusive and necessitate further experimentation.

Table 6.1: Test matrix of large-scale tests performed at WPI and CRREL

Test	Ice pool size, LxW (cm^2)	Ice condition	Ice thickness, H (cm)	Ullage, h (cm)	Oil added (kg)	Calculated oil thickness (cm)
1 ^[1]	117 x109	Fresh water ice	25	20	9.8	0.8
2	105 x101		25	20	10.0	1.0
3	103 x101		25	20	13.2	1.3
4	100 x100	Salty water ice	45	20	14.0	1.5*
5	150 x150		45	20	24.5	1.3*
6	100 x100		35	10	15.7	1.7*

The experiments performed at the small and intermediate scale were used as a guide to develop the large scale tests. The following parameters were varied:

1. Ice pool size: increases from 1 m (Test 1-4, Test 6) to 1.5 m (Test 5);
2. Ullage distance: decreases from 20 cm (Test 1-5) to 10 cm (Test 6);
3. Oil thickness: 1.0-1.5 cm.

Alaska North Slope (ANS) crude oil was used with similar initial temperature at around 0 °C for all tests. Oil thicknesses in Test 4-6 were around 1.5 cm, which included the effect of a water loss or gain because of a leak between 2 ice ponds. The water level descended at the beginning of Test 4 and 5 at a rate of around 2.2 mm/min, and stayed at a constant level temporarily at the beginning of Test 6. The leak was found during preparation for Test 4 when adding water to the ice cavity to reach the required ullage distance. Consequently, the oil pour in time was reduced significantly (oil was poured in 220s, 75s and 71s Test 4 - 6) to minimize

⁴ Some contents of this chapter were published as:

1. X. Shi, P. W. Bellino, A. S. Rangwala, "Flame Heat Feedback from Crude Oil Fires in Ice Cavities," *Arctic Marine Oilspill Program (AMOP) technical seminar on environment contamination and response*, vol. 38, Jun 2 – 4, 2015, Vancouver, British Columbia, Canada
2. X. Shi, A. S. Rangwala, "Study of In-situ Burning Flame Heat Feedback in Ice Cavities," Eastern States Spring Technical Meeting, Princeton University, Mar 13 – 16, 2016.

the impact of the leak between the ponds. It was noticed later that the oil/water level in the testing cavities actually descended or ascended at an unsteady rate until a balance was achieved between 2 ponds.

6.2 Experimental setup

Fig. 6.1 shows the experimental setup used in the indoor and outdoor tests. Details of the instrumentation are described below.

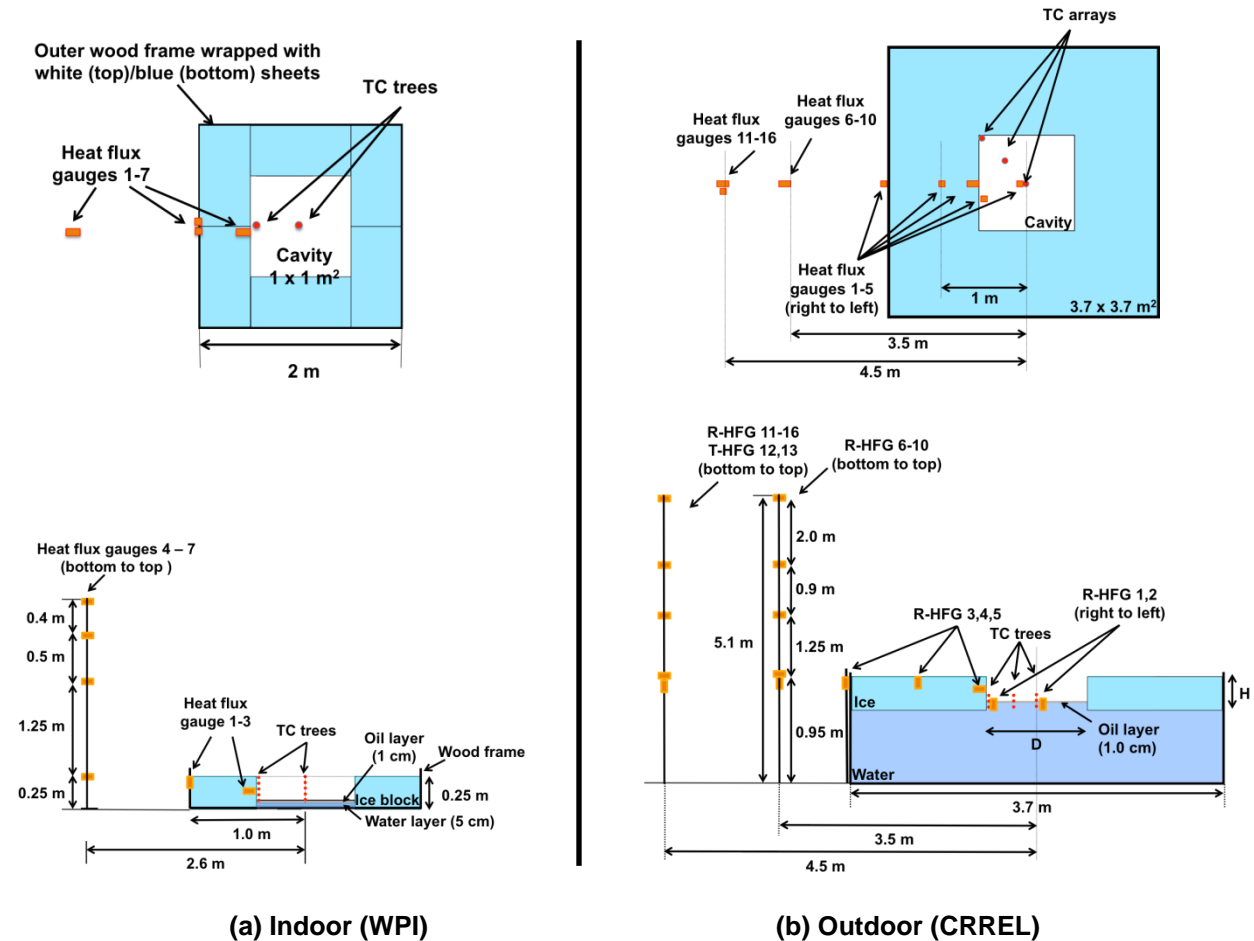


Fig. 6.1: Schematic of experimental setup.

6.2.1 Indoor tests (WPI)

Two large-scale experiments were conducted at the WPI fire laboratory with similar test conditions used in Test 1 [2]. Figure 6.1a shows the experimental setup consisting of a 2 m (L) × 2 m (W) × 0.28 m (H) outer frame made of plywood wrapped with two 3.5 × 4.5 m² fire-resistant and waterproof tarps. Six carved ice blocks, of 1 × 0.5 × 0.25 m³ and 136 kg (300 lb) each, were placed around the perimeter of the container, leaving a 1 × 1 m² area at the center with a cavity depth of 0.25 m. Ice blocks were fused together to prevent the oil from spreading into the gaps during combustion. A layer of water (5 cm) was added into the cavity to prevent the oil from spreading underneath the ice blocks.

Two identical thermocouple trees (32 thermocouples in total) were placed inside the cavity, one at its center and one adjacent to the wall (see Fig. 6.1a), to measure the temperature distribution and record the motion of the liquid layer. Spacing between thermocouples on each

tree is shown in Fig. 6.2a. K-type insulated thermocouple wire (Omega, GG-K-30-SLE) was used, which was welded to produce measuring junction (bead) by an Omega thermocouple welder (TL-WELD). Thermocouples were supported by two separate 14 cm long stainless steel plates with acrylic bases. Each thermocouple was inserted into a ceramic insulating tube (1.6 mm inner diameter), leaving only the bead exposed (5 mm from the tip of the ceramic tube). It was then bounded to the stainless steel supporting plate using thermocouple cement. Thermocouple wires passed underneath the ice blocks to a data logger located 5 m away from the pool centerline.

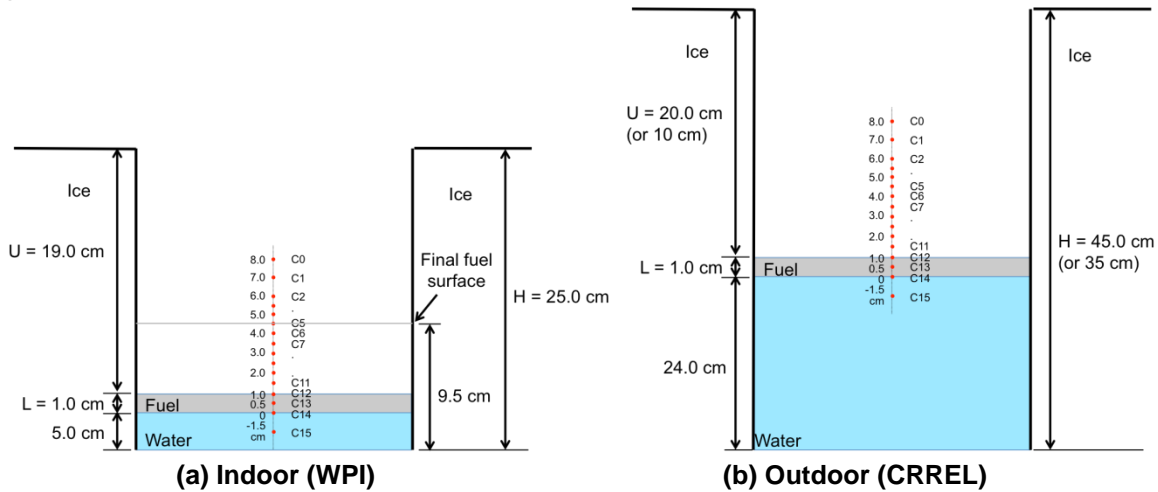


Fig. 6.2: Deployment of TC trees in ice cavity

Six water cooled total heat flux gauges and one radiometer (Medtherm 64 series) were used to measure the heat flux emitted by the flame to the environment and to the ice surface. One heat flux gauge (Heat flux gauge 1 in Fig. 6.1a) was placed inside of the cavity, 8.5 cm above the initial oil surface. Radiometer 2 and total heat flux gauge 3 were placed on the top surface of the ice (0.25 m above ground) side by side, 1 m away from the center of the ice cavity. Their measuring surfaces were pointed upward to measure the flux from the flame that reached the ice surface. Four additional heat flux gauges were placed 2.6 m away from the center of the ice cavity and 0.25, 1.5, 2.0 and 2.4 m above ground (Heat flux gauges 4-7 in Fig. 6.1a, respectively) to measure the heat flux emitted by the flame towards the ambient. These four total heat flux gauges were far enough so that the convection was ignored and their measurements are assumed to be the radiation only.

Two video cameras were used to record the burning process: one faced the flame to record the flame size and the other one was placed above the flame to record the change in the cavity geometry. ANS crude oil was poured into the ice cavity to form a 1.0 cm thick oil layer above the water base, as shown in Fig. 6.2a. The oil temperature was 9.5 °C before the ignition. The oil was ignited by a butane torch with an extended arm. The fire extinguished naturally after ~200 seconds. The remaining oil (heavy component residue) was collected by 3M oil-only absorbent pads. The absorbent pads were weighed before and after the clean up to obtain the average burning rate and burning efficiency. Fig. 6.3 shows a photographic record of set up, oil fill, ignition, burn, and post burn lateral cavity photos of the large scale indoor test.



Fig. 6.3: Photographic record of large scale indoor test using Alaska North Slope (ANS) crude oil

6.2.2 Outdoor tests (CRREL)

Two ice ponds were prepared by CRREL by growing ice with thicknesses of 45 cm and 35 cm from 35 ppt artificial salty water in two 370(L) × 370(W) × 95(H) cm³ concrete containments. An aerial view of the test set up showing the 2 ice ponds (one is ignited) is shown in Fig. 6.4. A 100 × 100 cm² cavity was cut at the center of each pond for the burn test. After the first test, the cavity was cut further more to make a 150 × 150 cm² pool for the 2nd test in the same pond. Figure 6.1b shows the layout of the outdoor experimental setup.

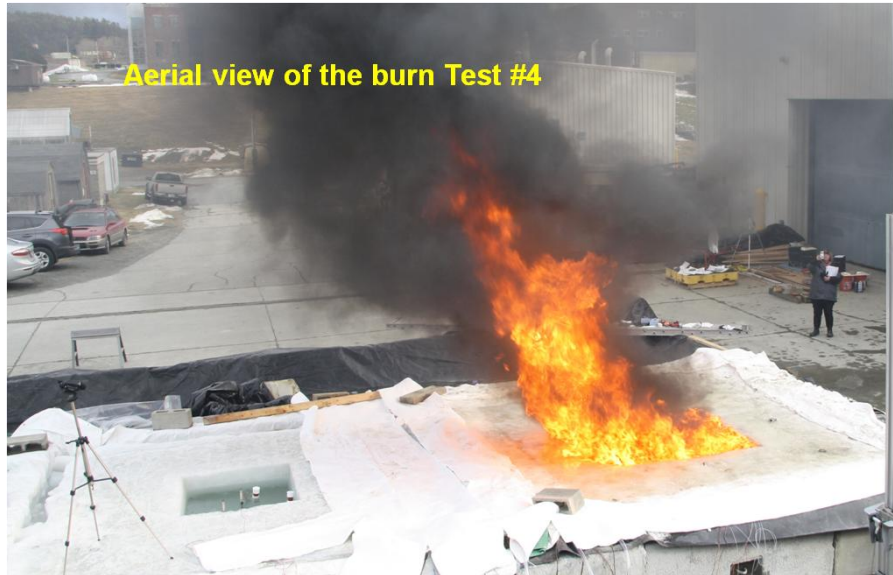


Fig. 6.4: Photograph showing the outdoor burn site at the US Army Cold Regions Research and Engineering Laboratory outdoor test facility in Hanover NH.

Three identical thermocouple trees (16 thermocouples each) were placed inside the cavity along the diagonal of the cavity: center, corner of the ice wall and in-between (see Fig. 6.1b and Fig. 6.5), to measure the temperature distribution and record the motion of the liquid layers. Spacing between thermocouples on each tree is shown in Fig. 6.2b. Thermocouple trees (TC) were built using the same procedure as the indoor tests performed at WPI. A closeup view of a TC tree is shown in Fig. 6.5 (left). Thermocouple wires passed underneath the ice layer and collected through a hole at the pond corner to connect to a data logger located 6 m away from the edge of the pond.

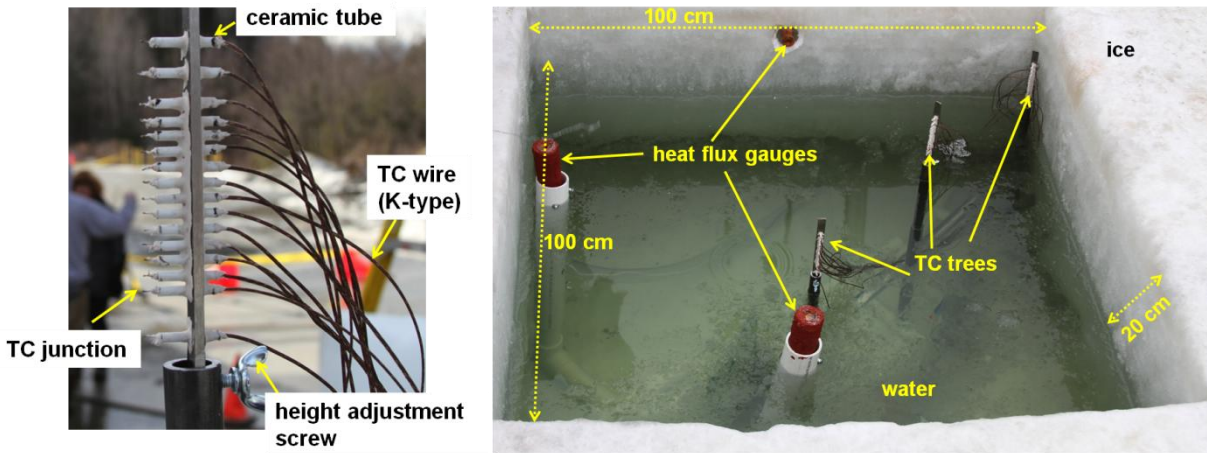


Fig. 6.5: Close up of TC tree (left) and deployment of 3 TC trees and heat flux gauges in the ice cavity (right)

Sixteen water cooled Medtherm 64 series heat flux gauges (14 radiometers and 2 total heat flux gauges) were used to measure the heat flux emitted from the flame to the oil surface, ice cavity wall, ice surface and to the environment. Two radiometers (R-HFGs 1,2 shown in Fig. 6.1b) were placed inside the pool (at center and adjacent to the wall) with their measuring surfaces 6 cm above the initial oil surface, pointing upward to measure the radiative heat flux received on oil

surface. Radiometer 3 (R-HFG 3) was placed on the side wall of ice cavity, 10 cm above the initial oil surface, with measuring surfaces pointing horizontally to measure radiative heat flux received on ice wall. Radiometers 4-5 were placed on the ice surface, 1 m and 1.9 m away from the pool centerline. Their measuring surfaces were pointed upward to measure the radiative heat flux on the ice surface. Other radiometers (R-HFGs 6-11, 14-16) were placed 3.5 m and 4.5 m away from the center of the ice cavity at heights of 0, 1.25, 2.15 and 4.15 m above ice surface to measure the heat flux emitted by the flame towards the ambient. Total heat flux gauges (T-HFGs 12, 13) were placed at distance of 4.5 m with their the height aligned up with ice surface. Four video cameras were used to record the burning process: three faced the flame to record the flame size and geometry from different angles and one was placed above the flame to record the change in the cavity geometry. High resolution still photographs were also taken to record burning behavior at different stages.



Fig. 6.6: Pouring of ANS crude oil in an ice cavity using a Teflon board to prevent spillage.

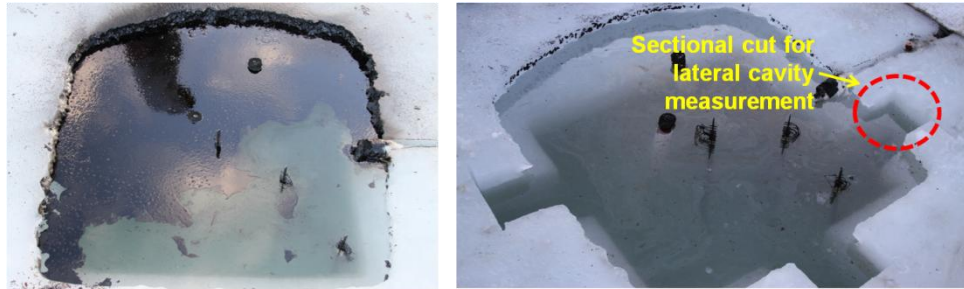
ANS crude oil was poured into the ice cavity to form a ~1.0 cm thick oil layer above the water base for all 3 burn tests. A teflon board was used to prevent splashing of the oil during the pour as shown in Fig. 6.6. Oil temperature was maintained at -1 °C before ignition. Oil was ignited by a butane torch with an extended arm as shown in Fig. 6.7.



Fig. 6.7: Ignition of ANS crude oil in an ice cavity at CRREL

The fire extinguished naturally and the remaining oil (heavy component residue) was collected by a rake and 3M oil-only absorbent pads. The collected residue was weighed along with all

contaminated tools used for after burn clean-up (rake, absorbent pads, gloves) to obtain the average burning rate and burning efficiency.



Test #6: post burn (before clean up)

Test #6: post burn after clean up

Fig. 6.8: Photograph of the cavity just after combustion of the oil and after clean up by oil-only absorbent pads.

Figure 6.8 shows the photographs of an experimental trial immediately after self extinction, and after clean up with the absorbent pads. The cross sectional cuts in the ice used to determine the lateral penetration are also shown in the photographs.

6.3 Experimental results and discussion

Table 6.2 shows the summary of ANS crude oil burning in all 5 large scale tests during the project along with the first test in 2013. The oil slick thicknesses used in 3 outdoor tests were 1.5 ± 0.2 cm thick, which is slightly thicker than the slick (1 cm) used in previous indoor tests. The results show that the average burning rate per unit area increases slightly as the pool size increases, while the burn efficiencies are about the same. As the ullage decreases from 20 cm to 10 cm, both the burning rate per unit area and the burning efficiency decrease. The cavity of 100×100 cm² initially with ullage of 20 and 10 cm, respectively, expanded 44% and 64% by area after the burn. The comparison with indoor tests shows that cavity expansion in fresh water ice is smaller than salty water ice.

Table 6.2: Results of large-scale tests. Tests 1 – 3: Indoor tests performed at WPI using fresh water ice. Tests 4-6 are outdoor tests performed at CRREL using salt water ice.

Test	Cavity size (cm ²)	Ullage (cm)	Oil thickness (cm)	Mass flux (g/s-cm ²)	Efficiency	Time to boilover (s)	Burn time (s)	Cavity_final (cm ²)	Cavity expansion	χ_R
1 ^[1]	113 x113	20	0.8	0.0033	85%	140	197	117 x117	7%	NA
2	105 x101	20	1.0	0.0039	82%	130	200	112 x110	16%	NA
3	103 x101	20	1.3	0.0043	85%	160	251	113 x111	21%	NA
4	100 x100	20	1.5	0.0042	92%	180	305	120 x120 (± 1)	44%	28%
5	150 x150	20	1.3	0.0044	91%	160	227	170 x170 (± 4)	28%	17%
6	100 x100	10	1.7	0.0038	89%	250	367	128 x128 (± 6)	64%	25%

Heat flux measured at 3.5 and 4.5 m away from the pool centerline are used to find the fraction of flame heat loss to the ambient (χ_R), which is defined as:

$$\chi_R = \dot{Q}_R / \dot{Q}, \quad (1)$$

where \dot{Q}_R is the total radiant energy emitted from the flame and \dot{Q} is the total heat released by the flame. Assuming the radiative energy to be isotropic

$$\dot{Q}_R = 4\pi L^2 \dot{Q}'' , \quad (2)$$

where \dot{Q}'' is the data recorded by the heat flux gauges located at distance of L . The total heat release rate from the flame was obtained by

$$\dot{Q} = \dot{m} \cdot \Delta H_C, \quad (3)$$

where \dot{m} is the average mass loss rate (g/s) and ΔH_C is the heat of combustion of the crude oil (44.77 kJ/g @ 25°C) by assuming complete combustion. Using Eqns. 1-3, the average radiant fraction χ_R in each outdoor test is found in a range of 17-28%. Radiant fractions in all the indoor tests were not available because of instrumentation limitation. The results of 100 cm pool with ullage distances of 20 and 10 cm show the fractions of 28% and 25%, which are in agreement with hydrocarbon pool fires of 1 m diameter size range. The fraction of heat loss to ambient with 150 cm pool is 17%, which is mainly because of a very windy condition during the test. The flame was tilted a lot most of the time so that less radiant flux was captured by the heat flux gauges placed 3.5-4.5 m away. In the outdoor tests, wind plays a significant role in the burning behavior. For example in one trial shown in Fig. 6.9, strong winds caused herding of ANS crude oil towards one end of the cavity.



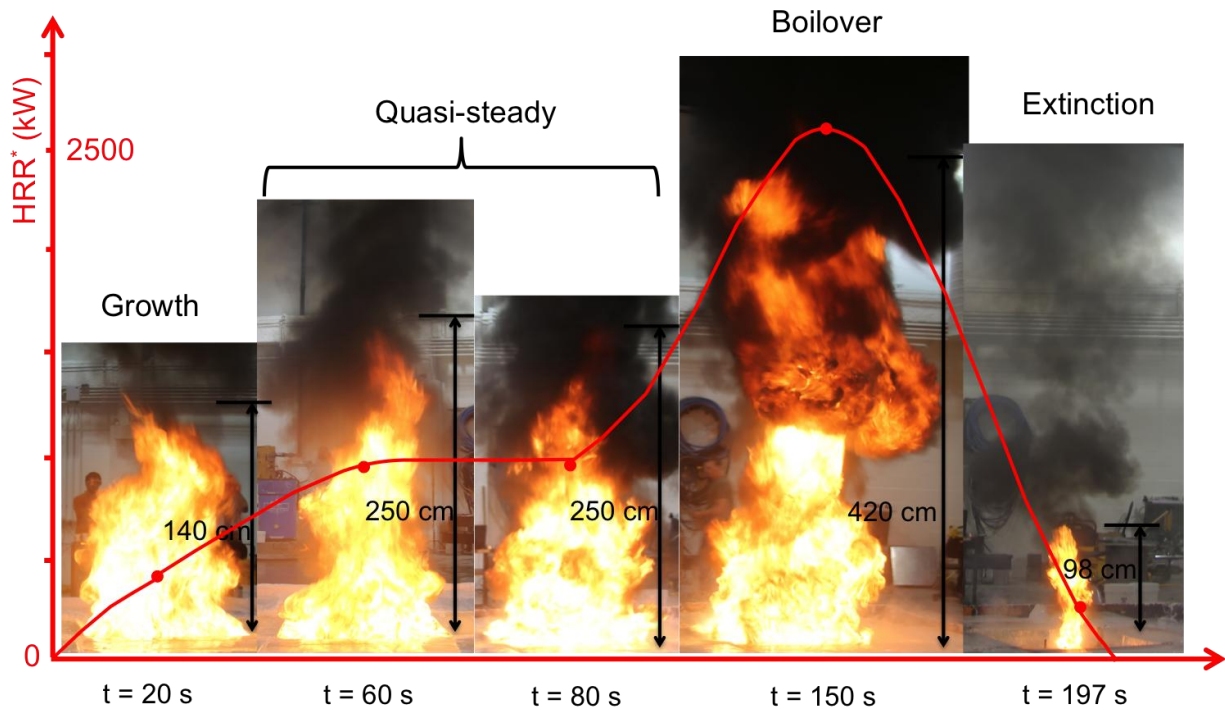
Fig. 6.9: Herding effect caused by strong winds during outdoor testing at CRREL

Typical burning behavior in all experimental trials (both indoor and outdoor) is similar: ignition is followed by a short growth phase, followed by an extended quasi-steady burning. Depending on the initial thickness of the oil and ullage height the water sub-layer boils over at some point that results in significant enhancement of the overall burning rate and flame radiation. Time to boilover in the test is also shown in Table 6.2. But the tests with the same ullage height (20 cm) and similar slick thickness are shown to reach the boilover stage all at around 160 seconds (Test 1-5), except Test 6 with a 10 cm ullage height (250 seconds). Hence, boilover seems not dependent of the water sublayer thickness when burning in ice cavities (as long as there is no moving current of water below the oil surface to take the heat away), but dependent on the slick thickness and the ullage. The boilover phase is followed by natural extinction. Series of photographs are presented in Fig. 6.10 (a- f) to show this burning behavior.

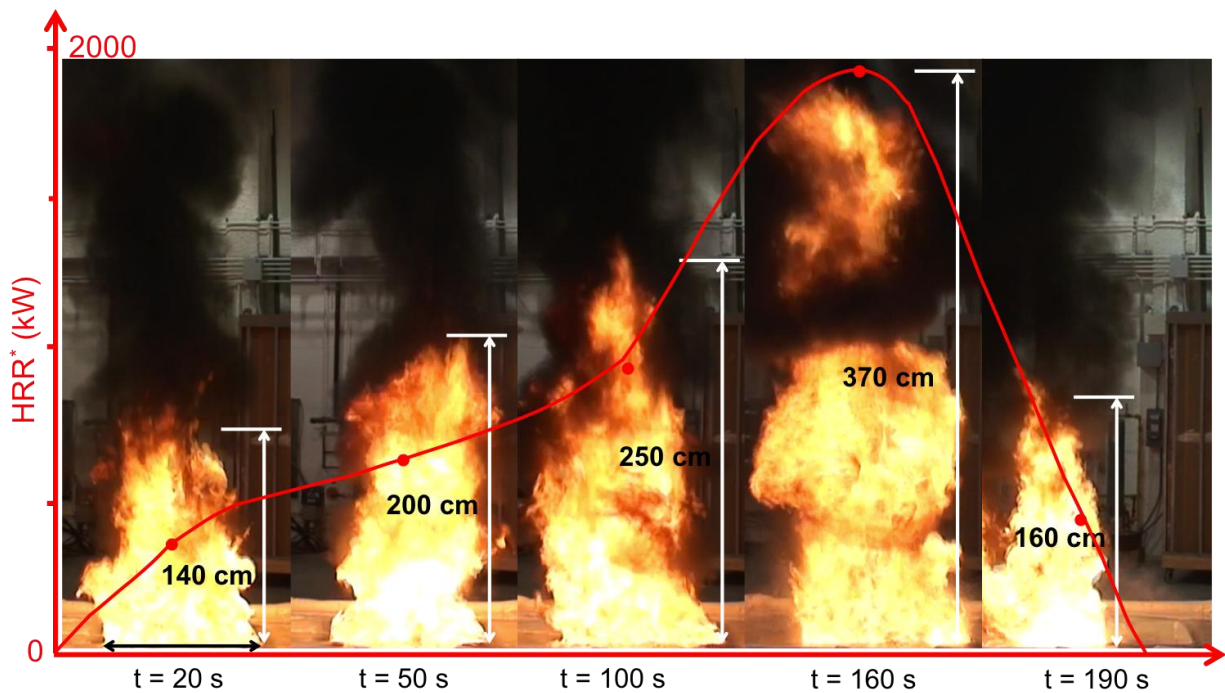
Flame height and heat release rate

Figure 6.10 also shows the flame heights at various burning stages for all the indoor and outdoor tests. The corresponding heat release rates are calculated using Heskestad's

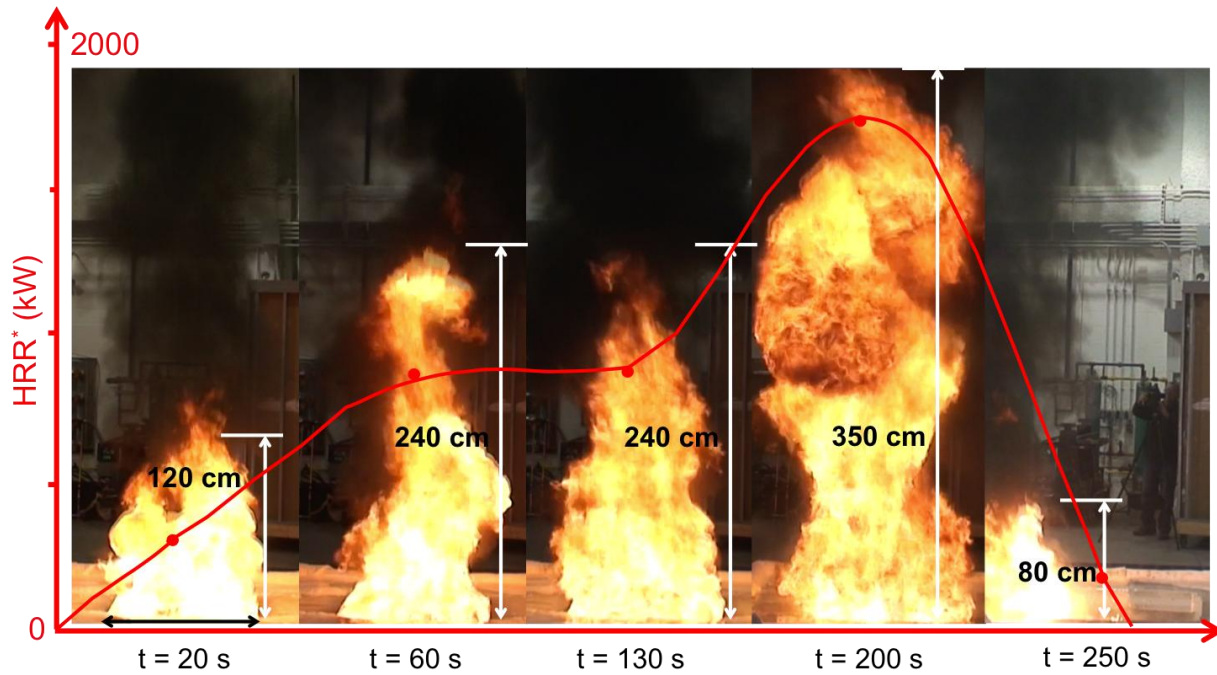
correlation [3]. As mentioned earlier, wind influence during outdoor tests are not negligible, the total heat release rate calculated based on the flame heights are therefore less accurate as those during the indoor tests.



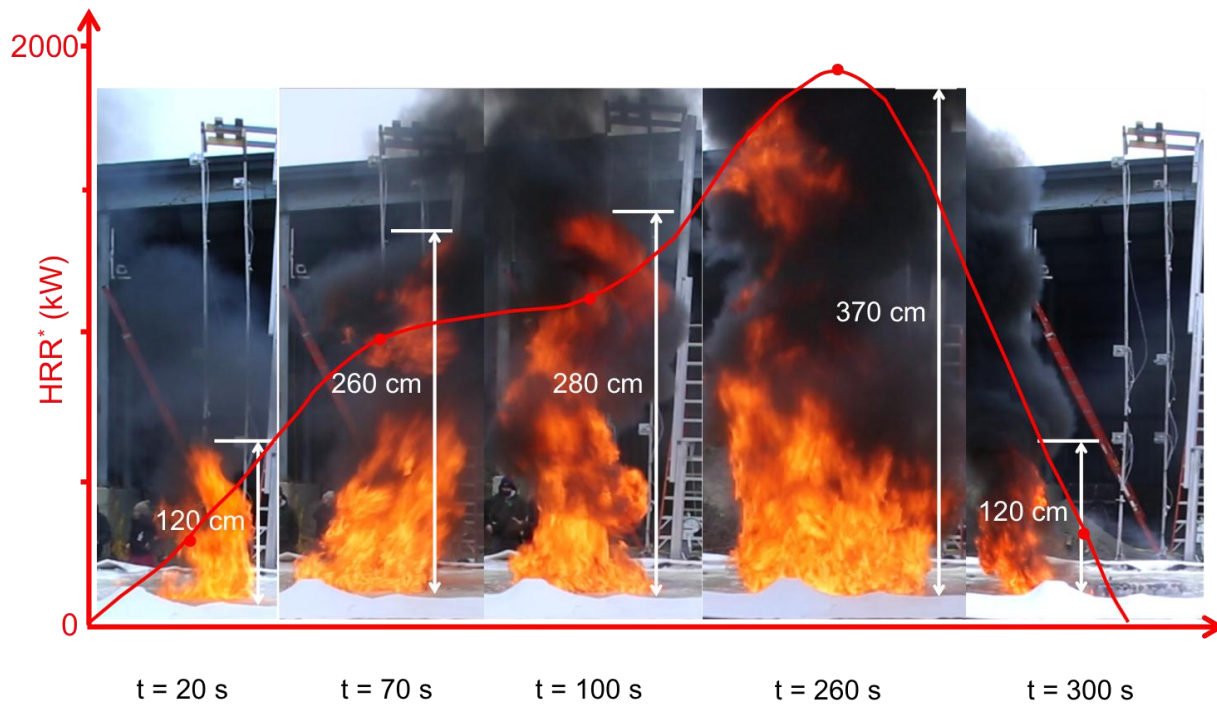
(a) Test 1^[1], indoor, $D = 1.1$ m, $h = 20$ cm.



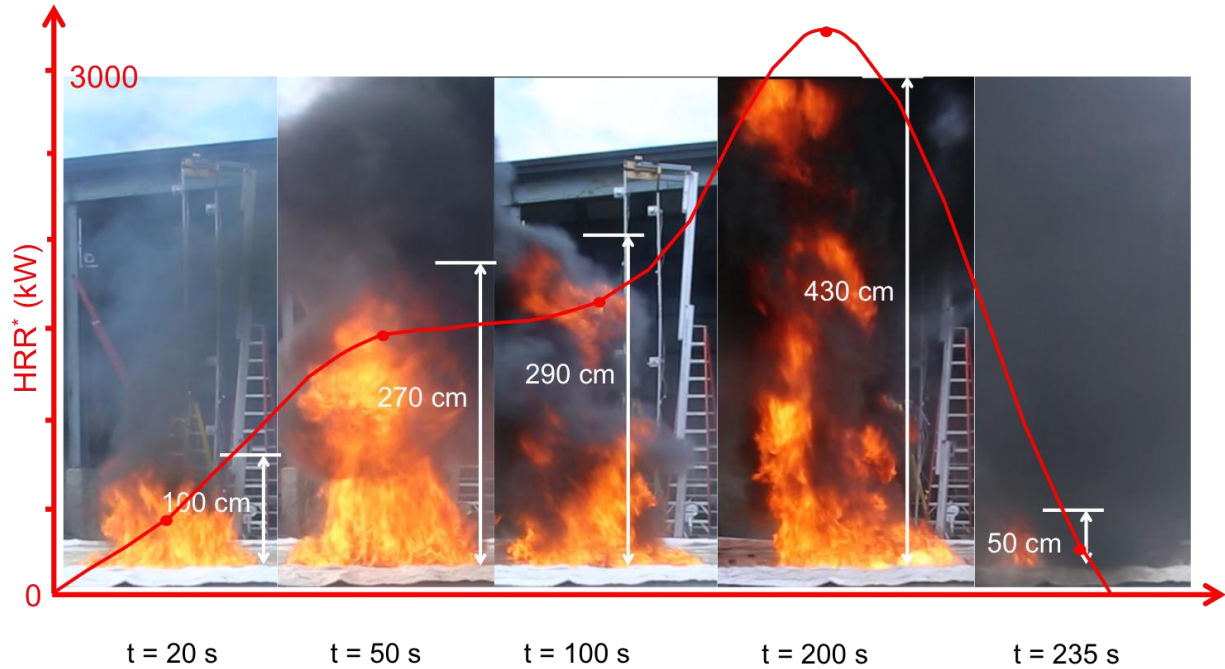
(b) Test 2, indoor, $D = 1$ m, $h = 20$ cm.



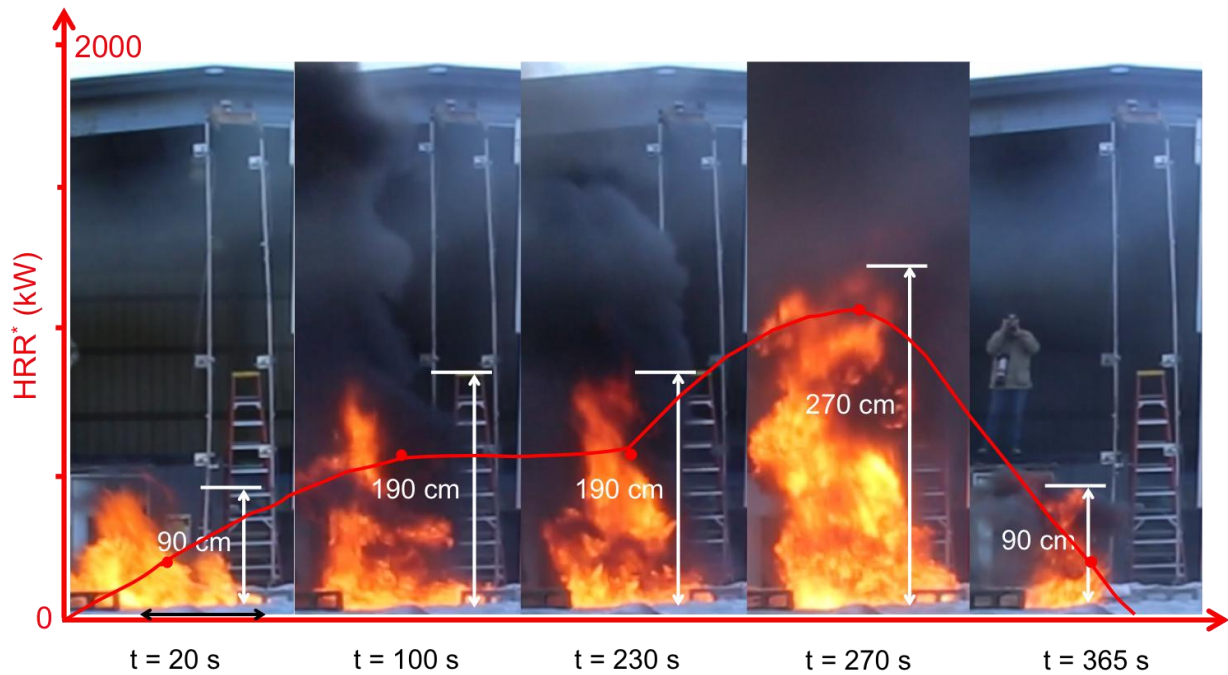
(c) Test 3, indoor, D= 1 m, h= 20 cm.



(d) Test 4, outdoor, D= 1 m, h= 20 cm.



(e) Test 5, outdoor, $D= 1.5 \text{ m}$, $h= 20 \text{ cm}$.



(f) Test 6, outdoor, $D= 1 \text{ m}$, $h= 10 \text{ cm}$.

Fig. 6.10: Flame at different stages in Test 1 – 6

Figure 6.10 shows that the flame height at quasi-steady stage in cavity of 1 m with 20 cm ullage was around 2.5 m (2.5D), which increased to around 3.7 m (3.7D) at the intense burning stage of boilover. Total heat release rate increased from around 1000 kW during quasi-steady stage to 2000 kW during boilover. As the ullage height remained the same at 20 cm and the cavity size

increased to 1.5 m, the flame height increased from around 3 m (2D) at quasi-steady stage to 4.3 m (2.9D) at boilover. Similarly, as the cavity size remained the same at 1 m and the ullage height decreased to 10 cm, the flame height increased from 1.9 m (1.9D) at quasi-steady to 2.7 m (2.7D) at boilover. The corresponding heat release rates at all stages during each test are compared in Fig. 6.11. It is clear that both the cavity size and the ullage play an important role to the total heat release rate, the burning rate, and efficiency.

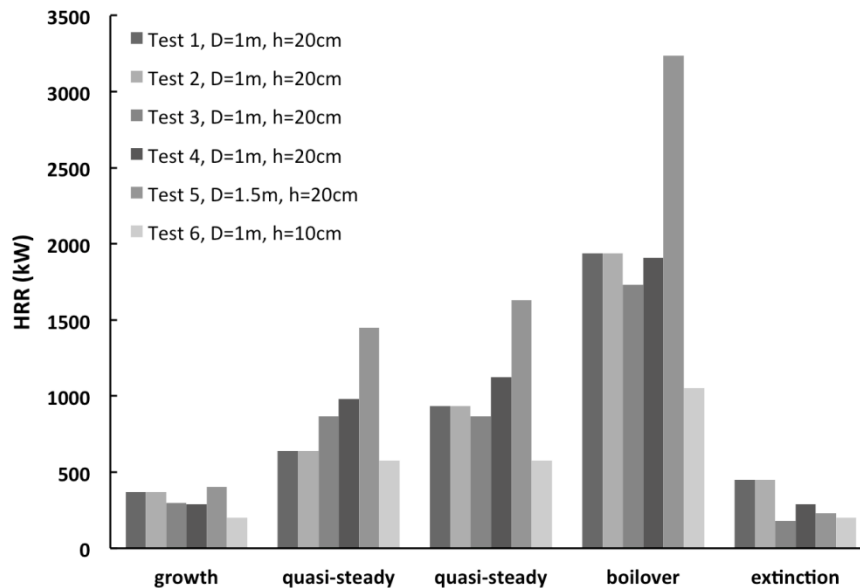


Fig. 6.11: Heat release rates in Test 1 – 6

The burning efficiencies shown in Table 6.2 are high mainly because of fresh ANS crude oil was used in all tests. As shown in Chapter 5, sufficient weathering is caused at low temperature conditions ($\sim 0^\circ\text{C}$) to reduce the flame spread rate significantly. The influence of the cavity size and ullage on the burning behavior will change with weathered oil and necessitate future research especially towards development of a predictive model that can account for fuel properties, geometry effects due to ullage and ice melting.

Temperature profiles

Vertical TC trees were used in the tests to measure in-depth temperature distribution inside oil/water layer at 3 different locations inside the ice cavity. Figure 6.12 shows the raw data of in-depth temperature distribution of one TC tree recorded during an indoor test ($D = 1\text{ m}$, $h = 20\text{ cm}$). Oil surface temperatures are represented by plateaus shown in each temperature curve. The temperature profiles show that when a slick of ANS crude oil burns, the lighter components burn first and leave the heavier components in the slick to be heated up to vaporize and burn gradually. Heavier components have higher evaporation (boiling) temperatures, which results in an increasing surface temperature during the burn. At the same time, a hot layer is gradually formed and gets thicker until it reaches the slick bottom. The range of ANS crude oil surface temperatures with 1-1.5 cm thickness and burning on a water sublayer are typically in a range of $170\text{--}360^\circ\text{C}$ before boilover. The experimental data shown in Fig. 6.12 shows this range during the burning of a slick of 1 cm ANS crude oil. Bench scale experiments performed during the smoke point tests (refer Chapter 2) also show a similar range of surface temperature.

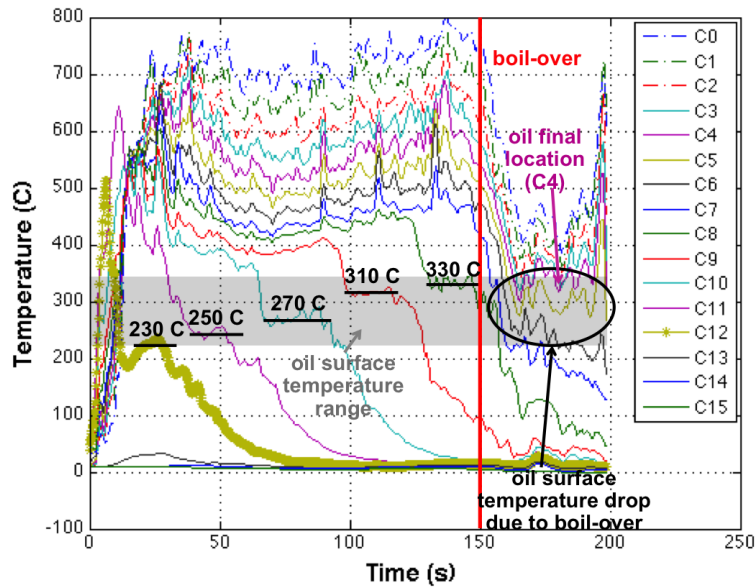


Fig. 6.12: Temperature profiles of 20 cm ullage in 1 m ice cavity (Test 2 in Table 6.2)

As the ice melts, the melted water causes the oil layer to rise. This is opposite to the burning behavior in a tank where the ullage or the distance of the fuel layer from the surface decreases with time. The movement of the oil layer was tracked using the in-depth temperature data as shown in Fig. 6.13. The raw thermocouple data was first smoothed by using a moving average (Fig. 6.13) and then the smoothed data was processed to identify the oil level movement by specifying a threshold temperature around the oil boiling temperature as shown in Fig. 6.13.

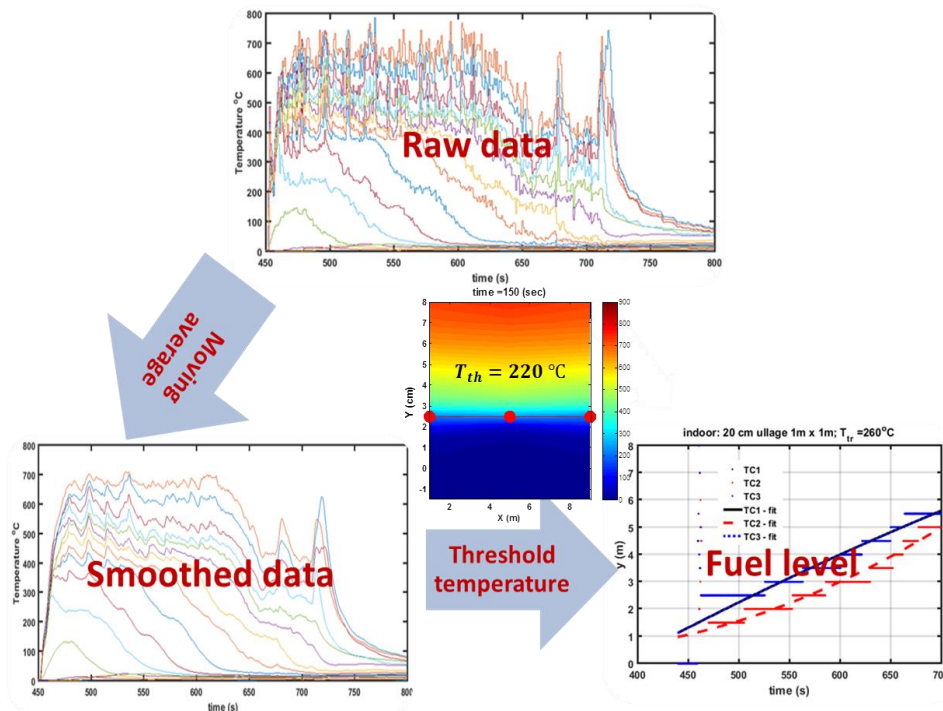


Fig. 6.13: Schematic representation of the processed thermo-couple data.

Figures 6.14 – 6.16 show the experimentally measured temperature contours of crude oil for 20 cm ullage (indoor-outdoor) and 10 cm ullage (outdoor). Linear interpolation is used to create the contour from three TC trees (Fig. 6.5). A constant threshold temperature of 220 °C is used to approximately track the movement of the oil layer. While this is not an accurate representation of the time varying ANS oil surface temperature, the contours provide a qualitative trend of the temperature within the cavity. Other threshold temperatures were also tried (180 °C, 200 °C, and 240 °C) and show a similar qualitative trend of fuel movement.

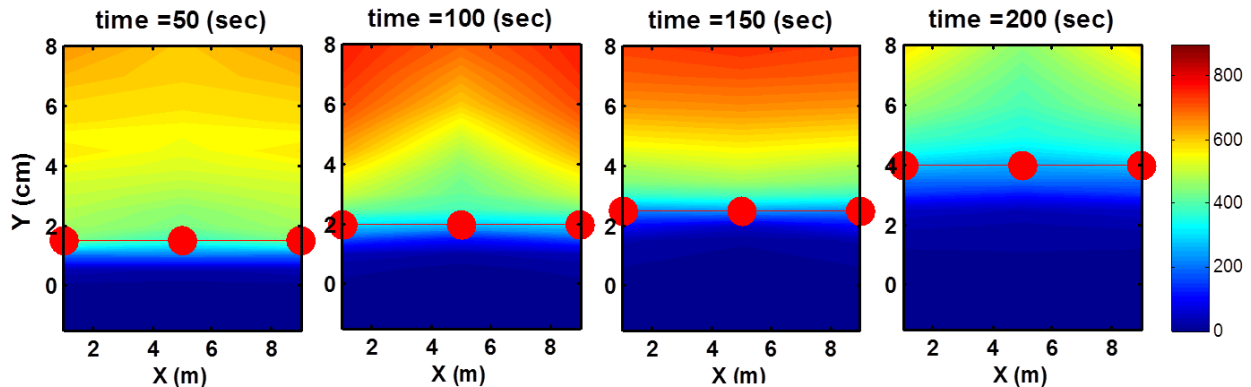


Fig 6.14: Contours of the temperature and fuel level indicator for a threshold temperature of 220 °C at different times for 20 cm ullage of 1m x 1m ice cavity: indoor test

The fuel level movement is observed to be faster in the case of 20 cm ullage for indoor and outdoor tests compared to the 10 cm ullage outdoor test. The threshold temperature is shown by the circular red symbols in Figs. 6.14 – 6.16. The qualitative trend of the temperature of the hot gases above the fuel layer in the cavity is clearly visible in Fig. 6.14. At 50 s, only the high volatile components of the fresh ANS crude oil are burning away. This causes the flame standoff to be higher. At 100s (Fig, 6.14) the flame standoff decreases because of the heavier components beginning to vaporize and finally at 150 s, the hot layer above the fuel surface is uniform showing signs of partial premixing. The region between ~70 to 150s is also the duration where most of the fuel is burned at the quasi steady state as shown by the flame photographs in Fig. 6.10 b and c. At 200s, boilover starts and the flame standoff once again increases significantly.

In the 20 cm ullage case, the entrained air interaction within the cavity causes partial premixing of the fuel vapor in the cavity. This significantly increases the radiative and convective heat flux inside the cavity also shown by the heat flux measurements discussed in the next section. It should be noted here that, there is a slight difference between indoor and outdoor tests of 20 cm ullage which may be because of the water leak discussed earlier.

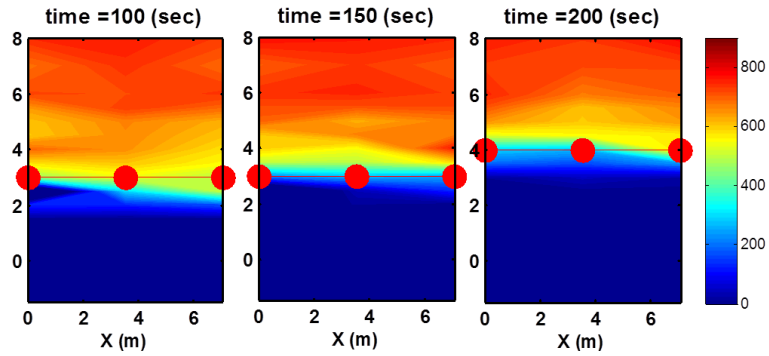


Fig. 6.15: Contours of the temperature and fuel level indicator for a threshold temperature of 220 °C at different times for 20 cm ullage of 1m x 1m ice cavity: outdoor test

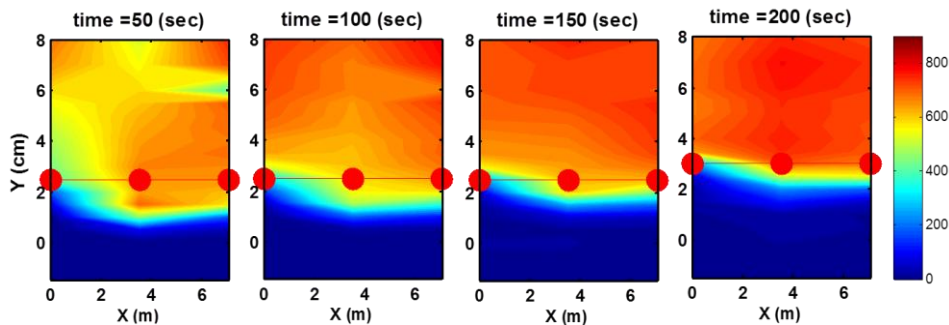
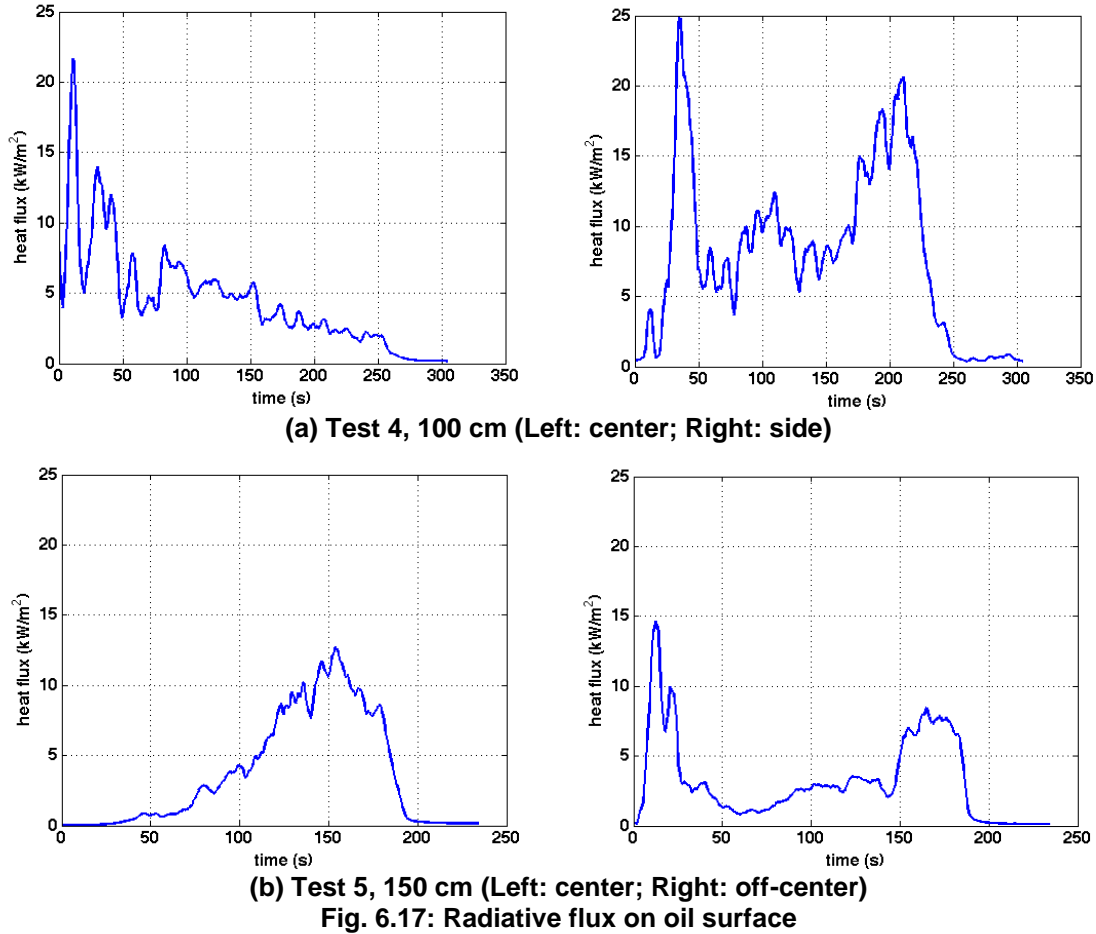


Fig. 6.16: Contours of the temperature and fuel level indicator for a threshold temperature of 220 °C at different times for 10 cm ullage of 1m x 1m ice cavity: outdoor test

Heat flux at oil surface

Figure 6.17 shows the radiative heat flux measured on the oil surface in Test 4 (1m) and Test 5 (1.5m) by radiometers R-HFGs 1-2 located in the liquid and facing up. The initial peak of 15-25 kW/m² was because of the butane igniter torch. The average heat flux received by the surface before boil-over for Test 4 (size of 1 m) was 3.1 kW/m² at center and 18.2 kW/m² close to the wall, and 9.1 kW/m² at center and 3.2 kW/m² at off-center for Test 5 (size of 1.5 m). The peak heat flux at center in Test 4 equals 7 kW/m², and 12 kW/m² in Test 5. The increase in the heat flux as the pool size increases is most likely because of enhanced radiation by soot.



Radiant fraction at quasi-steady state

Average radiant fraction in each test was calculated by the experimental heat flux data recorded during the test and the average mass burning rate calculated using the mass of oil before and after the test. In both indoor tests at WPI and outdoor tests at CRREL, boilover plays a significant role to enhance the burning and therefore increase the total burning rate and efficiency at the end. In the Arctic conditions, a cold water current under the ice lead may increase heat transfer between the oil and water layer and boilover may be delayed or not occur at all.

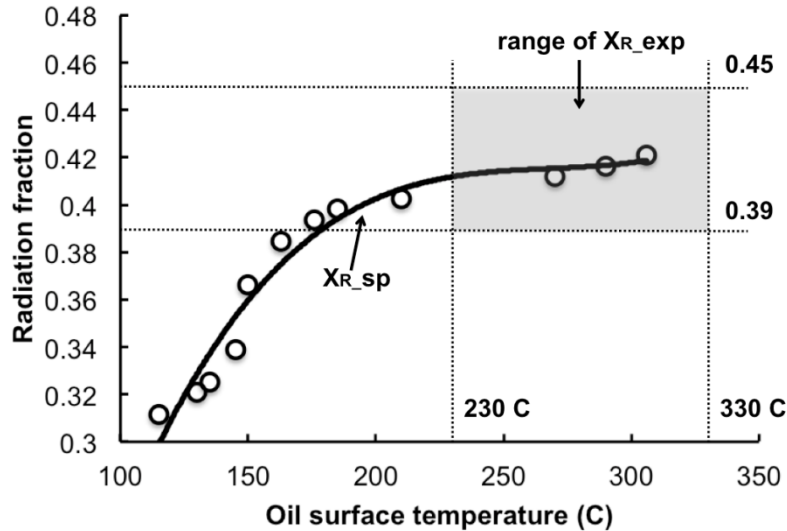


Fig. 6.18: Radiation fraction found experimentally and theoretically (smoke point)

In general, time to boilover is increased because of the cold water sublayer and surrounding ice, therefore, the prior boilover burning behavior (quasi-steady stage) is important in this study. Flame height at quasi-steady state, along with the heat flux measured experimentally (at 3.5 and 4.5 m away from flame axis) is used to find the quasi-steady radiant fraction χ_{R} . Here the total heat release rate \dot{Q} is calculated by $L_f = 0.23\dot{Q}^{2/5} - 1.02D$ [3], where L_f is the flame height. The radiant fractions at quasi-steady states of CRREL tests (χ_{R_exp}) are in a range of 39-45%, and shown in Fig. 6.18, along with the radiant fraction calculated from the smoke points of ANS crude oil (χ_{R_SP}). The oil surface temperature range (230 – 330 °C) used in the figure is from the in-depth temperature profiles in Test 2 and 3. The radiant fraction estimated by the smoke point height calculations (Chapter 2) are in a good agreement of the experimental data.

Lateral cavity formation

Lateral cavities, where the oil tends to penetrate sideways into the ice, thereby forming an ice “lip” was clearly observed after the burn in all the tests, as shown in Fig. 6.19. The lateral penetration into the ice wall in Test 1 and 2 were 11 cm, and 18 cm in Test 3. The variation of ± 1 cm is estimated based on an average of 4 cross sections of the ice wall taken from the four sides of the square cavity.

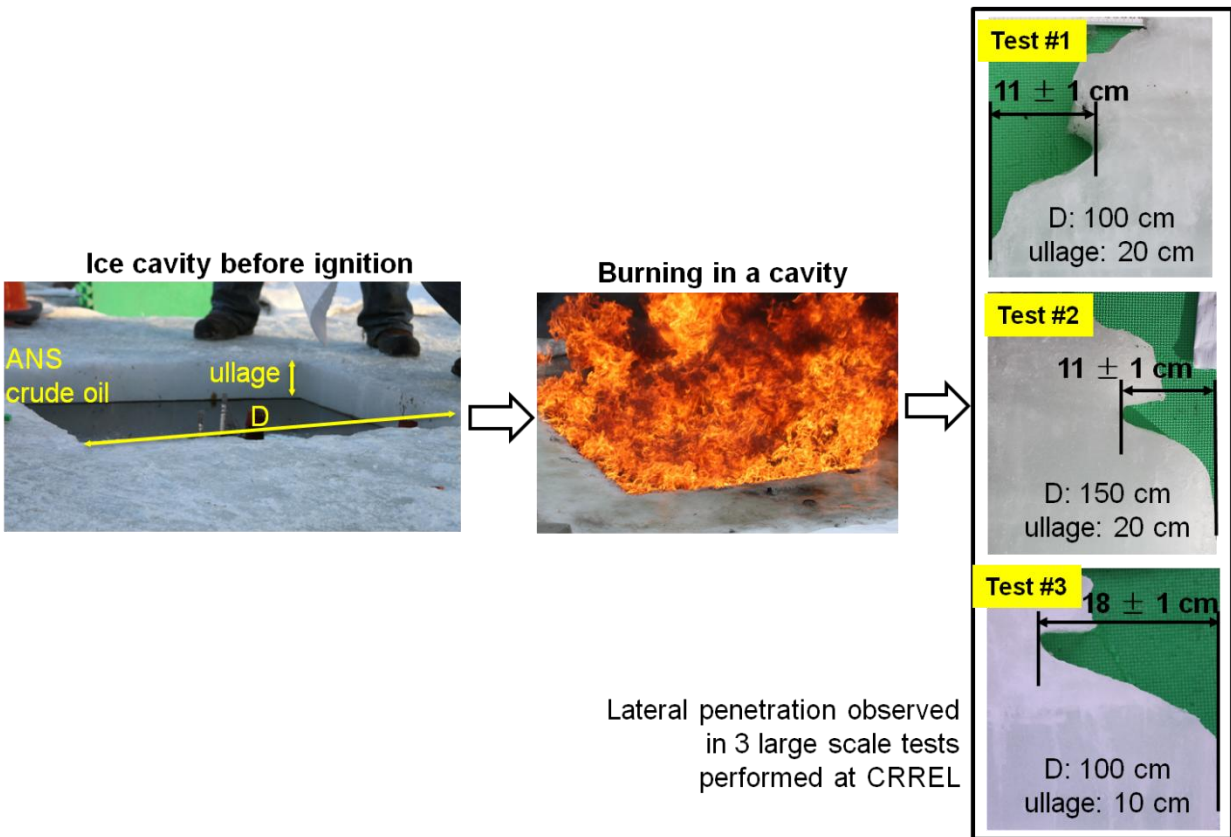


Fig. 6.19: Lateral cavity formation in tests performed with D ~1 to 1.5 m at CRREL

Figure 6.20 shows the lateral penetration length (L) observed in experiments at small, intermediate and large scale during the entire duration of the study. The initial diameter of the cavities range from 5 cm upto 150 cm with oil thicknesses between 1-1.5 cm.

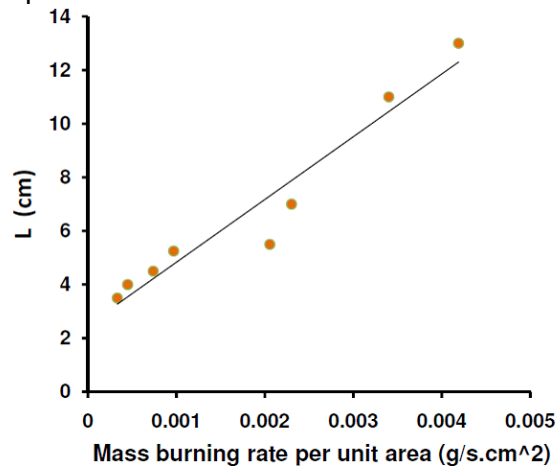


Fig. 6.20: Lateral penetration (L) as a function of burning rate per unit area

The penetration length is plotted as a function of the mass burning rate per unit area. As the burning rate per unit area increases, the oil penetration into the side wall increases. Thus enhancement in the burning rate usually comes at an expense of lateral cavities which increase the difficulty of oil cleanup as the oil hidden in the lateral cavity cannot be burned, and is also

hard to reach by mechanical recovery procedure afterwards. However, results also show that improved efficiencies can be obtained if the formation of the ice-lip can be avoided by selecting an optimized ullage for the burn. However, with only two large scale tests at two ullages, the results are not conclusive to provide specific guidelines.

Ullage effect on burning behavior of a cavity fire

Earlier discussion in the flame height and flame total heat release rate has showed that the ullage has an important influence on the burning behavior of large scale oil burning in ice cavities at the quasi-steady stage. After this stage, boilover further enhance the burning and therefore increases the total burning rate and efficiency at the end. This section explains the role of the ullage in a cavity, the mechanism/theory and the experimental results supporting it.

Figure 6.21 shows the airflow patterns in two geometries – above and below the ground which are denoted as “tank fire” and “cavity fire”. In a tank fire, air is pulled toward the flame bottom from the ground. A vertical boundary layer established on the wall of the tank causes the air entrainment rate into the fire to be weaker than the one in the case of cavity fire, where a recirculation zone is formed above the fuel surface as shown in Fig. 6.21b.

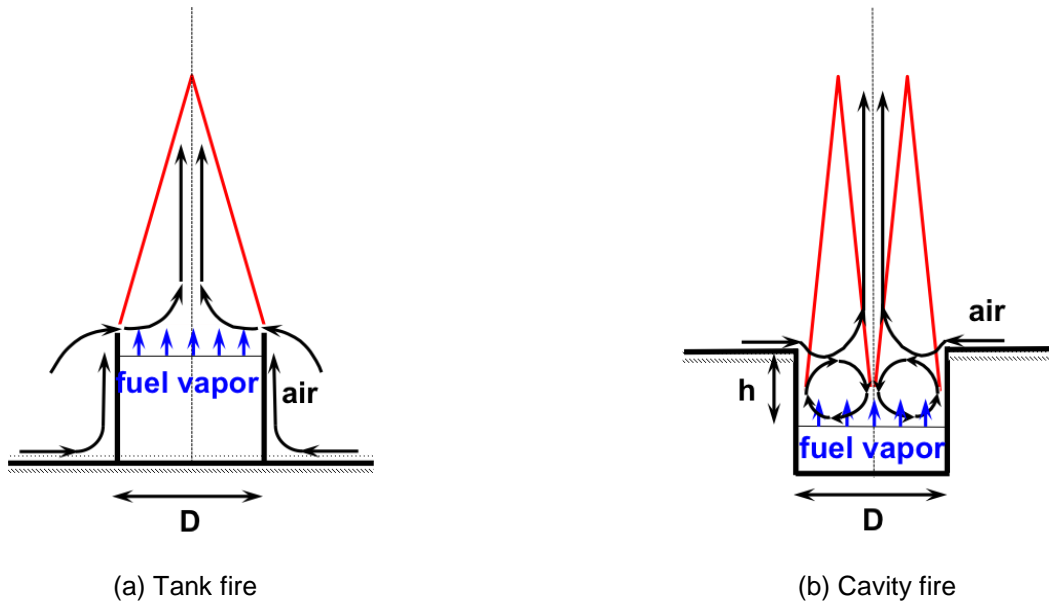


Figure 6.21: Airflow patterns of tank fire and cavity fire

In a cavity fire, the surface flanged around the top of the cavity strengthens or enhances the airflow that is pulled toward the flame. Air is able to be entrained into the ullage as ullage increases, forms the recirculation pattern above the fuel, and pre-mixes the fuel vapor with the air, as shown in Fig. 6.21b. This premixing action results in a faster reaction of fuel vapor with air, and more convective heat transferred to the fuel surface. When the geometry ratio (h/D , non-dimensional ullage) of cavity pool fire achieves its optimum value, the fastest reaction (burning rate) will occur.

The ullage effect on burning behavior of a cavity fire was first reported by Shi et al. [5]. It was noticed that there was an enhancement at the quasi-steady state in the indoor large scale test, when both the pool size expanding and boilover didn't exist. A hypothesis of a hot gas zone above oil layer in the cavity, which formed because of air recirculation in the ullage (as shown in Fig. 6.22) was suggested.

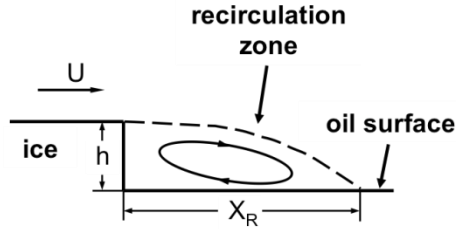


Fig. 6.22: Concept of air recirculation above oil in a cavity

A small-scale study of cavity fire with varying ullages [5] also showed similar trends. Experimental results of average mass burning rate per area (mass flux) as a function of non-dimensional ullage in 5 cm tank and cavity are summarized in Fig. 6.23. It is interesting to note that the mass flux in both cases start at around $0.0012 \text{ g/cm}^2\text{-s}$ at zero ullage, and as ullage increases, mass flux decreases at first and then increases. But in the case of tank fire, mass flux never increases beyond the one at zero ullage with increasing ullage. On the contrary, mass flux increases sharply in the cavity fire case, and asymptotes at a burning rate that is 2 times of the zero ullage result as the non-dimensional ullage is larger than 0.75, as shown in Fig. 6.23. Numerical simulations [5] show that the main reason for enhancement in a cavity fire is the resultant airflow pattern (recirculation) due to the ullage.

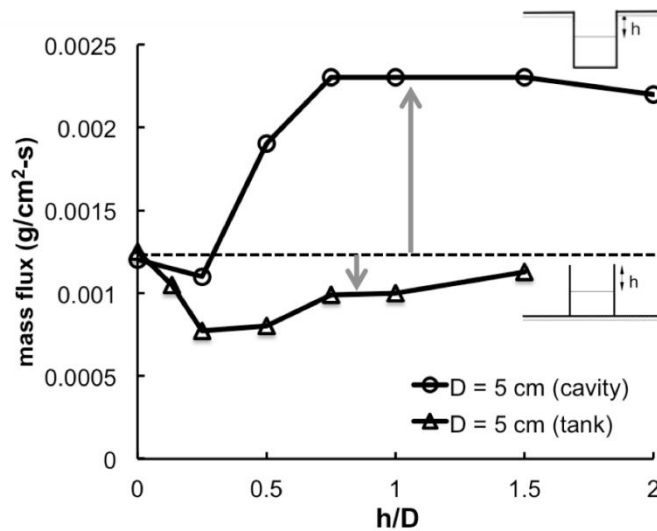


Fig. 6.23: Mass flux as a function of ullage (h) for cavity and tank fires in laminar flow regime.

When the geometry ratio (h/D) is smaller than its critical value, the fuel vapor is partially mixed with entrained air around the rim or cavity wall. As shown in Fig. 6.24, the recirculation pattern in 10 cm ullage is formed in the cavity but only covers the surface close to cavity wall. Oil vapor diffused upward from the oil surface is partially mixed with entrained air in the area that recirculation pattern is formed. Convective heat transfer is enhanced in the region close to the wall. However, the center of the pool does not see the premixing effect. When the ullage increases to 20 cm, more air is pulled into the cavity to form a larger recirculation zone above the oil surface. The area that is dominated by radiant heat transfer decreases and both convection and radiation become dominant because of the air/vapor pre-mixing.

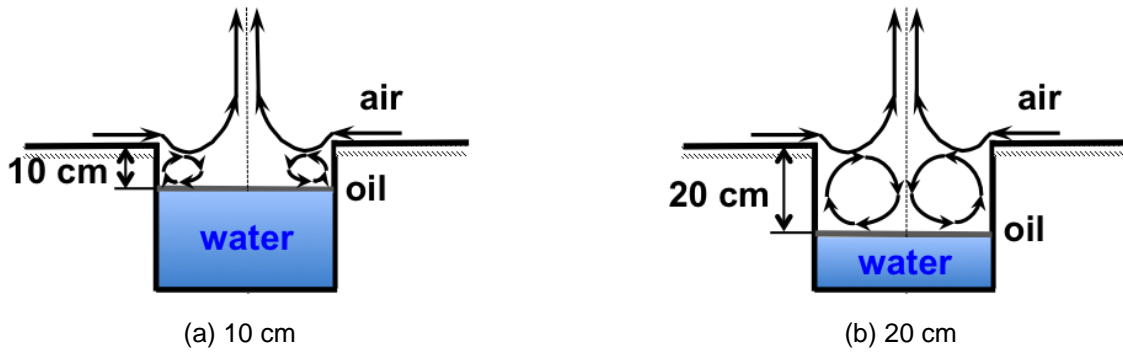


Figure 6.24: Airflow patterns of ullage at 10 and 20 cm in 1 m cavity

Figure 6.25 shows the total heat flux received on the ice wall inside a cavity as a function of time during the large scale burning in a 1 m cavity and 20 cm ullage conducted at WPI fire lab in February of 2015 (Test 2). The radiant and the total flux received on the ice surface in the same test are also shown for comparison. The dominance of convective heat transfer is clearly visible in Fig. 6.25.

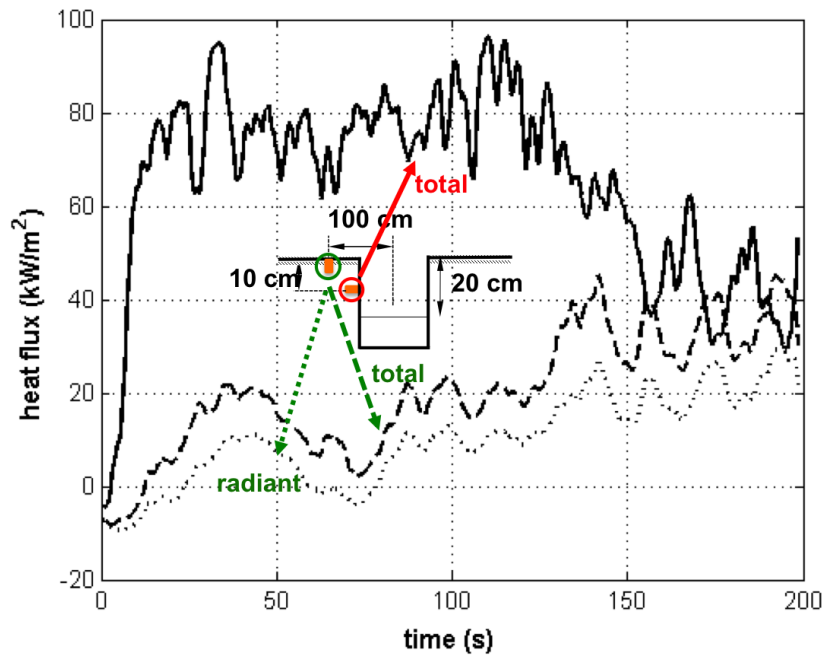


Fig. 6.25: Total heat flux received on cavity wall (indoor test $D = 1$ m, $h = 20$ cm)

The net radiant heat flux also increases because of the recirculation zone formation in the cavity. This was clearly observed in the outdoor tests performed at CRREL where additional heat flux gauges capable of measuring the radiant heat flux on the surface of the oil were deployed. Figure 6.26 shows the difference in the radiant heat flux at the oil surface inside a cavity (1 m) with two ullages of 10 and 20 cm (Test 6 and Test 4). Time of ignition, time to boilover and total burn time are also labeled to show the differences.

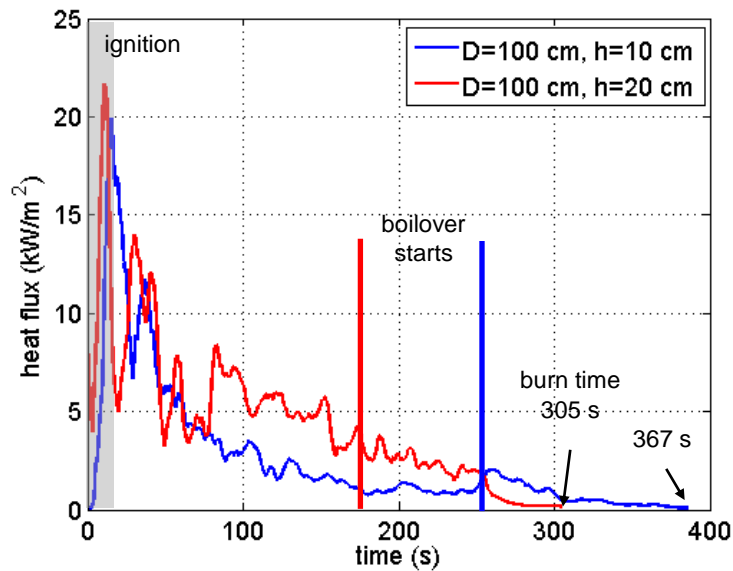


Fig. 6.26: Radiant flux received on center oil surface in 1 m cavity with different ullages

Figure 6.26 shows that the radiant flux is higher for the case with $h = 20$ cm compared to $h = 10$ cm. This results in faster onset of boilder in the case of $h = 20$ cm. Corresponding burn time is also faster (305 s compared with 367 s). The detailed experimental results of these two cases are summarized in Table 6.3.

Table 6.3: Experimental results comparison of 1 m cavity fire with ullage of 10 and 20 cm (CRREL)

Ullage (cm)	Lateral penetration (cm)	Mass flux (g/s-cm ²)	Efficiency (%)	Radiation on center oil surface (kW/m ²)	Time to boilder (s)
10	18	0.0038	89	1.4	270
20	11	0.0042	92	5.9	180

6.4 Conclusions

A series of large scale experiments were performed to analyze the burning behavior of ANS crude oil in an ice cavity. Results show that the burning rate and efficiency do not change much as the pool size increases from 1 m to 1.5 m. However, the ullage distance seems to have a significant influence on the burning behavior. As the ullage decreased from 20 cm to 10 cm in the 1 m pool, the average burning rate dropped by 10%. As discussed in Chapter 3, the presence of the ice wall causes significant geometry changes because of ice melting. The liquid fuel penetrates laterally into the ice wall forming a lateral cavity which reduces burning efficiency as the oil trapped in the cavity is difficult to burn and also clean up post combustion. The large scale outdoor tests at CRREL showed that lateral cavities are formed in salt water ice, similar to fresh water ice experiments reported earlier [2]. A linear relationship is observed between the cavity size and the mass burning rate per unit area. However, an optimized ullage can reduce the size of the cavity and also increase the burning rate and efficiency. This was shown based on two tests where doubling the ullage from 10 cm to 20 cm, improved burning rate and burn efficiency as well as reduced lateral penetration. However, 2 tests are still inclusive, and further tests to fundamentally explore the influence of ullage are warranted. The influence of fuel variation (weathering and emulsification) should also be considered in future tests.

6.5 References

1. Rangwala, A.S., Simeoni, A., and Shi, X., *Final report: Burning behavior of oil in ice cavities*. BSEE Contract No. E12PC00056, 2014.
2. Shi, X., Bellino, P., Simeoni, A., and Rangwala, A., *Experimental study of burning behavior of large-scale crude oil fires in ice cavities*. *Fire Safety Journal*, 2016. **79**: p. 91-99.
3. Heskestad, G., *Luminous heights of turbulent diffusion flames*. *Fire Safety Journal*, 1983. **5**(2): p. 103-108.
4. Shi, X., Bellino, P., and Rangwala, A.S., *Flame heat feedback from crude oil fires in ice cavities*. *Proc. Arctic and Marine Oilspill Program (AMOP)*, 2015. **38**: p. 767-776.
5. Shi, X., Sahu, A.K., Nair, S., Raghavan, V., and Rangwala, A.S., *Effect of ullage on burning behavior of small-scale pool fires in a cavity*. *Proc. Combust. Inst.*, 2016. **36**.

Chapter 7: Conclusions and recommendations for future work

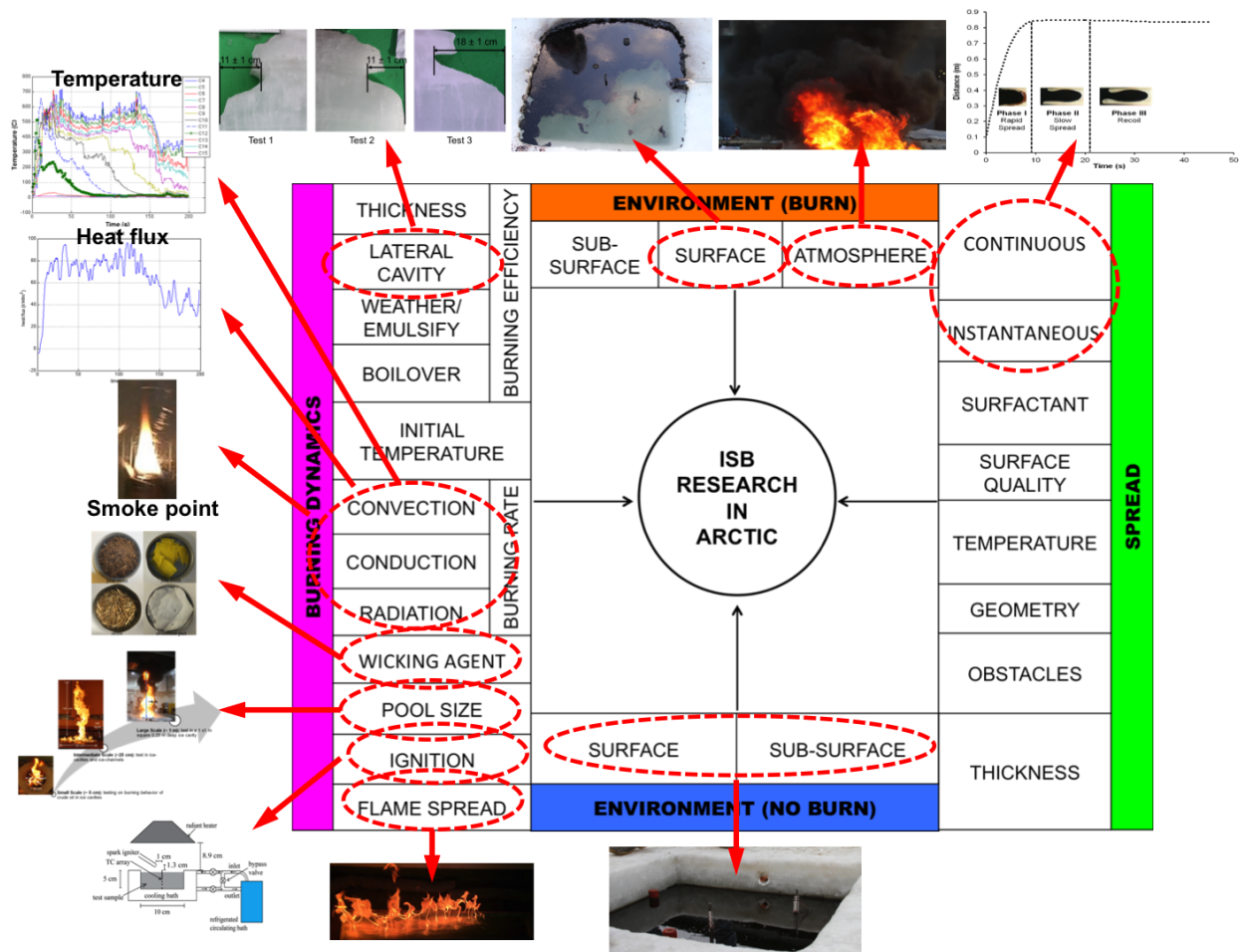


Fig. 7.1: *In situ* burning (ISB) study in the Arctic.

Figure 7.1 shows a macro-perspective of ISB research in the arctic region. The research problem can be divided into 4 main areas:

- a) **Burning dynamics**, investigating the fundamental research problem of ignition, flame spread, and burning behavior of an oil slick in the presence of arctic ice.
- b) **Environmental impact by ISB**, investigating the subsurface, surface, and atmospheric pollution because of ISB; its short-term and long-term consequences.
- c) **Spread of oil**, investigating the migration and chemical state (weathering, emulsification) of an oil slick, after a spill in the presence of ice, and snow
- d) **Environmental impact by no ISB**, investigating the surface and subsurface pollution and consequent impact of an oil spill if there is no ISB.

Each area can be further divided into sub research topics as shown in Fig. 7.1. The uniqueness of the Arctic environment presents unique challenges for fundamental investigation of burning, spread, and consequent environmental impact of a crude oil spill. Efficient response to an oil spill in the Arctic will require identification of controlling parameters which are different compared with ISB in open water and development of diagnostic tools for measurement, prediction, and forecasting the impact of a spill. Table 7.1, shows the layout of studies

conducted by WPI in two projects ICE I [1] and ICE II (current study) over a span of 4 years (2012 – 2016)

Table 7.1: Layout of studies conducted by WPI to date

	ICE I E12PC00056 (2012-2014)	ICE II E14PC00010 (2014 – 2016)
Phase I Small-Scale Tests	Task 1: Oil Spread Task 2: Burning behavior in small ice cavities (5 – 15 cm) Task 3: Modeling burning behavior in small ice cavities	Task 1: Ignition of oil Task 2: Smoke point of ANS Task 3: Lateral cavity formation Task 4: Technology (Burning Behavior with Wicking Agents)
Phase II Intermediate Scale Tests	Burning behavior in ice channels	Flame spread on ANS crude oil slicks (~3mm – 10mm) with cold boundaries
Phase III Large Scale Tests	Burning behavior in ice cavities ~100 cm (1 indoor test)	Burning behavior in ice cavities ~100 cm (2 indoor and 3 outdoor tests)

Since 2012, WPI has focused on *Burning Dynamics* and *Spread of Oil* at low temperature (-20 °C) and icy conditions. Fundamental research on ignition probability, flame spread, radiation, burning rate, burning efficiency, and migration of an oil spill have been performed. This research has led to revisiting several fundamental problems by setting it up in a new area of relevance to modern day oil exploration – the environmentally-sensitive Arctic environment. Second, the research has opened an entirely new discipline related to combustion in extreme cold climates. Several research papers have been published [1-10] demonstrating the impact of research performed.

In ICE I and II, the burning behavior of Alaska North Slope (ANS) crude oil in an ice cavity (fresh water and saltwater ice) with different diameters and oil thicknesses was characterized. Experiments included, small-scale (5-15 cm circular ice cavity), intermediate scale (25 cm circular ice cavity, and 65 ×16 cm² rectangular ice channel) and large sale (100 and 150 cm square ice cavity tested indoor and outdoor). The average regression rate of all experiments performed during ICE I and II are summarized in Fig. 7.2.

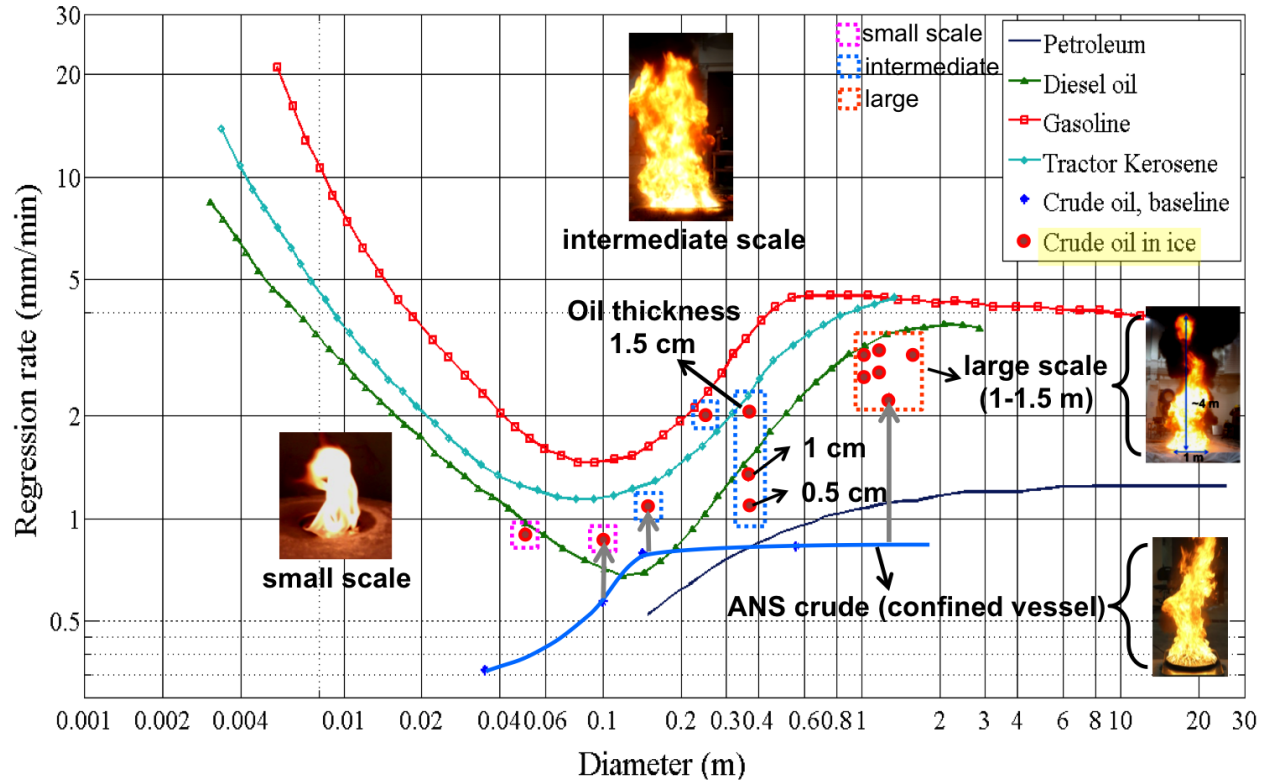


Fig. 7.2: Comparison of regression rates of burning in ice cavities and confined pools.
 Experimental data from Shi et al. [7] and Gottuk et al. [11].

As shown in Fig. 7.2 the regression rate for burning in an ice cavity does not follow the classical trend from literature for pool fires (Blinov and Khudiakov [11]). The *burning rate* in an ice cavity is around 2 to 3 times higher than the baseline cases (Fig. 7.3) which is a significant increase. In addition, current experiments show that it is not clear if the regression rate asymptotes at larger diameters (>1m) like the confined vessel tests. As shown in Fig. 7.3 the trend of regression rate vs. pool size is therefore still unresolved for oil spills bounded by ice. Second, the *burning efficiency* in an ice cavity is lower than the baseline case [7]. This means that burning in an ice cavity has a faster *rate* of oil removal by combustion; however, removal efficiency is low and more unburned oil is left behind compared to ISB on water [7]. The implication to the arctic environment is that burning rates during ISB may be high, but clean up rates will be low.

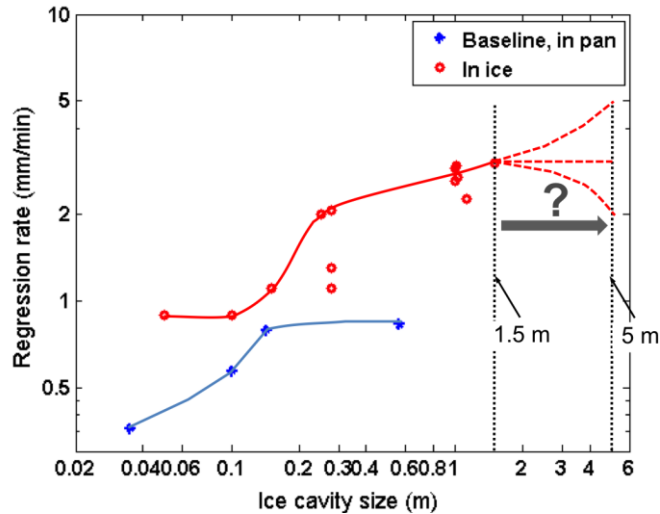


Fig. 7.3: Comparison of burning rate between ANS crude oil in a pan and ANS crude oil in an ice cavity.

It was shown that the controlling parameters for the net benefit (faster combustion) and net loss (lower efficiency) are geometry changes due to ice melting [4, 7, 12], radiation [4, 7], and oil penetrating sideways into the ice walls thereby creating lateral cavities where the oil is shielded from the flame heat flux [4, 7, 12, 13]. A second controlling parameter not investigated extensively, is the distance of the fuel layer from the ice-surface defined as the ullage. Two large scale tests performed at the US Army's Cold Regions Research and Engineering Laboratory (CRREL) show that both the burning rate and efficiency are highly dependent on the ullage.

Fundamental exploration of the influence of ullage on the burning behavior and investigation of the influence of increased scale or size of the pool fire are necessary to develop improved strategies for ISB in the arctic. Further, experimental data at large scales (greater than 1m) in the form of in-depth temperature profiles and radiative heat flux is unavailable in literature and will constitute an important milestone for future research.

References

1. Rangwala, A.S., Simeoni, A., and Shi, X., *Final report: Burning behavior of oil in ice cavities*. BSEE Contract No. E12PC00056, 2014.
2. Bellino, P., Flynn, M., and Rangwala, A.S., *A study of in-situ burning of crude oil in an ice channel*. Proc. Combust. Inst., 2012. **34**.
3. Bellino, P., Flynn, M., and Rangwala, A.S., *A study of spreading in an ice channel*. Journal of Loss Prevention in the Process Industries,, 2012.
4. Farahani, H.F., Shi, X., Simeoni, A., and Rangwala, A.S., *A study on burning of crude oil in ice cavities*. Proceedings of the Combustion Institute, 2015. **35**(3): p. 2699-2706.
5. Farahani, H.F., Jomaas, G., and Rangwala, A.S., *Effects of convective motion in n-octane pool fires in an ice cavity*. Combustion and Flame, 2015. **162**(12): p. 4643-4648.
6. Shi, X., Bellino, P., and Rangwala, A.S., *Flame heat feedback from crude oil fires in ice cavities*. Proc. Arctic and Marine Oilspill Program (AMOP), 2015. **38**: p. 767-776.
7. Shi, X., Bellino, P., Simeoni, A., and Rangwala, A., *Experimental study of burning behavior of large-scale crude oil fires in ice cavities*. Fire Safety Journal, 2016. **79**: p. 91-99.
8. Shi, X., Ghion, N.S., Fu, Y., Sundberg, K.T., Ramos, J.P., Stephansky, S., Ross, K., Kang, F., Raghavan, V., and Rangwala, A.S., *Influence of wicking agent on in-situ burning of water-in-oil*

- products from alaska north slope crude*. Proc. Arctic and Marine Oilspill Program (AMOP), 2016. **39**: p. 751-759.
9. Shi, X. and Rangwala, A. *Study of in-situ burning flame heat feedback in ice cavities*. in *Eastern States Combustion Meeting*. 2016. Princeton University, NJ.
 10. Van Gelderen, L., Brogaard, N.L., Sørensen, M.X., Fritt-Rasmussen, J., Rangwala, A.S., and Jomaas, G., *Importance of the slick thickness for effective in-situ burning of crude oil*. Fire Safety Journal, 2015. **78**: p. 1-9.
 11. Gottuk, D.T. and White, D.A., *Liquid fuel fires*. SFPE handbook of fire protection engineering, 2006. **15**(2): p. 297-316.
 12. Bellino, P.W., Rangwala, A.S., and Flynn, M.R., *A study of in situ burning of crude oil in an ice channel*. Proceedings of the Combustion Institute, 2013. **34**(2): p. 2539-2546.
 13. Farahani, H.F., Shi, X., Simeoni, A., and Rangwala, A.S., *A study on burning of crude oil in ice cavities*. Proc. Combust. Inst., 2014. **35**.